T2R2 東京科学大学 リサーチリポジトリ
Science Tokyo Research Repository

論文 / 著書情報
Article / Book Information

題目(和文)	
Title(English)	Structure-Property Relationship in Semiconducting Polymers for Organic Field-Effect Transistor Applications
著者(和文)	OTEPOVSULTAN
Author(English)	Sultan Otepov
出典(和文)	学位:博士(学術), 学位授与機関:東京工業大学, 報告番号:甲第12131号, 授与年月日:2021年9月24日, 学位の種別:課程博士, 審査員:道信 剛志,森 健彦,早川 晃鏡,松本 英俊,早水 裕平
Citation(English)	Degree:Doctor (Academic), Conferring organization: Tokyo Institute of Technology, Report number:甲第12131号, Conferred date:2021/9/24, Degree Type:Course doctor, Examiner:,,,,
学位種別(和文)	博士論文
Type(English)	Doctoral Thesis

Powered by T2R2 (Science Tokyo Research Repository)

Structure-Property Relationship in Semiconducting Polymers for Organic Field-Effect Transistor Applications

by
Sultan Otepov

Doctoral Thesis

Department of Materials Science and Engineering
Tokyo Institute of Technology

June 2021

Academic Supervisor: Associate Professor Tsuyoshi Michinobu

This thesis is dedicated to
my father, Dr. Parkhat Otepov.

Барлығы сіздің арқаңызда.

Abstract

Semiconducting polymers are promising materials for organic field-effect transistor applications. Design of the polymer structure is essential to achieve the best charge transport characteristics. It can be optimized by heteroatom substitution, backbone planarity tuning and/or side group engineering. First, charge transport properties of novel thiadiazolo[3,4-*f*]benzotriazole and 1,2-di(thieno[3,2-*b*]thiophen-2-yl)ethylene based polymers were optimized by tuning the backbone planarity using side alkyl group engineering approach. Second, effect of incorporation of electron-donating methoxy groups into a diketopyrrolopyrrole and quaterthiophene based copolymer was studied by synthesizing new random copolymers. Third, in-film cross-linking of poly(arylenebutadiynylene)s by thermal annealing and UV irradiation was demonstrated for the first time, and its effect on the charge transport properties was investigated. Experimental results were used together with theoretical calculations to derive the structure-property relationship in these polymers.

Accomplishments

Publications

1. Otep, S.; Wang, Y.; Kohara, A.; Matsumoto, H.; Mori, T.; Michinobu, T. Tuning Backbone Planarity in Thiadiazolobenzotriazole-Bis(thienothiophenyl)ethylene Copolymers for Organic Field Effect Transistors. *ACS Appl. Polym. Mater.* **2019**, *1*, 2302–2312. https://doi.org/10.1021/acsapm.9b00329.

2. Otep, S.; Michinobu, T.; Zhang, Q. Pure Organic Semiconductor-Based Photoelectrodes for Water Splitting. *Sol. RRL* **2020**, *4*, 1900395. https://doi.org/10.1002/solr.201900395.

3. Wang, S.; Otep, S.; Kimpel, J.; Mori, T.; Michinobu, T. N-Type Charge Carrier Transport Properties of BDOPV-Benzothiadiazole-Based Semiconducting Polymers. *Electronics* **2020**, *9*, 1604. https://doi.org/10.3390/electronics9101604.

4. Otep, S.; Lin, Y.-C.; Matsumoto, H.; Mori, T.; Wei, K.-H.; Michinobu, T. Diketopyrrolopyrrole–Thiophene–Methoxythiophene Based Random Copolymers for Organic Field Effect Transistor Applications. *Org. Electron.* **2020**, *87*, 105986. https://doi.org/10.1016/j.orgel.2020.105986.

5. Otep, S.; Ogita, K.; Yomogita, N.; Motai, K.; Wang, Y.; Tseng, Y.-C.; Chueh, C.-C.; Hayamizu, Y.; Matsumoto, H.; Ishikawa, K.; Mori, T.; Michinobu, T. Cross-Linking of Poly(arylenebutadiynylene)s and Its Effect on Charge Carrier Mobilities in Thin-Film Transistors. *Macromolecules* **2021**, *54*, 4351–4362. https://doi.org/10.1021/acs.macromol.1c00008.

Presentations

1. Otepov, S.; Michinobu, T. Photoelectrochemical Application of Thiadiazolobenzotriazole and Bis(thienothiophenyl)ethylene Based Donor-Acceptor Conjugated Polymers. 10th International Conference on Molecular Electronics and Bioelectronics. Nara, Japan, June 25–27, 2019. Oral.
2. Otepov, S.; Michinobu, T. Photoelectrochemical application of donor-acceptor conjugated polymers. 1st Tokyo Tech-NCTU Joint Symposium on Advanced Materials. Tokyo, Japan, September 2, 2019. Poster.

Acknowledgements

There are far too many people whose support and guidance allowed me to undertake this PhD. These acknowledgements will come nowhere close to sufficiently accounting for all of their help.

First and foremost, I am extremely grateful to my supervisor, Prof. Tsuyoshi Michinobu, for his continuous support and patience. Without his guidance I would not have been able to complete this PhD. Michinobu-sensei created countless opportunities for me to become an independent researcher. He always encouraged my interest to work on a wide range of projects. His involvement in planning of my future academic career gave me a confidence that I was taking the right steps.

Next, I would like to express my gratitude to researchers who have had an influence on me. I am deeply grateful to Prof. Yang Wang for his support. Wang-san's mentorship at the beginning of my journey was invaluable. I would like to thank Prof. Qichun Zhang for inviting me to do an exchange research in his group.

I would like to extend my sincere thanks to professors and researchers, collaboration with whom was invaluable for my completion of this PhD. I am grateful to Prof. Takehiko Mori group for collaboration in preparing and testing of the organic transistors; Prof. Hidetoshi Matsumoto group for taking the GIWAXS measurements and analyzing the results; Prof. Yuhei Hayamizu group for performing the Raman

spectroscopy measurements; Prof. Kung-Hwa Wei group for the synthesis of the random copolymers; Prof. Chu-Chen Chueh group for evaluation of the photovoltaic properties of semiconducting polymers.

I am also very grateful to the members of the Michinobu Laboratory for their help in numerous ways. With Kanehira-san, Otsuka-san, Hamada-san, Teraoka-san, Suzuki-san, and Joost, the Michinobu Laboratory was not a place to do only research, but also a place to enjoy spending time after a hard work.

I gratefully acknowledge the funding I received towards my PhD from the Japanese Government (MEXT) Scholarship Program.

I am indebted to all my friends. My special thanks go out to Zhasulan and Ayaulym, Yerlan and Agipa, Akylbek and Makpal, and Aliya for helping in whatever way they could during this challenging period. And a big thank you to my friends, who despite being far away, were always supportive and encouraging: Turganbay, Daulet, Bauyrzhan, Zarina, Narken, Serik and Nurzhan.

I would like to say thank you to my parents, brothers and sister. Without their support I would not have even thought about undertaking a PhD in the first place. My parents gave me the fundamentals necessary for thriving in scientific research. My father always encouraged me to pursue graduate studies.

I would like to thank my wife for being by my side and encouraging me to follow my dreams. Assem was always there to share all of the ups and downs of my PhD. I want thank my son, Bektemir, whose birth filled my PhD with an additional meaning. I also would like to say thank you to my mother, mother-in-law and sister-in-law for coming over to Japan and helping with childcare.

Table of Contents

List of Tables xi
List of Figures xii
List of Schemes xvii
Chapter 1. General Introduction 1
1.1. Introduction 1
1.2. Semiconducting Polymers 2
1.2.1. Charge transport in semiconducting polymers 2
1.2.2. Brief history of development of semiconducting polymers 5
1.3. Organic Field Effect Transistors 8
1.4. Strategies to Design High-Performance OFETs 12
1.4.1. Structure-property relationship in semiconducting polymers 12
1.4.2. Controlling acceptor/donor ratio 14
1.4.3. Heteroatom substitution 16
1.4.4. Side group engineering 18
1.4.5. Backbone planarity tuning 21
1.4.6. Random copolymerization 25
1.4.7. Molecular weight distribution 26
1.4.8. Improving device fabrication conditions 27
1.4.9. Topochemical polymerization 32
1.5. Concluding Remarks 33
Chapter 2. Backbone Planarity Tuning by Side-Chain Engineering 36
2.1. Introduction 36
2.2. Materials and Methods 40
2.2.1. Materials 40
2.2.2. General measurements 40
2.2.3. Theoretical calculations 43
2.2.4. OFET fabrication and characterization 44
2.2.5. Film morphology and microstructures 45
2.3. Results and Discussion 46
2.3.1. Polymer synthesis 46
2.3.2. Thermal properties 55
2.3.3. Optical and electrochemical properties 56
2.3.4. Theoretical calculations 59
2.3.5. OFET performances 63
2.3.6. Film morphology and microstructures 66
2.4. Conclusion 71

Chapter 3. Random Copolymers with Methoxy Conformational Locks 73
3.1. Introduction 73
3.2. Materials and Methods 75
3.2.1. Materials 75
3.2.2. General measurements 76
3.2.3. OFET fabrication and characterization 76
3.2.4. Film morphology and microstructures 77
3.3. Results and Discussion 78
3.3.1. Polymer synthesis 78
3.3.2. Thermal properties 79
3.3.3. Optical and electrochemical properties 80
3.3.4. OFET performances 83
3.3.5. Film morphology and microstructures 87
3.3.6. Effect of ionic additive on OFET performances 93
3.4. Conclusion 94
Chapter 4. Cross-linking of Poly(arylenebutadiynylene)s and Its Effect on Charge Transport Properties 96
4.1. Introduction 96
4.2. Materials and Methods 100
4.2.1. Materials 100
4.2.2. General measurements 100
4.2.3. Cross-linking of films 101
4.2.3. Theoretical calculations 102
4.2.4. OFET fabrication and characterization 102
4.2.5. Film morphology and microstructures 103
4.3. Results and Discussion 104
4.3.1. Polymer synthesis 104
4.3.2. Thermal properties 108
4.3.3. Optical and electrochemical properties 109
4.3.4. FTIR and Raman spectroscopy 112
4.3.5. Theoretical calculations 115
4.3.6. Film morphology and microstructures 120
4.3.7. Effect of cross-linking on charge transport 126
4.4. Conclusion 128
Chapter 5. Conclusion and Future Outlook 130
References 135

List of Tables

Table 2.1. Molecular weights and thermal properties of **P1–P6**. 52

Table 2.2. Evaluation of CHNS(Br) elemental analysis results of **P1–P6**. 53

Table 2.3. Summary of OFET performances of **P1**–**P6** 63

Table 3.1. Summary of properties of **P7**–**P11**. 78

Table 3.2. Summary of optimized OFET performances of **P7–P11**. 85

Table 3.3. Summary of the analysis of GIWAXS results of **P7–P11**. 89

Table 4.1. Summary of the properties of PDET and PDETT. 108

Table 4.2. Summary of OFET performances of PDET and PDETT. 127

List of Figures

Figure 1.1. Illustration of energy levels in conjugated polyenes with increasing repeat C−C and C=C bonds. Structures of π bonding MO and π* antibonding MO of ethylene, as well as HOMO and LUMO of polyacetylene are also given. 3

Figure 1.2. Idealized illustration of anisotropy of charge transport direction in conjugated polymers. 4

Figure 1.3. OFET configurations. 9

Figure 1.4. Typical output and transfer curves of a p-type OFET. 11

Figure 1.5. (a) Illustration of preferred orientation of edge-on and face-on packing orientations of conjugated polymers. (b) Illustration of intra- and inter-crystallite charge transport in (edge-on packed) semicrystalline polymer film. 13

Figure 1.6. Dependence of film morphology and μ_h on M_n in PBTTT. Reproduced with permission.[88] Copyright (2021) American Chemical Society. 26

Figure 1.7. Illustration of solution-based deposition techniques for polymer films. Adapted under Creative Commons Attribution 3.0 Unported Licence.[5] Colors were modified. 29

Figure 1.8. (a) PDA film for OFET applications prepared by topochemical polymerization of DCHD. Reproduced with permission.[103] Copyright (2021) John Wiley and Sons. (b) Topochemical polymerization of π-π stacked HBC by UV irradiation. Reproduced with permission.[104] Copyright (2021) American Chemical Society.....32

Figure 2.1. Thermal characterization results. (a) TGA curves of **P1–P6**. Second cycle DSC curves of (b) **P1**, (c) **P2**, (d) **P3**, (e) **P4**, (f) **P5**, (g) **P6-CF** and (h) **P6-CB**. 55

Figure 2.2. Absorption spectra of (a) **P1**, (b) **P2**, (c) **P3**, (d) **P4**, (e) **P5**, and (f) **P6** (**P6-CF**) in dilute solutions (in chloroform, CF, or chlorobenzene, CB), as-cast and annealed films. 58

Figure 2.3. (a) CV curves of the films of **P1–P6** and (b) energy level diagram of electrochemically determined E_{HOMO} and E_{LUMO} of **P1–P6** as well as $E_{g,opt}$ extracted from UV–vis–NIR absorption spectra. 59

Figure 2.4. Optimized structures of the polymers calculated with DFT. (a) Optimized structure of the four repeat D−A segments of **P1**. Optimized structures of D−A−D segments of (b) **P1**, (c) **P2**, (d) **P3**, (e) **P4**, (f) **P5** and (g) **P6**. Alkyl substituents were reduced to methyl groups. 60

Figure 2.5. DFT-calculated HOMO and LUMO of (a) **P1**, (b) **P2**, (c) **P3**, (d) **P4**, (e) **P5** and (f) **P6**. Alkyl substituents were reduced to methyl groups. g) Representation of calculated energy levels. 62

Figure 2.6. *I–V* behavior of polymers films in BGTC OFET devices: (a) transfer and (b) output curves of **P1** annealed at 260 °C; (c) transfer and (d) output curves of **P2** annealed at 150 °C; (e) transfer and (f) output curves of **P3** annealed at 325 °C; (g) transfer and (h) output curves of **P4** annealed at 250 °C; (i) transfer and (j) output curves of **P5** annealed at 250 °C; (k) transfer and (l) output curves of **P6-CF** annealed at 200 °C; (m) transfer and (n) output curves of **P6-CB** annealed at 250 °C. Measurements were done under ambient conditions in the dark. Transfer curves were recorded at V_D of −60 V. 65

Figure 2.7. GIWAXS images of (a) **P1** film annealed at 260 °C, (b) **P2** film annealed at 150 °C, (c) **P3** film annealed at 325 °C, (d) **P4** film annealed at 250 °C, (e) **P5** film annealed at 250 °C, (f) **P6-CF** film annealed at 200 °C and (g) **P6-CB** film annealed at 250 °C. Films were deposited onto n^+-Si/SiO_2/OTMS substrates and annealed for 10 min under Ar atmosphere. 66

Figure 2.8. (a) Out-of-plane and (b) in-plane 1D GIWAXS peak intensities of **P1** film annealed at 260 °C, **P2** film annealed at 150 °C, **P3** film annealed at 325 °C, **P4** film annealed at 250 °C, **P5** film annealed at 250 °C, **P6-CF** film annealed at 200 °C and **P6-CB** film annealed at 250 °C. Films were deposited onto n^+-Si/SiO_2/OTMS substrates and annealed for 10 min under Ar atmosphere. 67

Figure 2.9. AFM images of (a) **P1** film annealed at 260 °C, (b) **P2** film annealed at 150 °C, (c) **P3** film annealed at 325 °C, (d) **P4** film annealed at 250 °C, (e) **P5** film annealed at 250 °C, (f) **P6-CF** film annealed at 200 °C and (g) **P6-CB** film annealed at 250 °C. Films were deposited onto n^+-Si/SiO_2/OTMS substrates and annealed for 10 min under Ar atmosphere. 70

Figure 3.1. Amplified ^{1}H-NMR spectra of **P7–P11** (measured in $CDCl_3$) with assigned peaks shown on the chemical structure (right). 79

Figure 3.2. (a) TGA curves of **P7–P11** and DSC curves of (b) **P7**, (c) **P8**, (d) **P9**, (e)

P10 and (f) **P11**. 80

Figure 3.3. Optical and electrochemical properties of **P7–P11**. UV–vis–NIR absorption spectra of copolymers (a) in chloroform solutions and (b) in thin films. (c) CV curves. (d) Depiction of energy levels. 82

Figure 3.4. Selected transfer (left) and output (right) curves of (a) **P7**, (b) **P8**, (c) **P9**, (d) **P10** and (e) **P11**. All measurements were performed under vacuum. 86

Figure 3.5. GIWAXS patterns of (a) **P7**, (b) **P8**, (c) **P9**, (d) **P10** and (e) **P11**. Films were prepared identically to the optimized ones for transistor measurements (see above).. 87

Figure 3.6. Out-of-plane and in-plane 1D-profiles of GIWAXS measurements of **P7–P11**. 87

Figure 3.7. Atomic force microscopy images of (a) **P7**, (b) **P8**, (c) **P9**, (d) **P10** and (e) **P11**. Films were prepared identically to the optimized ones for transistor measurements (see above). 92

Figure 3.8. Transfer curves of OFET devices with Me_4NI ionic additive (Me_4NI/DPP = 1:30 mol) incorporated into thin films of (a) **P7**, (b) **P8** and (c) **P11**. (d) Average hole mobility measured with and without incorporation of Me_4NI ionic additive (Me_4NI/DPP = 1:30 mol) into thin films of **P7**, **P8** and **P11**. Films were annealed at 200 °C for 15 min. Values are the average of at least 20 devices prepared on two separate films. 94

Figure 4.1. FTIR spectra of (a) PDET and (b) PDETT, and ^{1}H NMR spectra of (c) PDET and (d) PDETT. 107

Figure 4.2. TGA and DSC curves of (a) PDET and (b) PDETT. 109

Figure 4.3. Solution and thin film UV–vis absorption spectra of (c) PDET and (d) PDETT. 111

Figure 4.4. CV curves of (a) PDET and (b) PDETT films. 112

Figure 4.5. FTIR spectra of (a) PDET and (b) PDETT films and Raman spectra of (c) PDET and (d) PDETT films. 113

Figure 4.6. Geometry optimization results using DFT calculations. Top and side views of the two repeat unit segments of (a) PDET and (b) PDETT. (c) Top and side views of 4 repeat units of PDET with one of the DET–DET segments coupled in *cis*-

configuration. Calculations were performed with B3LYP/6-31+G(d,p) basis set in 6 repeat units. Alkyl chains were reduced to methyl groups to save computational time. 116

Figure 4.7. HOMOs and LUMOs of (a) PDET and (b) PDETT, calculated with B3LYP/6-31+G(d,p) basis set. Calculations were performed on 6 repeat units. Alkyl chains were reduced to methyl groups to save computational time..... 117

Figure 4.8. (a) Representation of a rigid scan of 4DETT and 2DETT separated by 3.7 Å. (b) Basis set superposition error (BSSE) corrected total electronic energies calculated at different offset values using CAM-B3LYP/6-31+G(d,p) basis set. 0 kJ mol^{-1} corresponds to the sum of the total electronic energies of isolated 4DETT and 2DETT. Due to high computational cost, counterpoise corrections to address BSSE were included only at offsets of 2, 4, 6 and 9. BSSE was extrapolated to other results by using a quadratic fit. Alkyl chains were reduced to methyl groups in all calculations to save computational time. 118

Figure 4.9. Face-stacked dimers of two repeat DETT units optimized with CAM-B3LYP/6-311+G(d,p). Alkyl chains were replaced with methyl groups to save computational time..... 120

Figure 4.10. GIWAXS images of (a) as-cast and (b) annealed PDETT films. (c) Illustration of polymer packing and unit cell of as-cast PDETT (not to scale). Alkyl chains were omitted for clarity. GIWAXS 1D profiles of as-cast and annealed films of PDETT in (d) out-of-plane and (e) in-plane directions..... 120

Figure 4.11. GIWAXS images of (a) as-cast, (b) annealed and (c) UV-irradiated PDET films. GIWAXS 1D profiles of as-cast, annealed and UV-irradiated films of PDET in (d) out-of-plane and (e) in-plane directions. 123

Figure 4.12. Tapping-mode AFM images of (a) as-cast, (b) UV-irradiated, (c) and thermally annealed PDET films, (d) as-cast and (e) thermally annealed PDETT films. 124

Figure 4.13. Selected transfer and output curves of BGTC OFETs based on (a) as-cast PDET film, (b) as-cast PDETT film and (c) thermally annealed (200 °C) PDETT film. Devices based on the UV-irradiated and thermally annealed PDET did not show transfer curves. 126

Figure 4.14. Illustration of the effect of cross-linking on the film microstructure and charge transport pathways in PDET and PDETT. Red bars indicate cross-links that

block the interchain charge transfer sites due to the chemical bond geometry.....128

List of Schemes

Scheme 1.1. Structures of notable early polymers (first and second generations). R stands for arbitrary side group (e.g., alkyl). 6

Scheme 1.2. Structures of notable acceptor and donor units, as well as D-A polymers based on these units. R stands for arbitrary side group (e.g., alkyl). 7

Scheme 1.3. Structures of the notable high-performance semiconducting polymers achieved by controlling acceptor/donor ratio. * As reported in the same series of works.[56] 15

Scheme 1.4. Examples of heteroatom substitution in semiconducting polymers. 16

Scheme 1.5. Examples of side group engineering in semiconducting polymers. 19

Scheme 1.6. Examples of backbone planarity tuning in semiconducting polymers. .. 21

Scheme 1.7. Dihedral angles between NDI, IID, TBZ, DPP acceptors and their flanking units. 22

Scheme 1.8. Enhancement of coplanarity by "conformational locks" in T−T and Ph−T units. 23

Scheme 1.9. All-acceptor polymers utilizing planarizing vinylene bridge in conjugated backbone. 24

Scheme 1.10. Examples of random copolymers. 25

Scheme 2.1. Structures of BT, BBT and TBZ. Flanking thiophene units are shaded. R_1 and R_2 are arbitrary substituents (usually long and/or branched alkyl groups to improve solubility and control the thin film molecular packing). 37

Scheme 2.2. Structures of TBZ-DAE based copolymers reported previously, and those of TBZ-DTTE based copolymers developed in this work. 38

Scheme 2.3. Synthesis of acceptor monomers **A1**, **A2** and **A3**. 48

Scheme 2.4. Synthesis of donor monomers **D1**, **D2** and **D3**. 50

Scheme 2.5. Synthesis of **P1–P6**. A typical condition for Pd-catalyzed Stille polycondensation is illustrated, see the text for details. 51

Scheme 3.1. Structures of the monomers **M1–M3** and synthetic route to copolymers **P7–P11**.....78

Scheme 4.1. (a) Topochemical polymerization of butadiyne (diacetylene) monomers by 1,4-coupling to form PDA. Newly formed bonds are given in red. (b) Examples of cross-linking of small molecules and conjugated polymers by topochemical polymerization of butadiynes.....98

Scheme 4.2. Synthesis of PDET. 104

Scheme 4.3. Synthesis of PDETT.....105

Scheme 4.4. Illustration of ideal cross-linking of the PDET and PDETT films by 1,4-coupling of butadiyne moieties (newly formed bonds are given in red). 115

Scheme 5.1. Examples of PTBZ-DTTE polymers with alternative side group placements.....131

Scheme 5.2. Structure of random copolymers with longer alkoxy groups for better solubility.....132

Scheme 5.3. Examples of possible robust poly(arylenebutadiynylene)s. 133

Chapter 1.

General Introduction

1.1. Introduction

Organic semiconductors are a promising alternative for conventional inorganic semiconductors applied in electronics due to the versatility of synthesis, tunable electrochemical properties and solution-processability.[1–4] One of such applications is organic field effect transistors (OFETs). As electric current switching and amplification devices, OFETs are an integral part of potentially all electronics, such as displays, sensors, smart tags, electronic papers, and integrated circuits.[2,4]

Organic semiconductors can be classified into small molecules and polymers, both of which have their own pros and cons in terms of OFET performance and manufacturing process engineering. Small molecule semiconductors can be easily purified during the synthesis and can form crystalline films, which is advantageous for high-performance devices.[2] Polymers, on the other hand, possess good solution-processability (e.g., sprayable, printable, etc.), which makes the device fabrication process more scalable.[5] In addition, polymer films can have good flexibiltiy.[3] These two properties make semiconducting polymers more attractive candidates than the small molecule counterparts for applications in flexible and large-area printed

electronic devices.

1.2. Semiconducting Polymers

1.2.1. Charge transport in semiconducting polymers

Understanding of fundamentals of charge transport in semiconducting polymers is important for the development of high-performance materials for OFET applications. This section shortly introduces the basics of charge transport in organic semiconductors, which can be found in more details in literature. [1,6–8]

Semiconducting polymers have a π-conjugated backbone consisting of alternating carbon-carbon single bonds (C−C) and carbon-carbon double bonds (C=C). A C=C bond contains a σ molecular orbital formed by direct overlap of sp^2 hybridized atomic orbitals, and a π molecular orbital formed by parallel overlap of p_z atomic orbitals. In conjugated polymers, π bonding and π* antibonding orbitals tend to delocalize, forming band-like highest occupied molecular orbital (HOMO) and the lowest unoccupied molecular orbital (LUMO), respectively (Figure 1.1). With increasing conjugation length, the energy gap (E_g) between HOMO and LUMO becomes smaller, so that electrons can be excited from HOMO to LUMO by thermal activation or by absorption of photons. Then electron or hole charge carriers can be generated by reduction or oxidation, respectively, which can then be transported across the semiconducting polymer film. Although band-like charge transport along the

polymer chain is possible in polymers with highly rigid backbones, bands formation is limited to several repeat units in a typical polymer due to backbone torsion. In addition, charge transport channels of electronic devices are much larger than the polymer chain length.[3] Therefore, operation of the electronic devices inevitably involve inter-chain charge transfer.

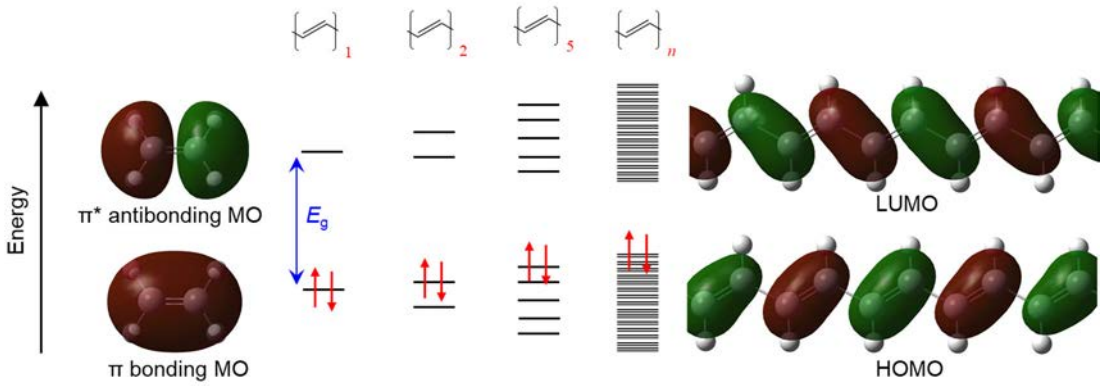


Figure 1.1. Illustration of energy levels in conjugated polyenes with increasing repeat C−C and C=C bonds. Structures of π bonding MO and π* antibonding MO of ethylene, as well as HOMO and LUMO of polyacetylene are also given.

Since polymer chains are held by weak van der Waals forces, they have large separation and experience significant vibrations. As a result, inter-chain HOMO and LUMO bands do not form and charge transfer between polymer chains happens by tunneling ("hopping"). Furthermore, due to the planarity of the conjugated backbone the π-π overlaps have high directionality, so that charge hopping strongly depends on their alignments. Thus, the crystallinity and molecular packing orientation are important factors that determine the charge transport properties of semiconducting

polymers.

The molecular packing motif of a crystalline region of a conjugated polymer film can be simplified as a parallel alignment of planar backbones (Figure 1.2). Then, band-like charge transport can take place along the conjugated backbone, while charge transport takes place by their "hopping" in the π-π stacking direction. Due to the large separation of the conjugated backbones, charge transport does not take place in the lamellar stacking direction.

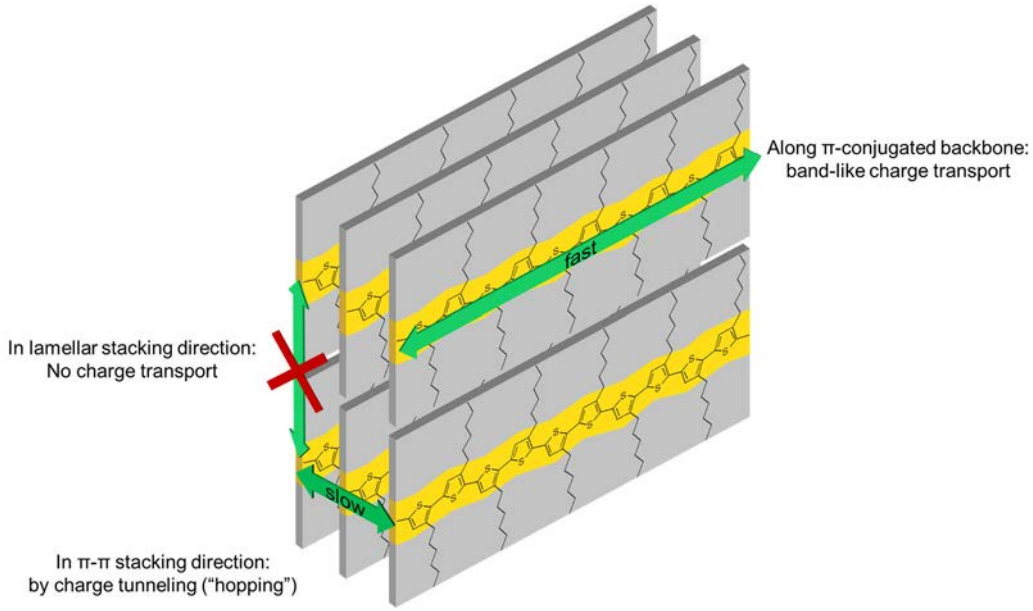


Figure 1.2. Idealized illustration of anisotropy of charge transport direction in conjugated polymers.

The speed of charge carriers per unit applied electric field is called charge carrier mobility (μ) and is expressed in units of $cm^2\ V^{-1}\ s^{-1}$. For comparison, amorphous and crystalline Si have μ = ~1 and >1000 $cm^2\ V^{-1}\ s^{-1}$, respectively.[7] Currently, semiconducting polymers giving μ beyond 10 $cm^2\ V^{-1}\ s^{-1}$ have been reported.[9–11] Thus,

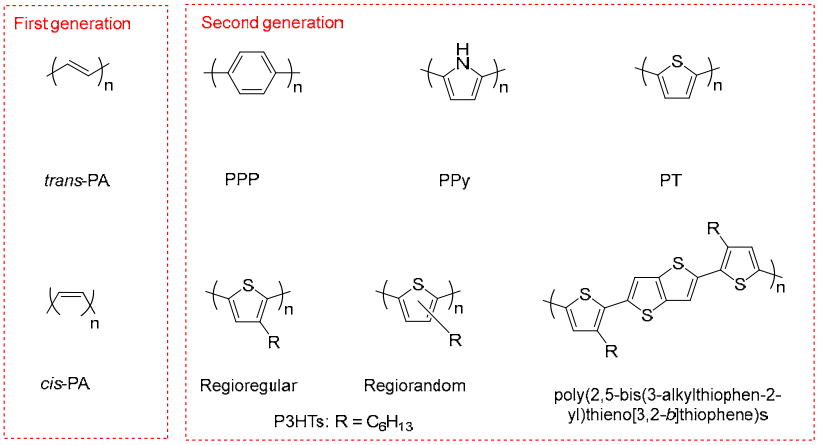
current level of developments of semiconducting polymers makes their implementation as alternative materials for amorphous Si-based electronic devices possible.

1.2.2. Brief history of development of semiconducting polymers

Conducting properties of organic polymers was first discovered in polyacetylene (PA) in 1977 (Scheme 1.1).[12] Following this discovery, research in semiconducting polymers gradually increased.[13–15] PA was first applied in OFETs in 1983.[16] PAs were termed as First Generation semiconducting polymers.[1] However, PA films were intractable and had low chemical stability due to rapid oxidation in air. These made researchers search for solutions to overcome these issues.

Polymers with repeat aromatic units, like poly(1,4-phenylene) (PPP), poly(thiophene) (PT), poly(pyrrole) (PPy), showed better stability compared to PA because of the lowered energy levels due to localization of charge carriers in aromatic units (Scheme 1.1). Especially, heterocyclic units proved to be promising and the first working polymer-based OFET was prepared from PTs in 1986, showing hole mobility (μ_h) of 2×10^{-5} cm^2 V^{-1} s^{-1}.[17] By introducing side alkyl groups, polymers were made solution-processable. For example, poly(3-hexylthiophene) (P3HT), which is one of the most studied semiconducting polymers, exhibited improved μ_h of up to 10^{-4} cm^2 V^{-1} s^{-1}.[18] The early studies in PAs and PTs were important in terms of understanding the

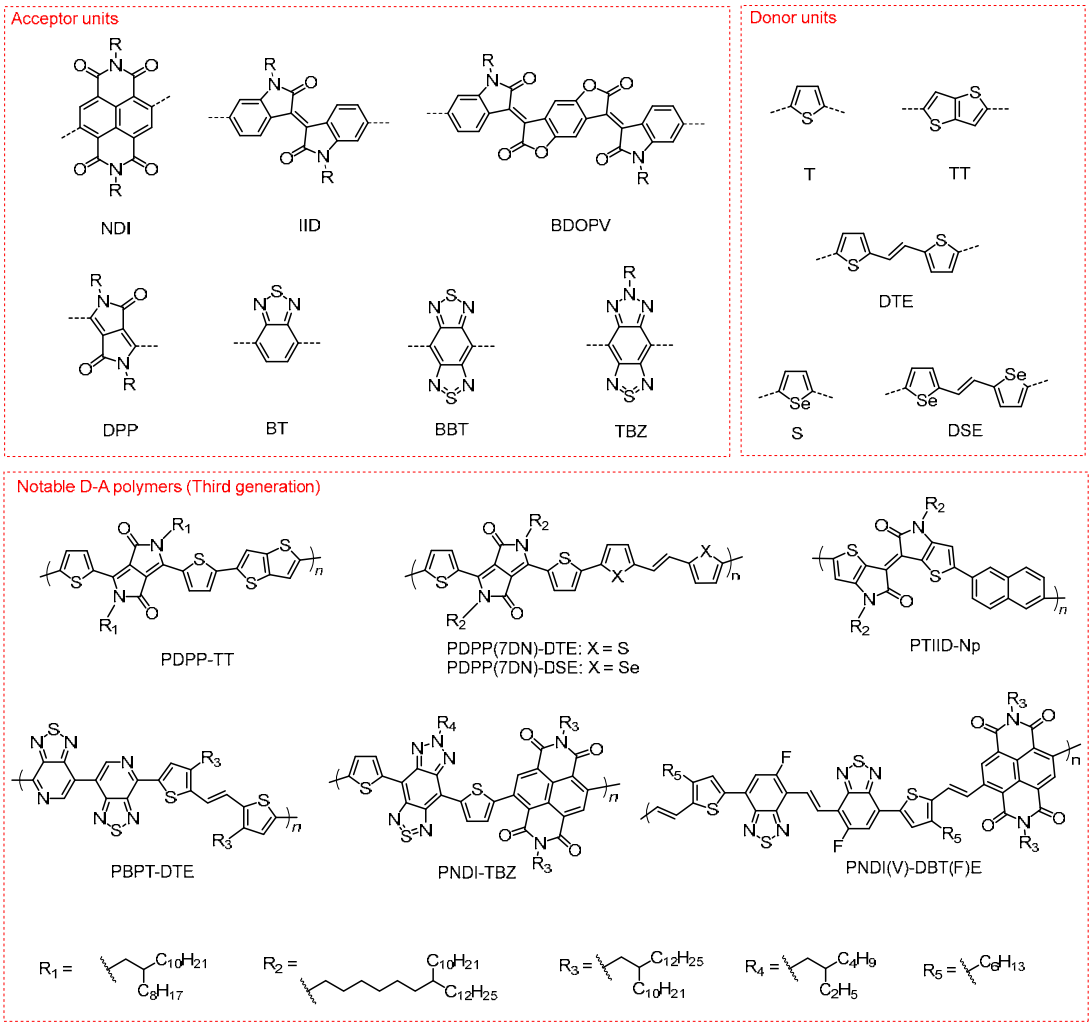
physics of charge transport in semiconducting polymers. Alternation of repeat units in the polymer backbone showed to be an effective approach to improve μ.[19–22] For example, inclusion of thieno[3,2-*b*]thiophene (TT) further improved μ_h, reaching 0.2–0.6 $cm^2 V^{-1} s^{-1}$.[19,20] These polymers marked the Second Generation of semiconducting polymers.[1]



Scheme 1.1. Structures of notable early polymers (first and second generations). R stands for arbitrary side group (e.g., alkyl).

Polymers with alternating electron-deficient (acceptor) and electron-rich (donor) units exhibited low E_g and gave higher μ, due to significantly improved intra-chain charge transfer.[23] Success of the donor-acceptor (D-A) semiconducting polymer design in early 2000s boosted the development of building blocks with more atoms in π-conjugated backbone.[1] Prominent examples of acceptor units are diketopyrrolopyrrole (DPP),[9–11,24–29] isoindigo (IID),[30–33] naphthalene diimide (NDI),[34–39] benzodifurandione-based oligo(*p*-phenylene vinylene) (BDOPV),[40,41]

benzothiadiazole (BT),[42–45] benzobisthiadiazole (BBT),[42,45–47] and thiadiazolobenzotriazole (TBZ) (Scheme 1.2.).[47,48] On the other hand, donor units are mostly based on thiophene and its derivatives, such selenophene (S), TT, di(thienyl)ethylene (DTE), and so on.[3,30]



Scheme 1.2. Structures of notable acceptor and donor units, as well as D-A polymers based on these units. R stands for arbitrary side group (e.g., alkyl).

PDPP-TT was the first D-A semiconducting polymer with $\mu_h = 0.94$ cm^2 V^{-1} s^{-1} approaching that of amorphous Si, which was reported in 2010.[24] Few years later

ultrahigh μ_hs exceeding 10 cm^2 V^{-1} s^{-1} were reported for PDPP(7DN)-DTE,[10] PDPP(7DN)-DSE,[11] and PTIID-Np.[32] Designing of strong acceptor units allowed to prepare n-type and ambipolar semiconducting polymers, whose development was lagging behind their p-type counterparts.[3] In addition, in the past few years all-acceptor polymers with μ_es above 5 cm^2 V^{-1} s^{-1} emerged, such as PBPT-DTE,[49] PNDI-TBZ,[50] and PNDI(V)-DBT(F).[51] Following the above convention, D-A polymers were classified as Third Generation semiconducting polymers.[1]

1.3. Organic Field Effect Transistors

The terms OFETs and organic thin-film transistors (OTFTs) are used interchangeably in literature.[3,4] This arises from the resemblances in structural design and bottom-up fabrication used to prepare both inorganic and organic TFTs.[52] This thesis will follow the convention of naming these devices as OFETs.

OFETs comprise of source, drain and gate electrodes. Depending on the positions of the electrodes relative to the semiconductor film, there are four different architectures of OFETs (Figure 1.3): bottom-gate top-contact (BGTC), bottom-gate bottom-contact (BGBC), top-gate top-contact (TGTC) and top-gate bottom-contact (TGBC).[53] The architecture affects both fabrication feasibility and device performance. In general, for characterization of p-type semiconductors BGTC configuration is used due to

fabrication simplicity. TGBC design is preferred for n-type semiconductors due to the added protection by the top gate dielectric from the ambient atmosphere.

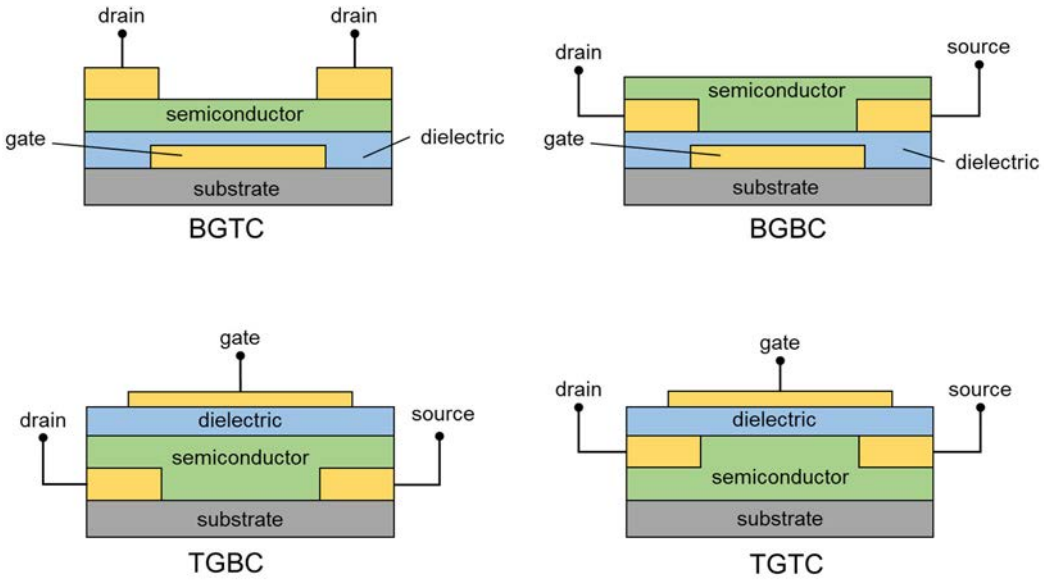


Figure 1.3. OFET configurations.

The operation principles of OFETs are provided below as described in literature.[52] If a negative potential is applied at gate of a p-type OFET, the holes are attracted to the dielectric-semiconductor interface due to the capacitive effect and form a p-channel. Then if a negative potential is applied at drain, the holes are injected from source and transported to drain. The gate voltage (V_G) at which the channel forms is called threshold voltage (V_T) of the device and the OFET is said to be on when $V_G \geq V_T$. The relation between V_G and drain voltage (V_D) affects the properties of the channel and, thus, determines how drain current (I_D) behaves. When V_D is low, the channel thickness is almost uniform and it depends on the magnitude of V_G. Since channel

resistance is inversely proportional to its thickness, the device acts as a variable resistor as long as $V_D < V_G - V_T$ holds true. This implies that I_D depends linearly on V_D:

$$I_D = \frac{W}{L} \mu C_i \left(V_G - V_T\right) V_D ,$$

where W and L are channel width and length, respectively, C_i – specific surface capacitance of the dielectric. This operation mode is called linear mode or triode mode. As V_D increases, electrons are injected from drain into the semiconductor and the channel thickness near drain decreases due to the charge recombination. When V_D becomes substantially high so that $V_D = V_G - V_T$, the channel pinches off near drain. Further increase in V_D enlarges this pinched off region but does not affect I_D because now the charge transport happens through a thin channel, whose thickness cannot be altered. Thus, I_D saturates with respect to V_D, and it is essentially controlled by the shape of the remaining part of the channel, which still depends on V_G. This mode is called saturation mode or active mode, and I_D is determined as:

$$I_D = \frac{W}{2L} \mu C_i \left(V_G - V_T\right)^2 .$$

OFETs are characterized by measuring current-voltage behavior using output and transfer curves (Figure 1.4). Output curve represents I_D-V_D behavior at constant V_G, while transfer curve depicts I_D-V_G behavior at constant V_D.

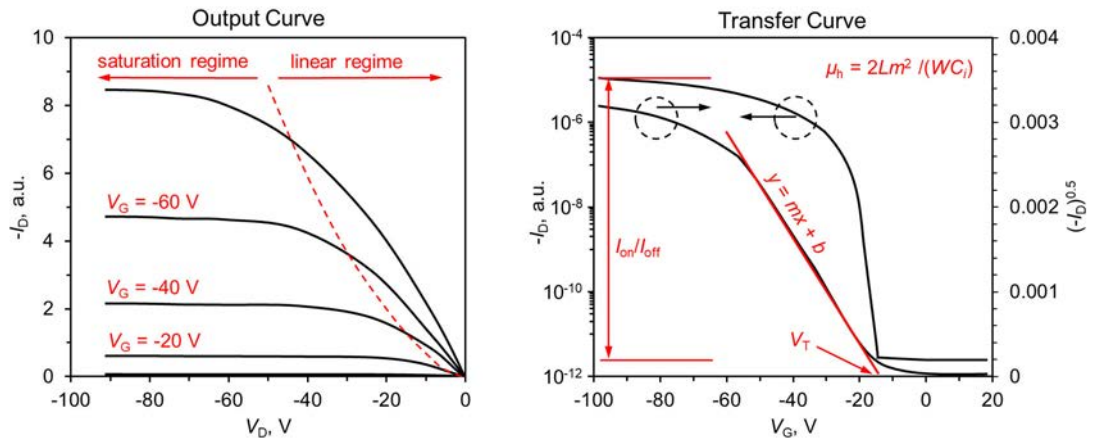


Figure 1.4. Typical output and transfer curves of a p-type OFET.

Field-effect μ can then be calculated from the *I*-*V* equations of either the linear or saturation regime. Since FETs in practice are employed in active mode, μ extracted from the saturation regime is reported in literature:

$$\mu = \frac{2L}{WC_i} \frac{I_D}{(V_G - V_T)^2}.$$

First, $(I_D)^{1/2}$–V_G curve is plotted and the linear fit is applied at the slope region ($V_G > V_T$). The slope of the linear fit gives the second term of the equation. Extrapolation of the linear fit line to the horizontal axis gives V_T. Ratio of the on and off currents (I_{on}/I_{off}) is determined from the maximum and minimum I_D. I_{on}/I_{off} shows the difference between current when device is on and the leakage current when it is off. Higher I_{on}/I_{off} is preferred for all FETs, which is typically in the range of 10^6–10^{10}.

OFETs are benchmarked according to their μ, V_T and $I_{on/off}$, as well as other properties like contact resistance, hysteresis of the transfer curve, subthreshold swing,

reproducibility and stability.[53] Out of these, values of μ are used for basic comparison because high μ usually guarantees high $I_{on/off}$, in addition to fast response time and large current output of the device.

1.4. Strategies to Design High-Performance OFETs

1.4.1. Structure-property relationship in semiconducting polymers

Ultimate goal in producing an OFET is to achieve high charge carrier mobility and control the type of the major charge carriers (i.e., p-type, n-type or ambipolar), as well as to achieve good stability. While the type of the charge carrier is mostly pre-determined by the intrinsic electronic properties of the polymer, μ can be strongly influenced by the film properties, such as π-π stacking distance ($d_{\pi\text{-}\pi}$), lamellar stacking distance (d_L), molecular packing orientation, and crystallinity. Firstly, due to the anisotropy of charge "hopping" direction edge-on stacking of polymer backbones with respect to substrate surface is the favorable molecular packing orientation for OFETs (Figure 1.5).[54] Typically, polymers have $d_{\pi\text{-}\pi}$ in the range of 3.6–4.0 Å, while some exceptionally tight packing with $d_{\pi\text{-}\pi}$ as short as 3.4 Å were also reported.[51] Secondly, long-range ordered and tight π-π stacking facilitates efficient intra-crystallite charge transport, which is much faster than inter-crystallite charge crossing.[55] Thus, higher crystallinity leads improved μ due to less boundaries between crystallites. In addition,

inter-crystallite charge transfer can be facilitated by π-conjugated pathways that can be created by long polymer chains.[55]

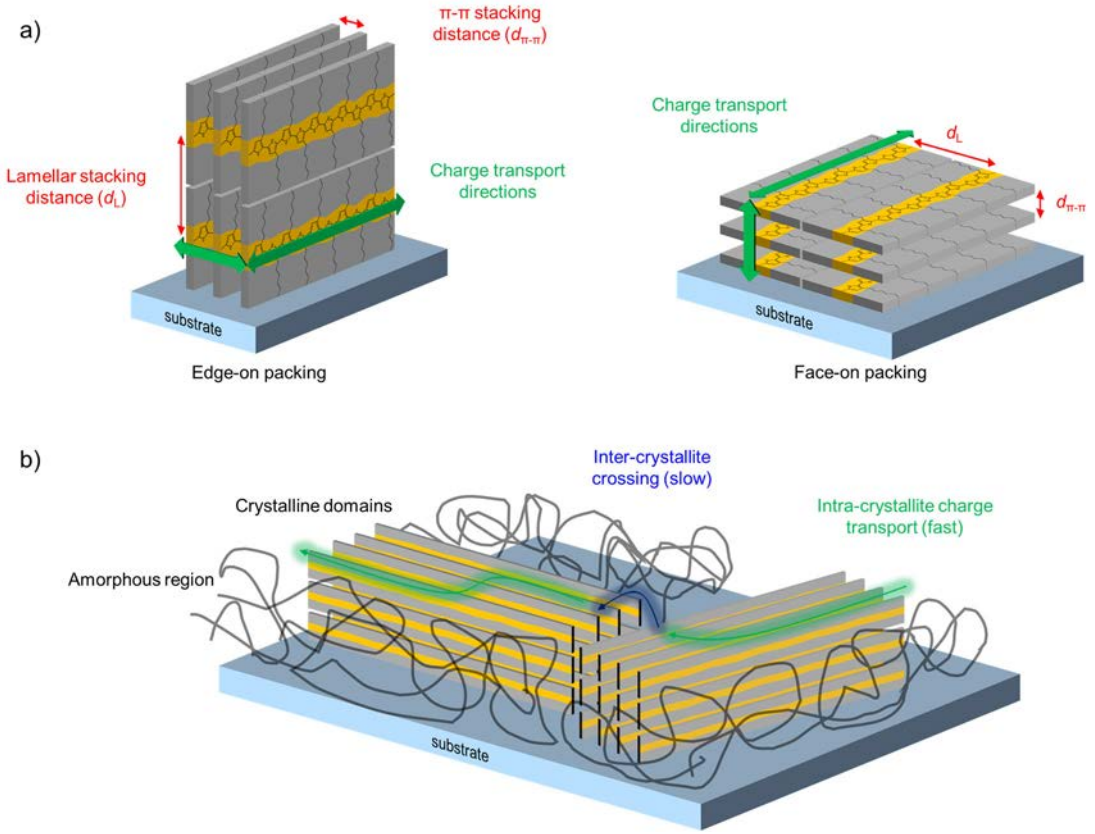


Figure 1.5. (a) Illustration of preferred orientation of edge-on and face-on packing orientations of conjugated polymers. (b) Illustration of intra- and inter-crystallite charge transport in (edge-on packed) semicrystalline polymer film.

Film morphology and microstructure, in turn, can be controlled by deliberately tuning the polymer design. Although the design of D-A conjugated polymers has almost endless variety, the most influential approaches can be roughly classified as controlling donor-to-acceptor ratio, heteroatom substitution, side chain engineering, backbone planarity tuning, random copolymerization. In addition, film properties also depend on

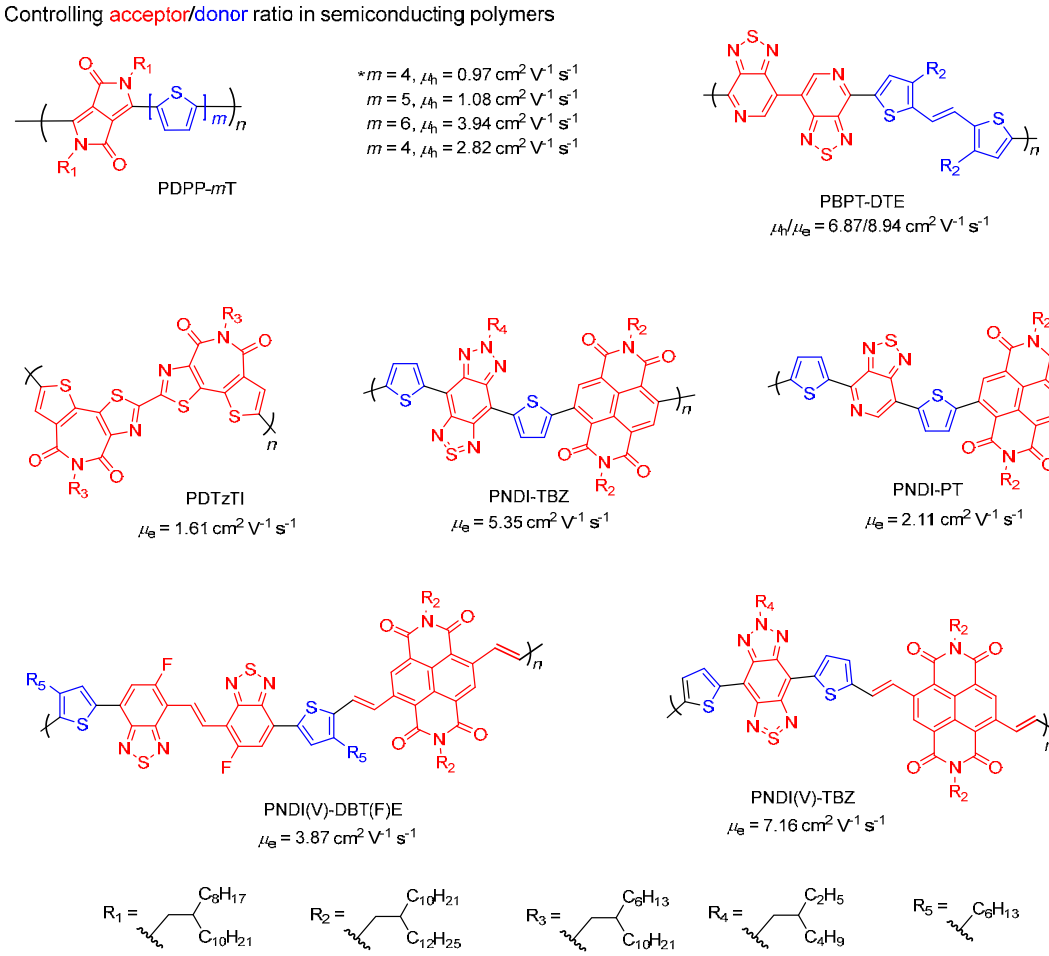
molecular weight distribution of the polymers as well as the film preparation conditions. The next sections will discuss these methods in detail and cover some examples to gain insight into the current trends and challenges in improving polymer OFET performances.

Recently, synthesis of polydiacetylenes by in-film topochemical polymerization of monomers has emerged as a promising method to prepare semiconducting films. Recent advances in this field will also be shortly covered.

1.4.2. Controlling acceptor/donor ratio

Each acceptor building block can perform differently depending on what donor unit is used.[30,37,46] Enhanced charge transport properties can be achieved by altering the acceptor/donor ratio.[25,56,57] Increasing the donor content from m = 4 to m = 6 in DPP-mT copolymers led to the improvement of μ_h from 0.97 to 3.94 $cm^2 V^{-1} s^{-1}$, up to point when solubility became a hindering effect for m = 7 due to the decreased alkylation extent. On the other hand, increasing the acceptor/donor ratio in the polymer backbone can lower E_{LUMO} and E_{HOMO} levels and open prospects for designing n-type and ambipolar semiconducting polymers. For example, a dual-acceptor polymer PBPT-DTE showed ambipolar charge transport with high μ_h/μ_e of 6.87/8.94 $cm^2 V^{-1} s^{-1}$.[49] A prominent example of all-acceptor polymers is PDTzTI, which exhibited μ_e = 1.61 cm^2

V^{-1} s^{-1}.[58]

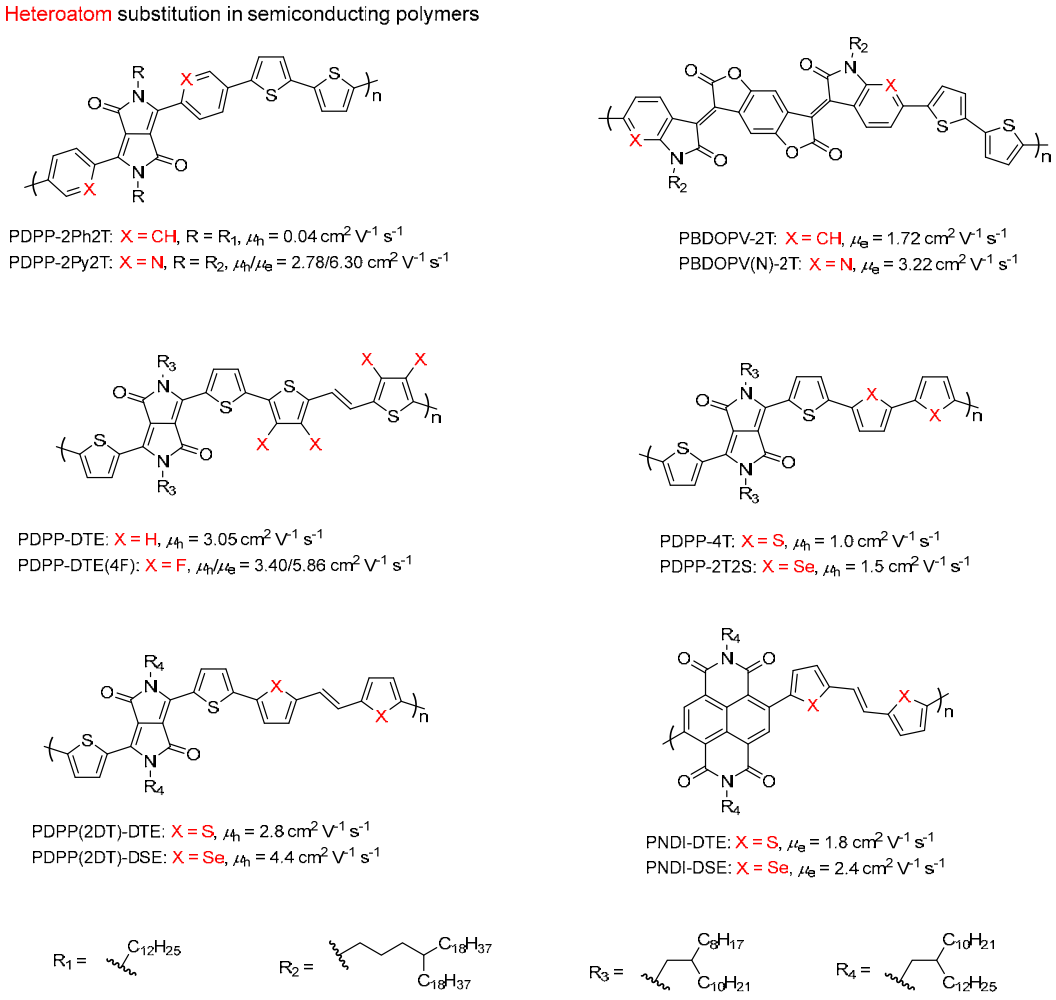


Scheme 1.3. Structures of the notable high-performance semiconducting polymers achieved by controlling acceptor/donor ratio. * As reported in the same series of works.[56]

A tandem effect of two different acceptor units were implemented in several A_1-D-A_2-D polymers to obtain enhanced n-type charge transport.[44,45,50,59,60] For example, PNDI-TBZ and PNDI-PT were reported as unipolar n-type polymers, which exhibited μ_e of 5.35 and 2.11 cm^2 V^{-1} s^{-1}, respectively.[50] PNDI-TBZ assumed bimodal molecular packing orientation ($d_{\pi\text{-}\pi}$ = 3.63 Å), while PNDI-PT exhibited edge-on dominant packing ($d_{\pi\text{-}\pi}$ = ~4 Å). By including vinylene bridges, both planarization and extension

of the π-conjugation in dual-acceptor units was achieved in PNDI(V)-TBZ, which exhibited $\mu_e = 7.16$ cm^2 V^{-1} s^{-1}, while PNDI(V)-DBT(F)E gave $\mu_e = 3.87$ cm^2 V^{-1} s^{-1}.[51] Both polymers showed very deep E_{LUMO} of −3.87 and −3.80 eV, respectively. In addition, PNDI(V)-DBT(F)E films acquired tight edge-on packing ($d_{\pi\text{-}\pi}$ = 3.49 Å), while PNDI(V)-TBZ had tight bimodal packing ($d_{\pi\text{-}\pi}$ = 3.40–3.45 Å).

1.4.3. Heteroatom substitution



Scheme 1.4. Examples of heteroatom substitution in semiconducting polymers.

Heteroatom substitution is an effective tool to design semiconducting polymers with desirable charge polarities (Scheme 1.4). In general, *N*-substitution is used as a means to enhance n-type charge transport or to flip the p-type charge transport into n-type/ambipolar.[28,33,40,48] For example, PDPP-2Ph2T showed a μ_h of 0.04 $cm^2\ V^{-1}\ s^{-1}$,[61] while its *N*-substituted counterpart PDPP-2Py2T exhibited high μ_h/μ_e of 2.78/6.30 $cm^2\ V^{-1}\ s^{-1}$.[28] Nitrogen atoms can be introduced into the π-conjugated backbone of the acceptor units as well. For example, *N*-substituted BDOPV(N)-2T exhibited improved μ_e of 3.22 $cm^2\ V^{-1}\ s^{-1}$ thanks to the tight π-π stacking (3.44 Å) and lowered E_{LUMO},[40] compared to the original BDOPV-2T.[41] Presence of several distinct positions for *N*-substitution opens a further way to optimize this method.[33] Halogen-substitution, of which fluorine (F)-substitution is the most widely applied, is also effective in lowering the energy levels of the polymers. For example, the E_{HOMO} of PDPP-DTE was lowered by 0.15 eV by F-substitution of the DTE unit, and the resulting polymer gave balanced ambipolar charge transport with μ_h/μ_e = 3.40/5.86 $cm^2\ V^{-1}\ s^{-1}$.[29] Thus, heteroatom substitution with atoms with high electronegativity allows to improve the n-type properties of polymers.

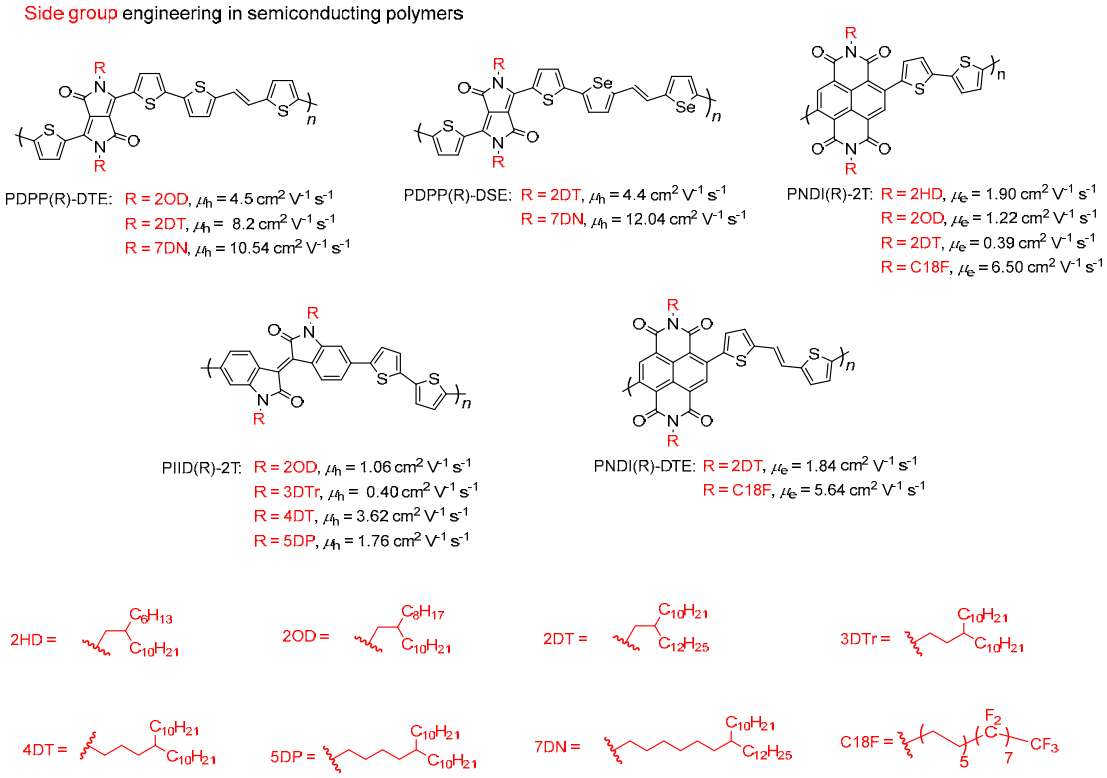
On the other hand, swapping of S with more electron-rich Se can enhance the electron-donating nature of the donor units and produce more p-type polymers. For example, changing 2,2'-bithiophene of PDDP-4T with 2,2'-biselenophene (PDPP-

2T2S) resulted in enhancement of the μ_h from 1.0 to 1.5 $cm^2 V^{-1} s^{-1}$.[62] Improvements were attributed to the lowered $E_{g,opt}$ (from 1.39 to 1.32 eV) and more fiber-like texture with shortened d_L (from 19.10 to 18.53 Å). Improvements of μ_h in a similar order (by ~1.5 times) can be observed in PDPP-DTE and PDPP-DSE.[10] In both series of the polymers, DSE-variants tended to give more long-range ordering together with shorter $d_{\pi-\pi}$ due to the stronger interchain attraction between DPP and DSE units. Contrary, Se-substitution of PNDI-DTE resulted in enhanced n-type charge transport,[38,39] which shows that Se-substitution has a great potential and versatility for applications. This is further supported by the fact that almost all conjugated polymers consist of thiophene-like S-containing units in their backbones. This method was also be applied to acceptor BBT units.[47]

1.4.4. Side group engineering

Initially introduced to solubilize the conjugated polymers, alkyl side groups have become an important unit to optimize both the optoelectronic properties and the film-forming properties of polymers.[63] Effect of alkyl substituents can be categorized into two, depending on whether their position affects the polymer backbone or not. For example, alkyl chains placed on neighboring units can create a steric hindrance and increase the backbone torsion, which in turn affects its π-conjugation and film-forming

properties.[64] On the other hand, changing the length and branching of alkyl groups do not alter the electronic properties of the polymer backbone, but control the film forming properties.[64–66] In addition, shorter alkyl substituents induce pre-aggregates in the deposition solution due to lowered solubility, which can give polymer films with larger crystallites.[67]



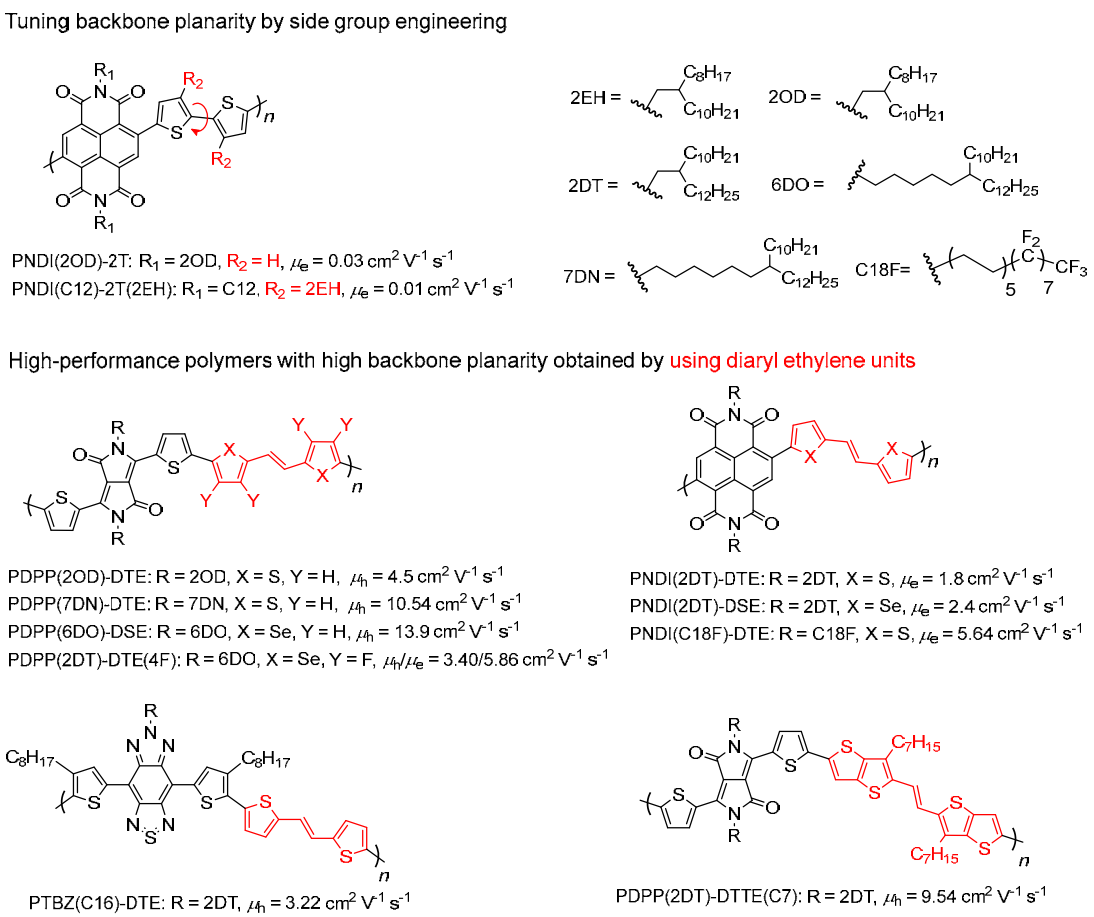
Scheme 1.5. Examples of side group engineering in semiconducting polymers.

Here we will focus on the optimization of the structure of the alkyl groups, while the effect on the polymer backbone is discussed in the next sub-section. Since branched side alkyl groups are mostly used in polymer designs, their lengths and branching points can be optimized. For example, by increasing the lengths of the branches of alkyl group

from 2-octyldodecyl (2OD) to 2-decyltetradecyl (2DT) in PDPP-DTEs, μ_h was enhanced from 4.5 to 8.2 $cm^2 V^{-1} s^{-1}$, respectively.[68] With other physical properties being identical, this was attributed to much closer π-π stacking distance in PDPP(2DT)-DTE (3.62 Å). Moving the branching point away from DPP unit by using 7-decylnonadecyl (7DN) resulted in the μ_h of 10.54 $cm^2 V^{-1} s^{-1}$.[10] Similar results were observed for PDPP(2OD)-DSE (4.4 $cm^2 V^{-1} s^{-1}$) and PDPP(7DN)-DSE (12.04 $cm^2 V^{-1} s^{-1}$). In both cases, 7DN-based polymers had much stronger long-range ordering in lamellar direction, as well as smaller $d_{\pi-\pi}$ (~3.6 Å) compared to 2DT-based counterparts (~3.7 Å). Similar optimizations have been performed for series of PNDI-2T[36] and PIID-2T.[31] A systematic study of the branching point position in PDPP-DSE showed that polymers with even number of C atoms between the DPP and the branching point resulted in tighter d_L and higher μ_h.[11]

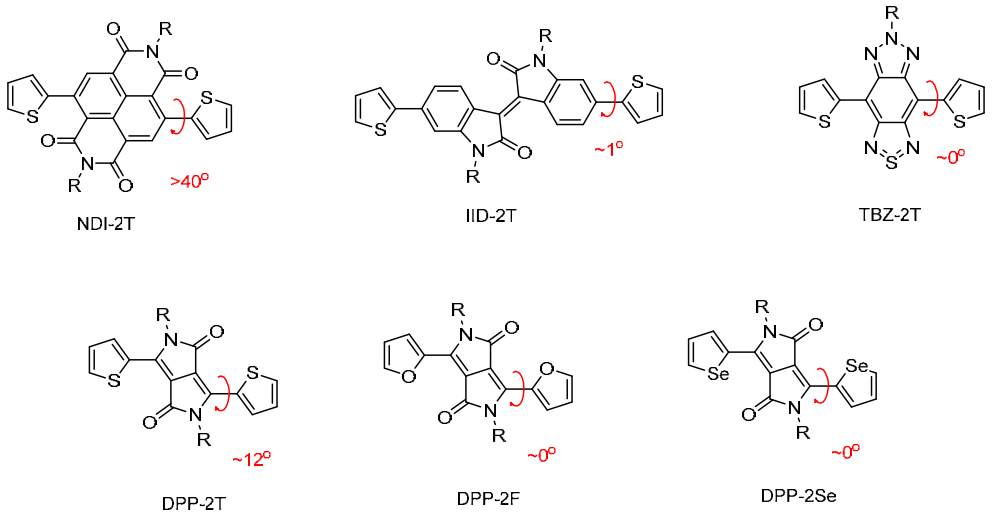
It is worth noting that besides alkyl groups, functionalized side groups/chains (e.g, polyethylene glycol, fluoroalkyls, etc.) can also be used.[69] For example, PNDI-2T and PNDI-DTE polymers containing semifluoroalkyl side groups gave enhanced μ_e above 5 $cm^2 V^{-1} s^{-1}$.[35] Despite the increasing $d_{\pi-\pi}$ from ~3.8 to ~4.1 Å, polymers exhibited great rigidity of the polymer backbone induced by highly ordered interdigitation of the fluorinated side groups.

1.4.5. Backbone planarity tuning



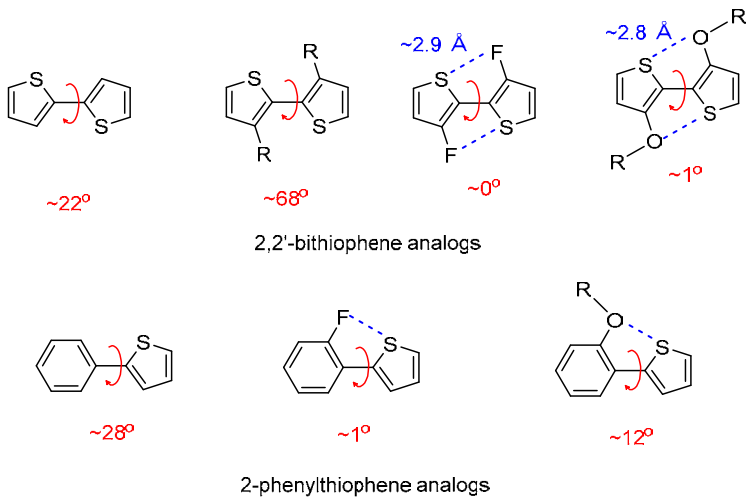
Scheme 1.6. Examples of backbone planarity tuning in semiconducting polymers.

Backbone coplanarity can facilitate strong conjugation length and tight π-π stacking. One of the factors that affects the backbone planarity is the hindrance between side groups of neighboring units.[70] For example, PNDI-2T films with 3,3'-dialkyl-2,2'-bithiophene units had no defined π-π stacking and the μ_e decreased by nearly 3 times compared to the polymer with unsubstituted 2,2'-bithiophene (Scheme 1.6).[37]



Scheme 1.7. Dihedral angles between NDI, IID, TBZ, DPP acceptors and their flanking units.

Backbone planarity also depends on the steric hindrance between the conjugated units themselves. For example, DPP-2T has a dihedral angle of 12°,[71] while NDI-2T has a dihedral angle of >40°.[72] On the other hand, IID-2T and TBZ-2T exhibit almost planar backbones (Scheme 1.7).[73,74] Heteroatom substitution can improve the backbone coplanarity. For example, DPP-2F gave more planar backbone than DPP-2S due to smaller O atoms in furan units compared to S atoms in thiophene units.[71] However, although Se atoms are larger than S, DPP-2S also showed highly planar structure, which was attributed to the strong attractive interaction between Se of selenophene unit and O of DPP unit.

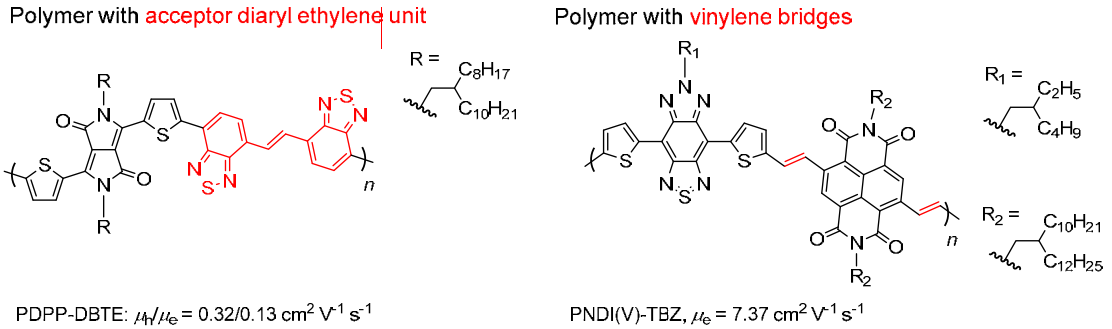


Scheme 1.8. Enhancement of coplanarity by "conformational locks" in T−T and Ph−T units.

Attractive interactions between pairs of atoms with large difference in electronegativity, such as halogen···sulfur (X···S), oxygen···sulfur (O···S), and nitrogen···sulfur (N···S), can be used to improve the planarity of conjugated backbone (Scheme 1.8).[75–78] Theoretical calculations and crystallography showed that in molecules containing such "conformational locks" the actual distance between the involved atoms is significantly shorter than the sums of their van der Waals radii.[79,80] In addition to these, hydrogen bonding was also employed to planarize conjugated backbone in semiconducting polymers.[51]

Inclusion of a planarizing moiety between aryl units is also an effective method to obtain highly rigid conjugated backbone. Vinylene bridge in diarylethylenes (DAE) units is one of the notable examples.[81] Extensively studied DAE donor units are dithiophenylethylene (DTE), diselenophenylethylene (DSE) and dithieno[3,2-

b]thiophenylethylene (DTTE). For example, PDPP(2OD)-DTE gave μ_h of 4.5 $cm^2\ V^{-1}\ s^{-1}$,[69] while PDPP(2OD)-4T was reported to exhibit μ_h = 0.97 $cm^2\ V^{-1}\ s^{-1}$.[56] PDPP(2OD)-DTE exhibited long-range ordered π-π stacking compared to PDPP(2OD)-4T. Thus, it is not surprising that for many acceptor units, their DAE-based copolymers exhibited very high μ: PDPP(7DN)-DTE (μ_h = 10.54 $cm^2\ V^{-1}\ s^{-1}$),[10] PDPP(6DO)-DSE (μ_h = 13.9 $cm^2\ V^{-1}\ s^{-1}$),[11] PDPP(2DT)-DTE(4F) (μ_h/μ_e = 3.40/5.86 $cm^2\ V^{-1}\ s^{-1}$),[29] PNDI(2DT)-DTE (μ_e = 1.8 $cm^2\ V^{-1}\ s^{-1}$),[38] PNDI(2DT)-DSE (μ_e = 2.4 $cm^2\ V^{-1}\ s^{-1}$),[39] PNDI(C18F)-DTE (μ_e = 5.64 $cm^2\ V^{-1}\ s^{-1}$),[35] PTBZ(C16)-DTE (μ_h = 3.22 $cm^2\ V^{-1}\ s^{-1}$),[48] and PDPP(2DT)-DTTE(C7) (μ_h = 9.54 $cm^2\ V^{-1}\ s^{-1}$).[82]

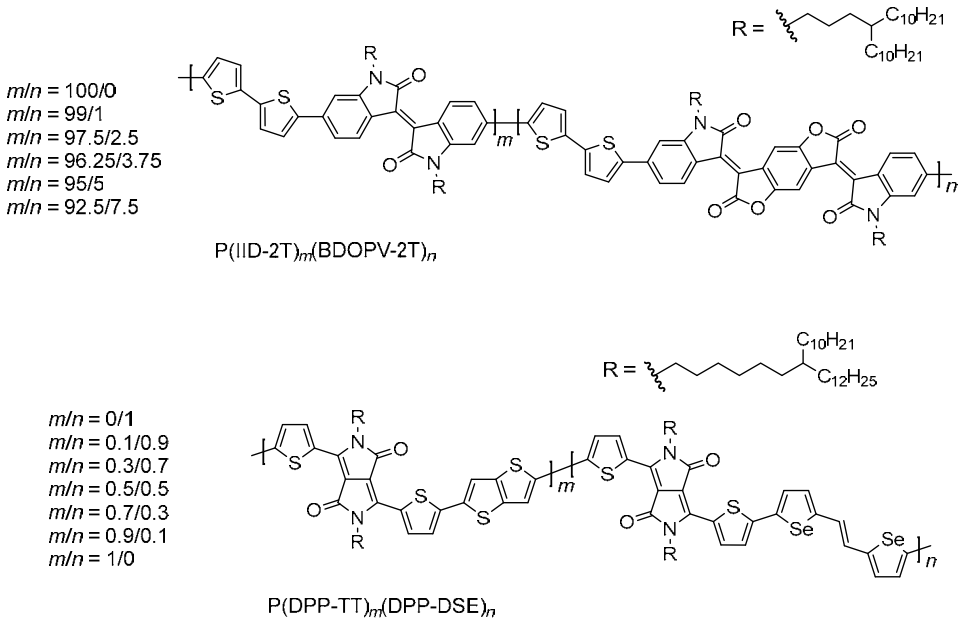


Scheme 1.9. All-acceptor polymers utilizing planarizing vinylene bridge in conjugated backbone.

Similar bridging units were applied to the acceptor units as well. For example, PDPP-DBTE gave balanced μ_h/μ_e of 0.32/0.13 $cm^2\ V^{-1}\ s^{-1}$, thanks to very high crystallinity and short $d_{\pi-\pi}$ of 3.66 Å (Scheme 1.9).[83] This approach was then further expanded into bridging different acceptor units. For example, vinylene bridged PNDI(V)-TBZ exhibited μ_e of 7.16 $cm^2\ V^{-1}\ s^{-1}$,[51] while the same units without

vinylene bridges (i.e., PNDI-TBZ) gave μ_e of 5.35 cm^2 V^{-1} s^{-1}.[50]

1.4.6. Random copolymerization



Scheme 1.10. Examples of random copolymers.

Incorporation of a third structural unit into D-A polymers is another effective way to tune the electronic structures of the polymers, without having to re-design the already established building blocks. For example, random copolymers prepared by incorporating low levels of BDOPV into PIID-2T gave optimized μ_h of 7.01 cm^2 V^{-1} s^{-1} at the loading ratio of 2.5mol%, while the original PIID-2T had μ_h = 2.10 cm^2 V^{-1} s^{-1} (Scheme 1.10).[84] The random copolymer had minimally deepened E_{LUMO} from −3.57 to −3.61, while E_{HOMO} was practically identical. In addition, the $d_{\pi\text{-}\pi}$ decreased from 3.51 to 3.49 Å. It is worth noting that, PBDOPV-2T was earlier reported as an n-

type polymer with μ_e = 1.74 cm^2 V^{-1} s^{-1}.[41] Although adding completely unrelated structures is possible,[85] in general, incorporation of units with similar structures gives better results, due to the similarities in molecular packing. As a result, structures optimized by controlling acceptor/donor ratio, heteroatom substitution, alkyl side chain engineering, and incorporation of conformational locks can be used to prepare random copolymers.[86] In other words, random copolymerization approach allows to achieve trade-off between positive and negative effects of each optimization method. For example, in a series of random copolymers based on PDPP-DSE and PDPP-TT,[87] the μ_h gradually increased from 3 to 9 cm^2 V^{-1} s^{-1} with increasing DSE-content, while the solubility, E_{LUMO} and $E_{g,opt}$ exhibited increasing-decreasing trends.

1.4.7. Molecular weight distribution

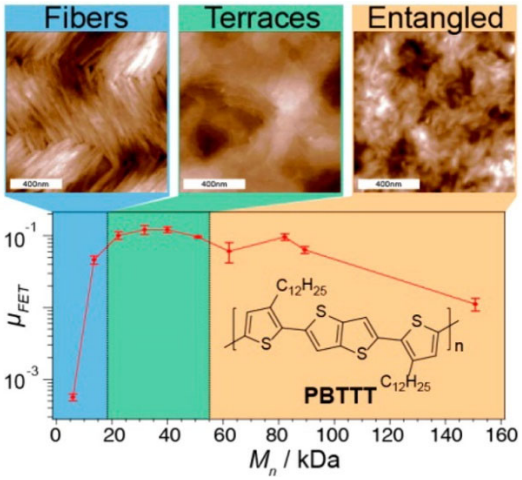


Figure 1.6. Dependence of film morphology and μ_h on M_n in PBTTT. Reproduced with permission.[88] Copyright (2021) American Chemical Society.

Polymers with large molecular weights can form semicrystalline films where crystallites are interconnected by long polymer chains that serve as inter-domain charge transport pathways.[55] For example, PBTTT with low number-averaged molecular weight (M_n) of 5–20 kDa formed fibers, in which the crystalline domains hardly interconnected (Figure 1.6).[88] With increasing M_n (20–50 kDa), polymer chains formed interconnecting "terraces" with neighboring domains. However, when the M_n was further increased (50–151 kDa), rough surface morphology was observed due to the entanglement of long polymer chains. Authors suggested that entanglement of polymer chains led to a substantially increased lamellar spacing at M_n = 89.7 kDa. As a result, the μ_h of the films increased quickly, saturated, and degraded as the M_n was increased. Similar trend was demonstrated in DPP-based polymers.[89] In both works, blending the low-M_n fraction with high-M_n fraction led to μ_h values comparable to those of pure high-M_n fractions. This further supported the hypothesis that long polymer chains formed interconnecting pathways for charge transport between fiber-like crystalline domains formed mostly by the low-M_n fraction.

1.4.8. Improving device fabrication conditions

Aspects of the OFET fabrication process that affect the film morphology and microstructure include selection of solvent, film thickness, post-deposition treatment

(e.g., thermal annealing), film deposition method. In addition to these, device configuration also plays an important role.

1.4.8.1. Device Architecture

Bottom-gate designs are often employed due to commercial availability of high-quality heavily n-doped Si (n^+-Si) wafers with a thermally grown SiO_2 layer, where the latter acts as dielectric.[53] In top-gate configurations, the dielectric layer atop the semiconducting material can protect it against ambient atmosphere. For example, PDPP-TT in TGBC device configuration showed ambipolar charge transport with μ_h/μ_e of 1.36/1.56 $cm^2\ V^{-1}\ s^{-1}$,[26] while earlier bottom-gate device configurations gave unipolar p-type charge transport (0.94 $cm^2\ V^{-1}\ s^{-1}$).[24] By further improving the device fabrication conditions, μ_h = 10.54 $cm^2\ V^{-1}\ s^{-1}$ was reported for PDPP-TT films later the same year (see below).[9] Similarly, *N*-substituted PIID-2T gave p-type charge transport in BGBC architecture with μ_h = 7.28 $cm^2\ V^{-1}\ s^{-1}$, while TGBC devices exhibited μ_h/μ_e = 2.33/0.78 $cm^2\ V^{-1}\ s^{-1}$.[33] These examples showed how device configuration and fabrication processes can dramatically affect the performances. Another factor to consider during the fabrication of top-gate OFETs is that the solvent used for deposition of organic dielectric must be inert to the semiconductor layer.[53] Furthermore, charge carriers generated at the dielectric-semiconductor interface are more prone to trapping

due to the roughness of the semiconductor surface.

Due to the preparation of source and drain contacts before the semiconductor layer deposition in bottom-contact devices, high-precision techniques can be used to obtain narrow channel length and width.[53] For example, PDPP-TT showed μ_h of up to 8.0 $cm^2 V^{-1} s^{-1}$ in BGTC devices with W/L = 4000/100 μm, while μ_h of up to 10.5 $cm^2 V^{-1} s^{-1}$ was obtained by using BGBC architecture that had W/L = 1400/40 μm.[9]

1.4.8.2. Film deposition

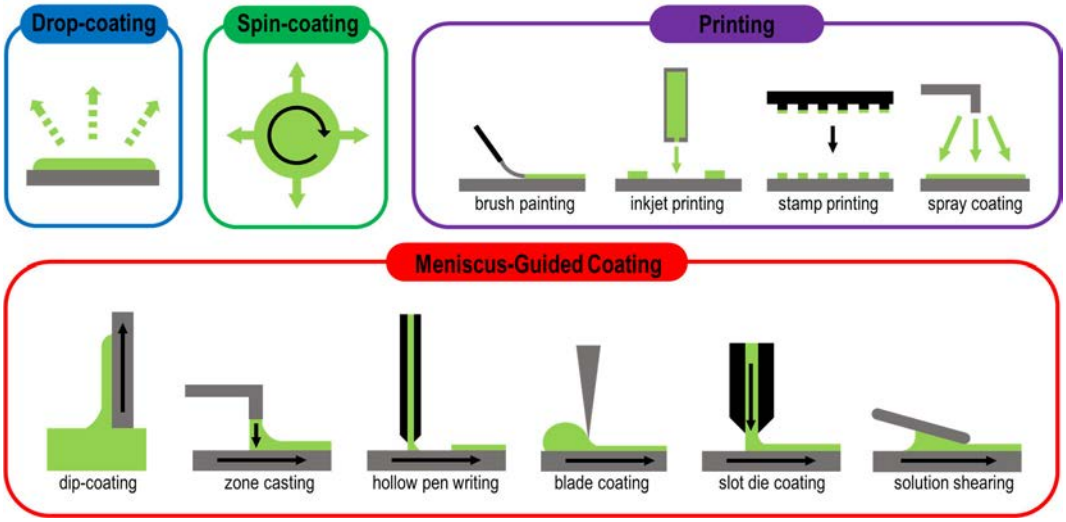


Figure 1.7. Illustration of solution-based deposition techniques for polymer films. Adapted under Creative Commons Attribution 3.0 Unported Licence.[5] Colors were modified.

There are numerous polymer film preparation methods at the disposal of researchers: drop-casting, spin-coating, printing and meniscus-guided coating techniques (Figure 1.7).[5] Printing and meniscus-guided coating techniques are ideal for large-area applications. However, these techniques for polymeric semiconductors

are still relatively underdeveloped due to the non-equilibrium conditions during the drying step. Nevertheless, a full-adder circuit was demonstrated using PNDI(2OD)-2T as n-type semiconductor with inkjet-printing technique.[90] Meniscus-guided coating methods can be used to achieve anisotropic alignment of polymer chains which could potentially give better charge transport along one of the axes. For example, solution sheared PTDPP(2DT)-DTTE films exhibited μ_h of 7.43 $cm^2 V^{-1} s^{-1}$, while spin-coated films had μ_h = 3.13 $cm^2 V^{-1} s^{-1}$.[91] Researches are being done to improve the uniformity of the films (hence, of the OFET performances) prepared by meniscus-guided techniques.[92]

Spin-coating is by far the most reported method in research publications due to simplicity of the process, uniformity of prepared films and high reproducibility. As mentioned earlier, Si/SiO_2 substrates are often employed for OFET fabrication.[53] Surface-modifiers, used to facilitate the deposition of polymers onto SiO_2 surface, can be roughly classified as self-assembly monolayers (SAMs) and polymeric materials. SAM can be prepared from silanes (e.g., alkyltrichlorosilanes, alkyltrimethoxysilanes, etc.) by chemically binding the silane center to the SiO_2 surface.[93] On the other hand, polymeric materials (e.g., poly(methyl methacrylate), parylenes, Cytop®, etc.) are applicable in TGBC or TGTC configurations, since they can be deposited onto the semiconductor surface and can serve as protective layer as well.[94,95]

1.4.8.3. Film thickness, post deposition treatment and additives

Thickness plays an important role both in the crystallinity and the molecular packing orientation of the films. For example, thinner P3HT films exhibited better OFET performances due to the ultrathin layer of edge-on crystallites at the SAM-polymer interface.[96,97] Film thickness can be controlled by altering the deposition solvent, concentration of the solution and spin-coating rate.

Post-deposition treatments, such as thermal annealing and solvent vapor annealing can also affect the molecular packing and surface morphology of the films. [92,98,99] Heating the polymer film to glass transition or melting temperatures (i.e., thermal annealing) allows polymer chains to reorganize into crystallites with tightly packed polymer chains. In some cases, complete change of orientation was observed. For example, PNDI(2OD)-T2 annealed at 150–180 °C was highly crystalline with predominantly (77.5%) face-on orientation, while after annealing above melting temperatures (300–320 °C) polymer film retained its crystallinity but orientation changed to predominantly edge-on (94.5%).[98]

Small-molecule additives can be used to facilitate polymer packing orientation or its crystallization in general.[100] Ionic additives, such as organic salts, can interact with the polymer chains at an electronic level. For example, incorporation of tetramethylammonium iodide (Me_4NI) into PDPP-TT locked the side alkyl groups of DPP unit at certain angle due to attractive interaction between DPP and Me_4N^+.[101] This

resulted in improved stacking of polymer chains and the average μ_h was boosted from 0.8 to 19.5 $cm^2 V^{-1} s^{-1}$.

1.4.9. Topochemical polymerization

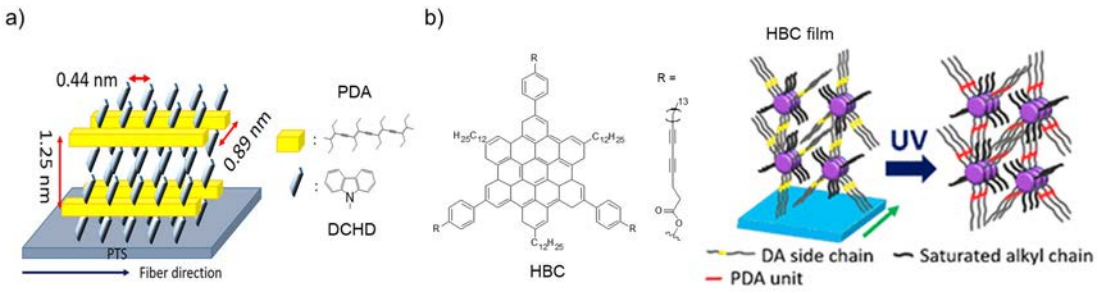


Figure 1.8. (a) PDA film for OFET applications prepared by topochemical polymerization of DCHD. Reproduced with permission.[103] Copyright (2021) John Wiley and Sons. (b) Topochemical polymerization of π-π stacked HBC by UV irradiation. Reproduced with permission.[104] Copyright (2021) American Chemical Society

Single crystals of polydiacetylenes (PDAs) are known to exhibit μ_h of up to 50 $cm^2 V^{-1} s^{-1}$.[102] The intriguing fact is that PDAs can be synthesized by topochemical 1,4-coupling polymerization of 1,3-butadiyne (diacetylene) monomers by ultraviolet (UV) light irradiation or thermal annealing. For example, photopolymerization of a 1,6-di-(*N*-carbazolyl)-2,4-hexadiyne (DCHD) film gave μ_h of 0.039 $cm^2 V^{-1} s^{-1}$.[103] If the butadiyne moieties are present in the side groups, the formation of PDA chains can "freeze" and improve the molecular packing motif of the starting material (Figure 1.8). For example, photopolymerization of hexa-peri-hexabenzocoronene (HPC) derivatives which had diacetylene-containing side groups was reported recently.[104] After UV

irradiation $d_{\pi\text{-}\pi}$ of the crystallites decreased by 0.05–0.1 Å owing to the formation of cross-links. As a result, the films exhibited μ_h = 1.5 cm^2 V^{-1} s^{-1}, which was 10^3 times higher than those of the monomeric films. The authors attributed the improvement to tighter packing induced by the cross-links and to the additional charge transport paths from the PDA backbone. Such a cross-linking approach can be expanded to polymeric semiconductors as well. For example, cross-linking of PIID-DTE was reported and the films retained their photophysical properties.[105] However, no application in OFETs was reported. Thus, cross-linking of semiconducting polymers by topochemical polymerization of butadiynes has a promising potential for obtaining photo-patternable films.

1.5. Concluding Remarks

In the development of each building block and related polymers one can see systematic improvements. After discovery of a building block, it is copolymerized with various other well-studied units. Then for the best combination, the energy levels are modulated to control the charge carrier type by introducing heteroatoms into the design. Solubilizing alkyl side groups are optimized to achieve the best possible molecular packing motif with edge-on/bimodal orientation and tight π-π stacking distance. In addition, polymers with high M_n are desired due to their facile film-forming properties.

During these optimizations, theoretical calculations are performed to evaluate polymer chain backbone because various conformations can have different backbone planarity and affect the overall electronic structure and the film-forming properties. Finally, OFET device preparation conditions are also optimized to ensure uniform film morphology that can give highly reproducible results. The stability of the devices is also evaluated at this point. As a consequence, design and development of semiconducting polymers for OFET applications requires good understanding of structure-property relationship in these materials.

The next chapters will demonstrate structure-property relationship in three series of polymers: PTBZ-DTTE, PDPP-4T and butadiyne-containing polymers. Firstly, OFET performances of PTBZ-DTTE polymers were optimized by side-chain engineering. The positions of alkyl chains were changed to alter the backbone coplanarity, which led to the best possible μ_h of 0.2 $cm^2 V^{-1} s^{-1}$. Flanking thiophenes of TBZ unit were found to be the main sources of backbone torsion, whose removal gave a polymer with an almost planar backbone and μ_h of 0.4 $cm^2 V^{-1} s^{-1}$. Next, methoxy groups were introduced into PDPP-4T polymer as conformational locks. To observe gradual change of the properties, the random copolymerization approach was applied by substituting 3,3'-dimethoxy-2,2'-bithiophene instead of 2,2'-bithiophene at loadings of 25, 50, 75 and 100mol%. At incorporation extent of 25mol%, a polymer

with OFET performances comparable to those of original PDPP-4T was obtained. Effect of an ionic additive on the charge transport was also studied. Finally, thin films of poly(arylenebutadiynylene)s (i.e., polymers with butadiyne units in the conjugated backbone) were cross-linked by UV irradiation and thermal annealing to study the effect of the cross-linking on the OFET performances. A polymer with a straight backbone demonstrated enhancement of μ_h due to improved molecular packing. On the other hand, a polymer with a zigzagged backbone failed to give long-range ordered molecular packing. The cross-links deteriorated the charge-transport pathways leading to complete loss of field-effect μ_h.

Chapter 2

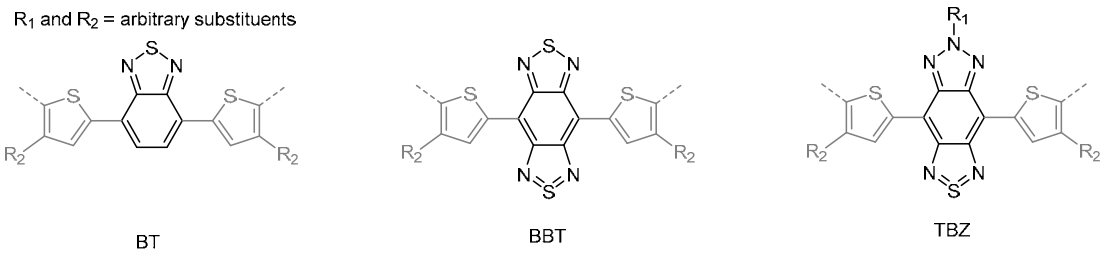
Backbone Planarity Tuning by Side-Chain Engineering

This chapter was adapted with permission from the published article: Otep, S.; Wang, Y.; Kohara, A.; Matsumoto, H.; Mori, T.; Michinobu, T. Tuning Backbone Planarity in Thiadiazolobenzotriazole-Bis(thienothiophenyl)ethylene Copolymers for Organic Field Effect Transistors. *ACS Appl. Polym. Mater.* **2019**, *1*, 2302–2312. https://doi.org/10.1021/acsapm.9b00329. Copyright (2021) American Chemical Society.

2.1. Introduction

TBZ is a promising building block of high-mobility D-A semiconducting polymers for OFET applications.[42] Its development can be traced back to BT, which was synthesized and characterized in 1970s, and first reported in D-A semiconducting polymers in 1996 (Scheme 2.1). To achieve higher electron mobilities, another electron deficient fused ring was added to the BT unit to give BBT, which lowered its LUMO level.[42] For example, a copolymer of DPP and BBT (PDPP-BBT) exhibited balanced μ_h/μ_e of 1.17/1.32 $cm^2\ V^{-1}\ s^{-1}$.[45] Main disadvantage of BBT is its low solubility, due to the lack of a position for side group substitution. In 2011, by changing one of the

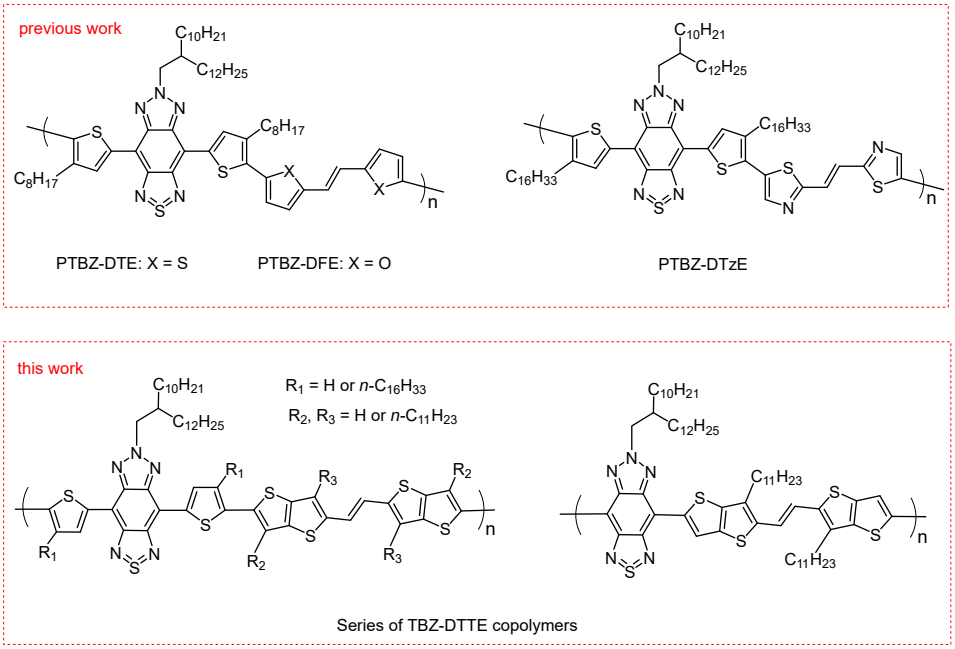
thiadiazole rings in BBT to a triazole ring, Grimsdale et al reported the TBZ unit, which had a position available for solubilizing alkyl chain substitution.[106] This unit had shallower E_{LUMO} and E_{HOMO} than BBT, resulting in more p-type dominant copolymers when polymerized with identical donor units.[47]



Scheme 2.1. Structures of BT, BBT and TBZ. Flanking thiophene units are shaded. R_1 and R_2 are arbitrary substituents (usually long and/or branched alkyl groups to improve solubility and control the thin film molecular packing).

DAE donor unit was first reported as DTE in PDPP-DTE polymer in 2012, which exhibited μ_h of 4.5 $cm^2 V^{-1} s^{-1}$ for 2-octyldodecyl substituted polymer and μ_h of 8.2 $cm^2 V^{-1} s^{-1}$ for 2-decyltetradecyl substituted polymer.[68] Other DAE structures widely-reported in literature include DSE, DTTEs, and difluorophenylethylenes (DFPEs). For example, a series of PDPP-DSE polymers exhibited ultrahigh μ_h values exceeding 12 $cm^2 V^{-1} s^{-1}$.[10,11] DTTE forms a more extended and planar π-conjugated core compared to DTE in the polymer backbone. In addition, there are several positions for side chain engineering. Effect of substituted alkyl group position of DTTE was studied in PDPP-DTTE polymers. The highest μ_h of 9.54 $cm^2 V^{-1} s^{-1}$ was obtained for 3,3'-substituted

DTTE,[82] while polymer with 6,6'-substituted DTTE showed μ_h of 0.72 $cm^2 V^{-1} s^{-1}$.[107] These can be compared to the polymer with the same backbone and unsubstituted DTTE unit, which exhibited μ_h = 3.13 $cm^2 V^{-1} s^{-1}$,[91] under similar conditions. As it was revealed by theoretical calculations, the dihedral angle between DTTE and neighboring thiophene ring was high in 6,6'-substituted DTTE (37.8°), while other two units showed moderate values (≈17°).[107]



Scheme 2.2. Structures of TBZ-DAE based copolymers reported previously, and those of TBZ-DTTE based copolymers developed in this work.

Recently, copolymerization of TBZ with electron rich DTE and difuranylethylene (DFE) units resulted in p-type semiconducting polymers (Scheme 2.2), which showed μ_h of 3.22 and 1.21 $cm^2 V^{-1} s^{-1}$, respectively.[48] Introduction of electron deficient dithiazolylethylene (DTzE) resulted in ambipolar polymers with μ_h/μ_e of 0.027/0.16

$cm^2\ V^{-1}\ s^{-1}$.

To further develop TBZ-based high-performance polymers, this work focuses on the synthesis and characterization of a series of novel TBZ-DTTE based copolymers. In addition to the alkyl substitution positions of DTTE unit, alkyl substituents on the thiophene flanking units of the TBZ were modified as well. These modifications not only controlled the backbone planarity, but also significantly impacted the solubility of the polymers. Thus, five polymers differing in the alkyl chain positions were synthesized and their OFET performances were evaluated. Optical and electrochemical properties as well as film microstructures and theoretical calculation results were used to determine the effect of the substituent position on the charge-transport properties. Copolymers based on the 3,3'-substituted DTTE unit exhibited μ_h of up to 0.18 $cm^2\ V^{-1}\ s^{-1}$, while 6,6'-substitued DTTE gave μ_h of ~0.01 $cm^2\ V^{-1}\ s^{-1}$. In addition to these polymers, to further improve the backbone planarity and the electronic structure of the polymer, thiophene flanking units were removed from the backbone, giving the sixth polymer. This approach led to the further improved μ_h of 0.44 $cm^2\ V^{-1}\ s^{-1}$.

2.2. Materials and Methods

2.2.1. Materials

All chemicals were purchased from Tokyo Chemical Industry (TCI), Kanto Chemical, Co., Inc., and Sigma Aldrich, and were used as received. Acceptor units **A1**, **A2** and **A3** were synthesized following identical or slightly modified reaction protocols as reported in literature.[48,108–110] Donor units **D1**, **D2** and **D3** were prepared adopting the reported procedures.[82,91,107,111,112] Polymerization procedures for **P1–P6** were performed as reported.[48] The polymerization conditions were modified where necessary.

2.2.2. General measurements

Proton nuclear magnetic resonance (^{1}H NMR) and carbon-13 nuclear magnetic resonance (^{13}C NMR) spectra were recorded by a JEOL AL-300 (300 MHz) spectrometer at room temperature. Deuterated chloroform ($CDCl_3$) was used as the solvent and the chemical shifts were reported in parts per million (ppm) relative to the residual solvent peak at 7.26 ppm for ^{1}H NMR and 77.23 ppm for ^{13}C NMR. Coupling constants *J* were given in Hertz. The resonance multiplicity was described as singlet (s), doublet (d), triplet (t), multiplet (m) and broadening (br).

The matrix assisted laser desorption/ionization time of flight (MALDI-TOF) mass spectra were measured by a Shimadzu/Kratos AXIMACFR mass spectrometer equipped with a nitrogen laser (λ = 337 nm) and pulsed ion extraction, which was operated in the linear-positive ion mode at an accelerating potential of 20 kV. Test samples were prepared by dropping 1 μL aliquots of tetrahydrofuran (THF) solutions containing a test compound, dithranol (matrix) and CF_3COONa at the concentrations of 1, 20 and 1 g L^{-1}, respectively.

Gel permeation chromatography (GPC) was measured by a JASCO GULLIVER 1500 equipped with the pump (PU-2080 Plus), absorbance detector (RI-2031 Plus), and two Shodex GPC KF-803 columns (8.0 mm I.D. × 300 mm L) at 40 °C. The flow rate was 0.5 mL min^{-1} for the *o*-dichlorobenzene (*o*-DCB) eluent. The M_ns and polydispersity indexes (PDIs) were calculated based on the calibration curves using polystyrene standards.

Elemental analysis (CHN content) was performed on JM10 (J-Science Co.) with combustion temperature and time of 950 °C and 4 min, respectively. Helium was used as carrier gas and the amount of resulting gases was determined with thermal conductivity detector.

Thermogravimetric analysis (TGA) and differential scanning calorimetry (DSC) measurements were carried out using a Rigaku TG8120 and Rigaku DSC8230,

respectively, for 3–5 mg samples under flowing N_2 at the heating rate of 10 °C min^{-1}. Decomposition temperature (T_d) was estimated as the temperature corresponding to the 5% weight loss in TGA curves. Glass transition temperature (T_g) was determined from the step changes in DSC curves. Melting points (m.p.) of the acceptor and donor monomer units were determined from the peaks of endotherms in heating cycles of DSC curves.

Ultraviolet–visible–near-infrared (UV–vis–NIR) spectra were recorded by a JASCO V-670 spectrophotometer for 0.03 mg mL^{-1} solutions or thin films deposited on a glass substrate from 2–3 mg mL^{-1} of the sample solutions in either chloroform or chlorobenzene. Optical energy gap ($E_{g,opt}$) was estimated from the onset of the absorption band in as-cast thin films as $E_{g,opt} = \lambda_{onset}/1243$ {eV}. Prior to film deposition, the glass substrates were pre-cleaned by subsequent sonication in water, acetone and isopropanol, followed by drying under hot air gun.

Cyclic voltammetry (CV) measurements were performed on a BAS electrochemical analyzer model 612C at room temperature in a three-electrode cell at the sweep rate of 0.01 V s^{-1}. The working, reference, and auxiliary electrodes were a glassy carbon, Ag/AgCl, and Pt wire, respectively, while 0.1 M tetrabutylammonium perchlorate ($(C_4H_9)_4NClO_4$) in acetonitrile was used as electrolyte. Polymer films were drop cast onto the working electrode from 2–3 mg mL^{-1} of the sample solutions in

chloroform or chlorobenzene. Positive and negative sweeps were measured from separate samples at a rate of 0.01 V s^{-1}. Electrolyte was bubbled with Ar for 5–10 min before every run. Electrolyte was renewed before the measurements of a new polymer. From the positive and negative sweeps, the onsets of corresponding oxidation and reduction peaks vs. Ag/AgCl electrode (φ_{ox} and φ_{red}, respectively) were recorded. For calibration, the redox potential of ferrocene/ferrocenium (Fc/Fc^+) vs. Ag/AgCl electrode ($\varphi_{Fc/Fc+}$) was measured under the same conditions. It was assumed that the redox potential of Fc/Fc^+ has an absolute energy level of −4.80 eV to a vacuum ($E_{Fc/Fc+}$).[48] Then E_{HOMO} and E_{LUMO} of the samples were calculated according to the following equations:

$$E_{HOMO} = E_{Fc/Fc+} - \varphi_{ox} + \varphi_{Fc/Fc+} \{eV\}$$

$$E_{LUMO} = E_{Fc/Fc+} - \varphi_{red} + \varphi_{Fc/Fc+} \{eV\}$$

Since for most polymers reduction peak was unclear, additionally, E_{LUMO} was estimated using optical band gap as $E_{LUMO} = E_{HOMO} + E_{g,opt}$.

2.2.3. Theoretical calculations

Density functional theory (DFT) calculations were performed on Gaussian 09 software using GaussView 5 program to build input structures and visualize results.[113,114] All

side alkyl chains were reduced to methyl groups to save computational time. B3LYP/6–31G(d) basis set was used for all calculations.

2.2.4. OFET fabrication and characterization

BGTC OFET devices were fabricated on n^+-Si with a thermally grown 300-nm-thick SiO_2 layer (C_i = 13.7 nF cm^{-2}). The SiO_2 surface was modified by the SAM of octadecyltrimethoxysilane (OTMS) by the reported method.[93] First, the substrates (1 × 1 cm^2) were cleaned by sequential sonication in distilled water, acetone, and 2-propanol for 10 min each, followed by a treatment with ultraviolet light irradiation for 20 min. A solution of 3 mM OTMS in trichloroethylene (100 μL) was then dropped onto the substrates and held for 10 s to allow self-assembly. After the substrates were spun at 3000 rpm for 10 s to remove the residual solvent, they were placed in a closed container with a small amount of ammonia overnight in order to chemically fix the SAM layer. The substrates were finally washed with water to remove any excess ammonia and sonicated in toluene to remove the excess OTMS. Polymer thin films were deposited onto the treated substrates by spin-coating 3–5 mg mL^{-1} of the sample solutions in selected solvents in an Ar-filled glovebox, followed by thermal annealing at temperatures of 150–300 °C. After the polymer thin film deposition, an ~40 nm thick gold layer was vacuum deposited as the source and drain contacts using a shadow mask

(*W*/*L* of 100/1000 μm). Current-voltage (*I*-*V*) performances were measured under ambient conditions using a Keithley 4200 parameter analyzer. The μ_h values were extracted from transfer curves in saturation regime.[48,52,53]

2.2.5. Film morphology and microstructures

For the grazing-incidence wide-angle X-ray scattering (GIWAXS) and tapping mode atomic force microscopy (AFM) measurements, samples were prepared by the methods similar to those of the OFET devices: polymer films were spin-coated onto n^+-Si/SiO_2/OTMS substrates, followed by thermal annealing.

GIWAXS measurements were carried out at BL40B2 in a SPring-8 (Hyogo, Jap an). The samples were irradiated at a fixed incidence angle on the order of 0.125°, and the GIWAXS patterns were recorded with a 2D image detector (PILATUS3 S 2M, Dectris, Ltd.). The wavelength of the X-ray beam was 1 Å, and the camera length was 350 mm. X-ray diffraction (XRD) patterns were obtained using a Bruker AXS D8 DISCOVER with GADDS (Cu Kα, wavelength = 0.154 nm) operated at 50 kV and 22 mA. The samples were exposed to the X-ray beam for 5 min with a sample-to-film distance of 200 mm. Scattering vectors, *q*, parallel (in-plane) and perpendicular (out-of-plane) to the sample surface were defined as q_x and q_z, respectively. Peaks corresponding to (*h*00) and (010) planes were assigned as described in literature.[54] Presence of intense (*h*00) reflections on q_z or q_x axes was considered as indication of

edge-on or face-on packing, respectively, while the absence was considered as a sign of amorphousness of the film. The d_L and $d_{\pi\text{-}\pi}$ were calculated from (100) and (010) reflections, respectively, using Bragg's equation.

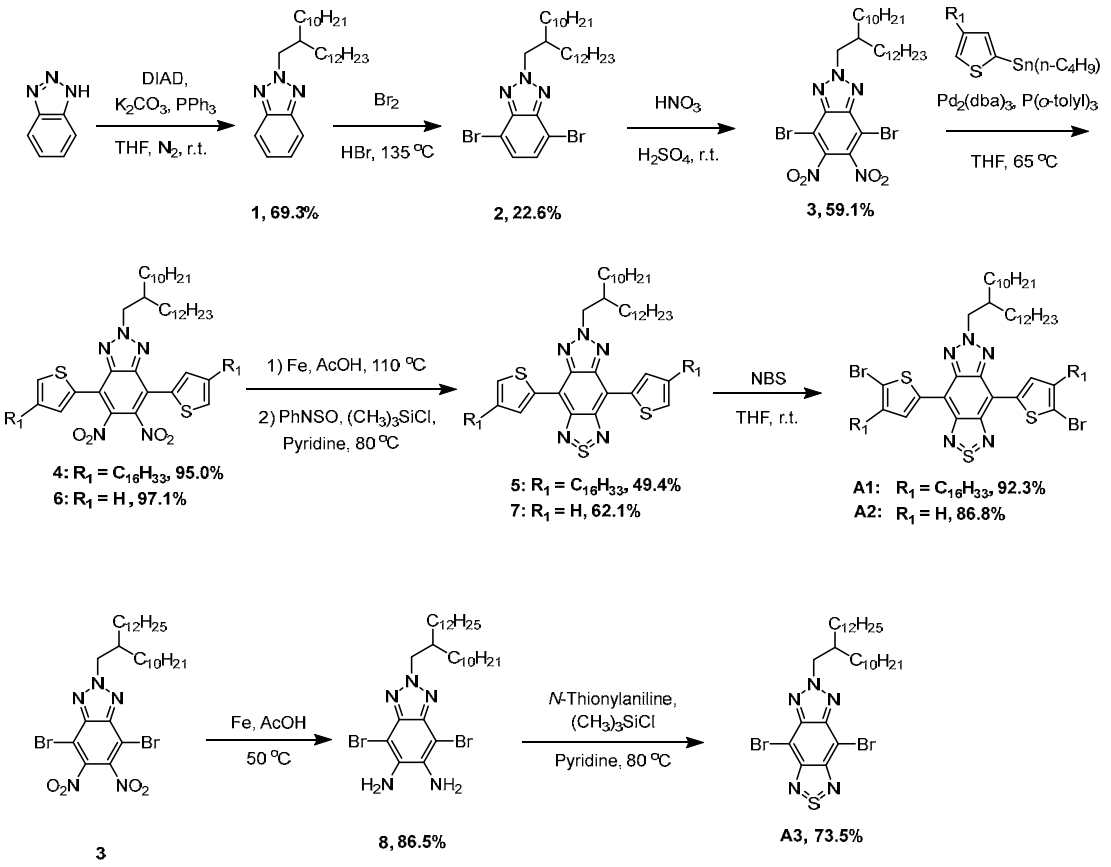
Tapping-mode AFM measurements were conducted using a Seiko Instruments SPA-400 with a stiff cantilever Seiko Instruments DF-20.

2.3. Results and Discussion

2.3.1. Polymer synthesis

Acceptor units **A1** and **A2** were synthesized starting from benzotriazole (Scheme 2.3). Firstly, *N*-hydrogen in benzotriazole was substituted with 2-decyltetradecyl in the presence of diisopropyl azodicarboxylate (DIAD), K_2CO_3 and triphenylphosphine (PPh_3) under inert atmosphere to give **1** in 69.3% yield.[108] The rest of the reaction conditions in the synthesis of **A1** and **A2** were adopted from literature.[48] Thus, bromination of **1** was done with Br_2 in refluxing 48% HBr to give **2**. Low yield of 22.6% in this reaction was associated with difficulty of controlled electrophilic substitution of benzotriazole at the 4,7-positions, giving 4-monobrominated compound as a major by-product. It is interesting to note that the latter can be isolated and used for the synthesis of alternative acceptor units. Next, **2** was nitrated with nitric acid in the presence of sulfuric acid under ambient conditions to afford **3** with 59.1% yield. Although higher

yield (≈70%) was reported for nitration in the presence of trifluoromethanesulfonic acid,[109] sulfuric acid was used due to safety considerations. Substitution of the 4,7-positions of the benzotriazole **3** to 4-hexadecylthiophen-2-yl or thiophen-2-yl in the presence of tris(dibenzylideneacetone)dipalladium(0) ($Pd_2(dba)_3$) and tris(o-tolyl)phosphine (P(*o*-tolyl)$_3$) gave **4** (95.0% yield) and **6** (97.1% yield), respectively. Due to difficulty of controlling the purity of starting organotin compounds, they were used in excess. Nitro groups of **4** and **6** were converted into amino groups with Fe in hot glacial acetic acid (AcOH), followed by ring closure reaction with *N*-thionylaniline (PhNSO) in the presence of trimethylsilyl chloride ($(CH_3)_3SiCl$) to give **5** (49.4% yield) and **7** (62.1% yield), respectively. The higher yield of **7** was likely caused by its less hydrophobicity, which allowed it to better dissolve in AcOH during the reduction reaction. Finally, **5** and **7** were brominated with *N*-bromosuccinimide (NBS) to give **A1** (92.3% yield) and **A2** (86.8% yield), respectively. For the synthesis of **A3**, nitro groups of **3** were reduced with Fe in AcOH under milder conditions to give **8** (86.5%), which was subjected to thiazole-forming ring-closure reaction, giving **A3** (73.5%).[110] **A1** and **A2** were stable under ambient conditions, while **A3** quickly darkened. Therefore, **A3** was stored in a fridge (~10 °C), where no changes were detected after several months of storage.

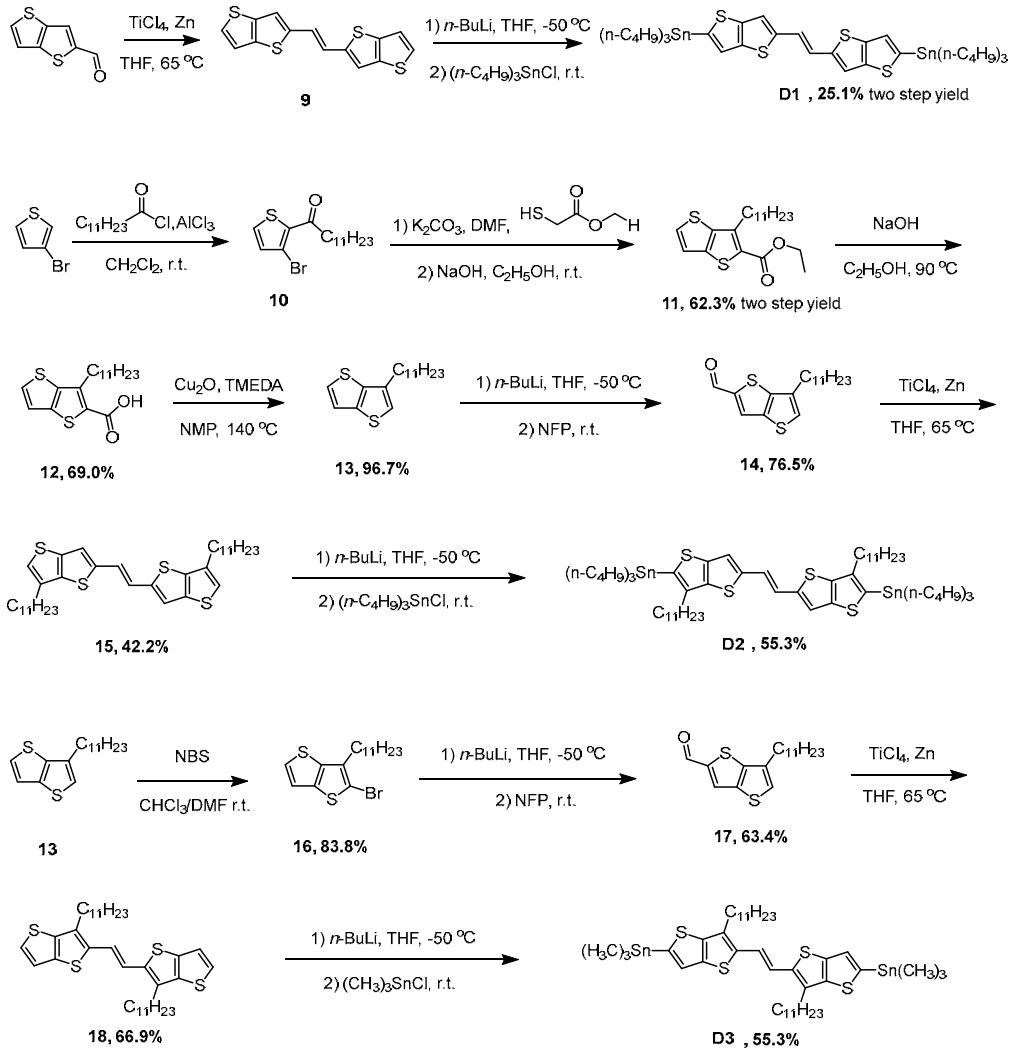


Scheme 2.3. Synthesis of acceptor monomers **A1**, **A2** and **A3**.

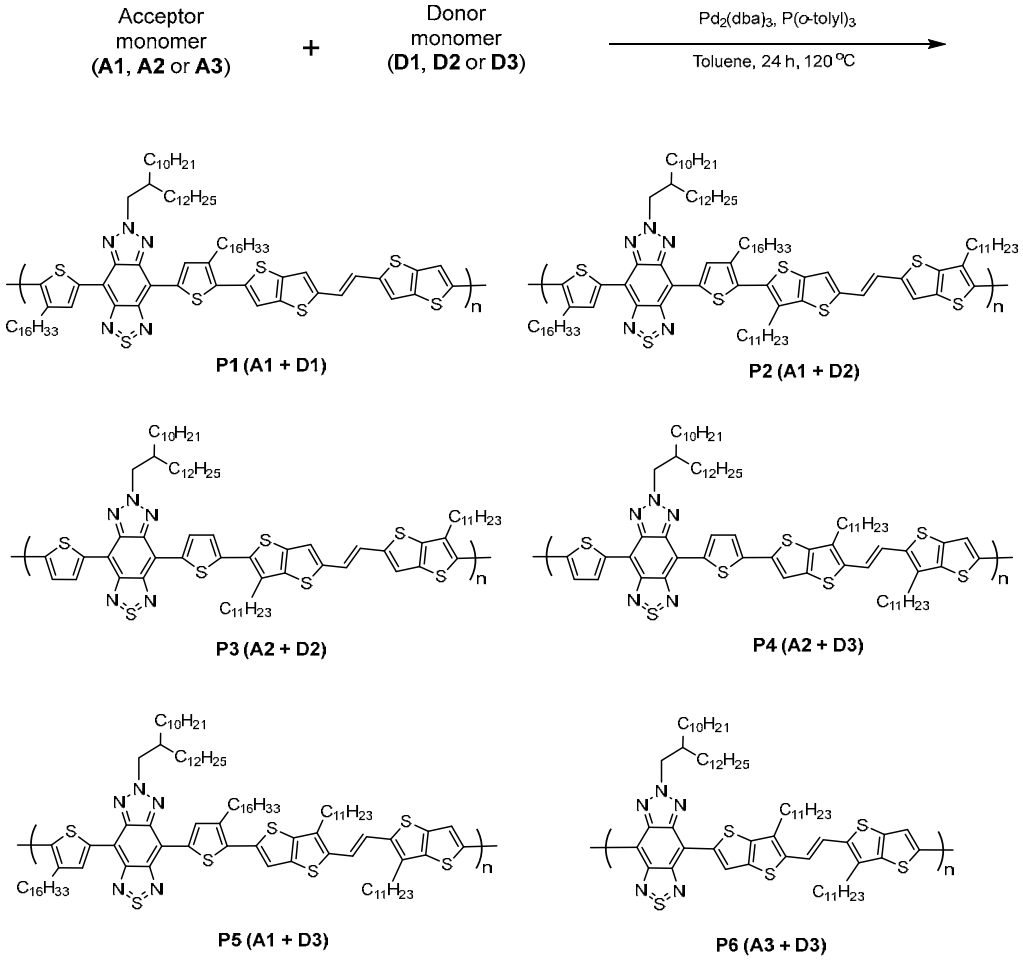
Donor units **D1**, **D2** and **D3** were synthesized by McMurry coupling from the corresponding carboxaldehyde precursors (Scheme 2.4). In all cases divalent titanium was preliminarily prepared by refluxing $TiCl_4$ and Zn in THF, to which the precursors were added. For the synthesis of **D1**, thieno[3,2-*b*]thiophene-2-carboxaldehyde was coupled to give **9**.[91] However, **9** was not fully isolated due to the low solubility, and was directly functionalized from the product mixture by step-wise treatment with n-butyllithium (*n*-BuLi) and tributylstannyl chloride ($(n\text{-}C_4H_9)_3SnCl$). Obtained stannane (**D1**) had a good solubility and could be purified by high-performance liquid

chromatography (HPLC) with the two-step yield of 25%. For the synthesis of **D2**,[111] firstly, 3-bromothiophene was acylated by Friedel-Crafts reaction to give **10** and its 2,4-isomer. Since the latter is inactive in the next reaction, this crude mixture was not further purified. Crude **10** was treated with ethyl thioglycolate in the presence of bases (K_2CO_3, NaOH) in dimethylformamide (DMF) to afford **11**, giving the two-step yield of 62.3%. The resulting ethyl ester (**11**) was hydrolyzed in the presence of NaOH to give **12** in 69.0% yield. In literature,[111] decarboxylation of the acid (**12**) is typically carried out with Cu in quinoline at 240 °C (in a Woods metal bath). Instead, applicability of a milder procedure, reported for the decarboxylation of aromatic acids,[112] was explored here. Thus, **13** was prepared in a high yield (96.7%) by treating **12** with Cu_2O and *N*,*N*,*N*',*N*'-tetramethylethylenediamine (TMEDA) in *N*-methyl-2-pyrrolidone (NMP) at 140 °C. Treatment of the obtained **13** with 1 eq. of nucleophilic *n*-BuLi resulted in 2-substituted intermediate, due to the higher acidity of the unsubstituted thiophene ring. Thus, **13** was converted into 2-carboxaldehyde by transferring the carboxyl group from *N*-formylpiperidine (NFP) via pre-treatment with *n*-BuLi to give **14** with 76.5% yield.[107] The latter was coupled by McMurry reaction to give **15** (42.2% yield), and subsequently functionalized with tributylstannyl to afford donor monomer **D2** (55.3% yield), as described above. Electrophilic substitution of **13** with NBS resulted in 6-substituted thieno[3,2-*b*]thiophene, thus allowed the synthesis of **D3**.[82] Hence, **16**,

obtained by bromination of **13** (83.8% yield), was treated with *n*-BuLi and then reacted with NFP to give **17** with 63.4% yield. McMurry coupling of **17** afforded **18** (66.9% yield), whose stepwise reaction with *n*-BuLi and trimethylstannyl chloride ($(CH_3)_3SnCl$) gave donor monomer **D3** (49.5% yield). To ensure high purity for polymerization reactions, all donor units were purified by HPLC, whereas in literature organotin compounds are occasionally not purified due to their instability to silica gel used in column chromatography.



Scheme 2.4. Synthesis of donor monomers **D1**, **D2** and **D3**.



Scheme 2.5. Synthesis of **P1–P6**. A typical condition for Pd-catalyzed Stille polycondensation is illustrated, see the text for details.

Polymers were prepared by Pd-catalyzed Stille polycondensation between the corresponding donor and acceptor monomers (Scheme 2.5). Typically, a donor monomer (1 eq.) and an acceptor monomer (1 eq.) were reacted in the presence of $Pd_2(dba)_3$ (1/15 eq.) and P(*o*-tolyl)$_3$ (1/4 eq.) in toluene at 120 °C for 24 h under N_2 atmosphere.[48] Polymerization reaction conditions for the synthesis of **P3**, **P4** and **P6** were modified. After the reaction, the resulting polymers were subjected to Soxhlet extraction sequentially with methanol, acetone, hexane, chloroform and chlorobenzene,

assuming that fractions with increasing molar weights are extracted in this order. Fractions containing the largest amounts of polymers were used for further characterization.

Table 2.1. Molecular weights and thermal properties of **P1–P6**.

	Soxhlet solvent [a]	M_n, **kg mol^{-1}**	**PDI**	T_d, **°C** [a]	T_g, **°C** [b]
P1	Chlorobenzene	13.4	1.3	398	119
P2	*n*-Hexane	5.3	1.7	373	66
P3	Chloroform	7.6	1.4	376	70
P4	Chloroform	5.7	1.4	378	126
P5	Chlorobenzene	8.5	1.2	381	149
P6-CF	Chloroform	3.0	1.2	383	130
P6-CB	Chlorobenzene	N/A	N/A	386	146

[a] Solvent used in Soxhlet extraction that contained the most fraction of polymers. [b] Temperature at which 5% weight loss occurred. [c] Onset in the 2nd heating cycle of DSC curves.

Among the polymers, the chlorobenzene fraction of **P1** displayed the highest M_n of 13.4 kg mol^{-1} with PDI of 1.3 (Table 2.1). **P2**, extracted with *n*-hexane, showed low M_n of 5.67 kg mol^{-1} (PDI = 1.49). Therefore, it was re-precipitated from *n*-hexane–acetone solution (1:1, v/v) to give higher M_n = 7.63 kg mol^{-1} (PDI = 1.54). After polymerization with the above procedure, the chloroform fraction of **P3** showed M_n of 6.04 kg mol^{-1} (PDI = 1.40). The M_n of the polymer was increased by adding CuI (1/5 eq.) to the polymerization reaction, as well as changing the solvent to chlorobenzene and increasing the reaction time to 48 h. After these changes, M_n of the chloroform fraction increased to 7.65 kg mol^{-1} (PDI = 1.37). During the synthesis of **P4**, an insoluble solid precipitated after 4 h of stirring, which was re-dissolved by adding more solvent. Its chloroform fraction exhibited the M_n of 5.7 kg mol^{-1} (PDI = 1.4). **P5** was

almost entirely extracted with chloroform (8.5 kg mol^{-1}, PDI = 1.2). The reaction mixture of **P6** became gel-like after 1 h of stirring, which separated into a homogeneous solution and precipitated upon dilution. The solution was further stirred overnight. Although a larger amount of **P6** was mainly extracted with chlorobenzene (**P6-CB**, 38%), the chloroform fraction (**P6-CF**, 3.0 kg mol^{-1}, PDI = 1.2, 16%) was also collected and characterized. The M_n of **P6-CB** could not be measured due to its limited solubility, and we assumed that the M_n of **P6-CB** was at least equal to or higher than that of **P6-CF**.

Table 2.2. Evaluation of CHNS(Br) elemental analysis results of **P1–P6**.

Elemental composition		**P1**	**P2**	**P3**	**P4**	**P5**	**P6-CF**	**P6-CB**
C, %	measured	69.08	71.85	68.13	67.91	72.50	69.71	69.72
	calculated	70.62	73.34	69.05	69.05	73.34	70.60	70.60
	corrected [(a)]	70.37	73.25	68.87	68.64	72.92	70.35	70.04
H, %	measured	8.67	9.87	8.09	8.13	9.83	9.10	9.30
	calculated	8.69	9.70	8.07	8.07	9.70	8.88	8.88
	corrected [(a)]	8.83	10.06	8.18	8.22	9.89	9.18	9.34
N, %	measured	4.77	3.93	5.40	5.43	4.04	5.87	5.99
	calculated	4.91	4.03	5.44	5.44	4.03	6.24	6.24
	corrected [(a)]	4.86	4.01	5.46	5.49	4.06	5.92	6.02
S, %	measured	15.65	12.44	17.30	17.47	13.05	14.41	14.54
	calculated	15.78	12.93	17.44	17.44	12.93	14.28	14.28
	corrected [(a)]	15.94	12.68	17.49	17.66	13.13	14.54	14.61
Total of measured, % [(b)]		98.17	98.09	98.92	98.94	99.42	99.09	99.55
Measured Br, %		0.13	1.17	0.09	0.00	0.00	0.00	0.00

[(a)] corrected = (measured × 100%)/(total of measured); [(b)] total of measured = (measured C) + (measured H) + (measured N) + (measured S).

Elemental analysis showed that the polymers contained <2wt% impurities (Table 2.2), which could be caused by leftover Pd catalyst or unreacted terminal functional groups (i.e., −Sn(*n*-C_4H_9)$_3$, −Sn(CH_3)$_3$, or −Br). For example, assuming that one chain

of **P1** could contain two remnant groups (at each end) as any combination of −$Sn(C_4H_9)_3$ and −Br, the sum of their weight fractions can be calculated to be from 1.2% (in case of two −Br groups) to 4.3% (in case of two −$Sn(C_4H_9)_3$ groups). Since the other polymers have lower M_n, the estimates for those would be even higher. Note that −$Sn(C_4H_9)_3$ could be unstable towards hydrolysis, and its decomposition can bring the possible range of values to 0–1.2% (in case of two −$Sn(C_4H_9)_3$ groups). This is also supported by the fact that traces of −Br were detected only in **P1**, **P2** and **P3**. Nevertheless, when corrected for impurity, the results were in good agreement with the expected elemental composition giving <0.5% deviation.

Compared to DPP and NDI, whose polymers tend to show high M_n, the TBZ unit has only one position for solubilizing alkyl group incorporation, which could have decreased its solubility and resulted in the observed moderate M_ns. In addition, large π-conjugation of DTTE could further affect the solubility, making PTBZ-DTTE polymers have lower M_n than those of similar PTBZ-DFE, PTBZ-DTzE and PTBZ-DTE.[48]

2.3.2. Thermal properties

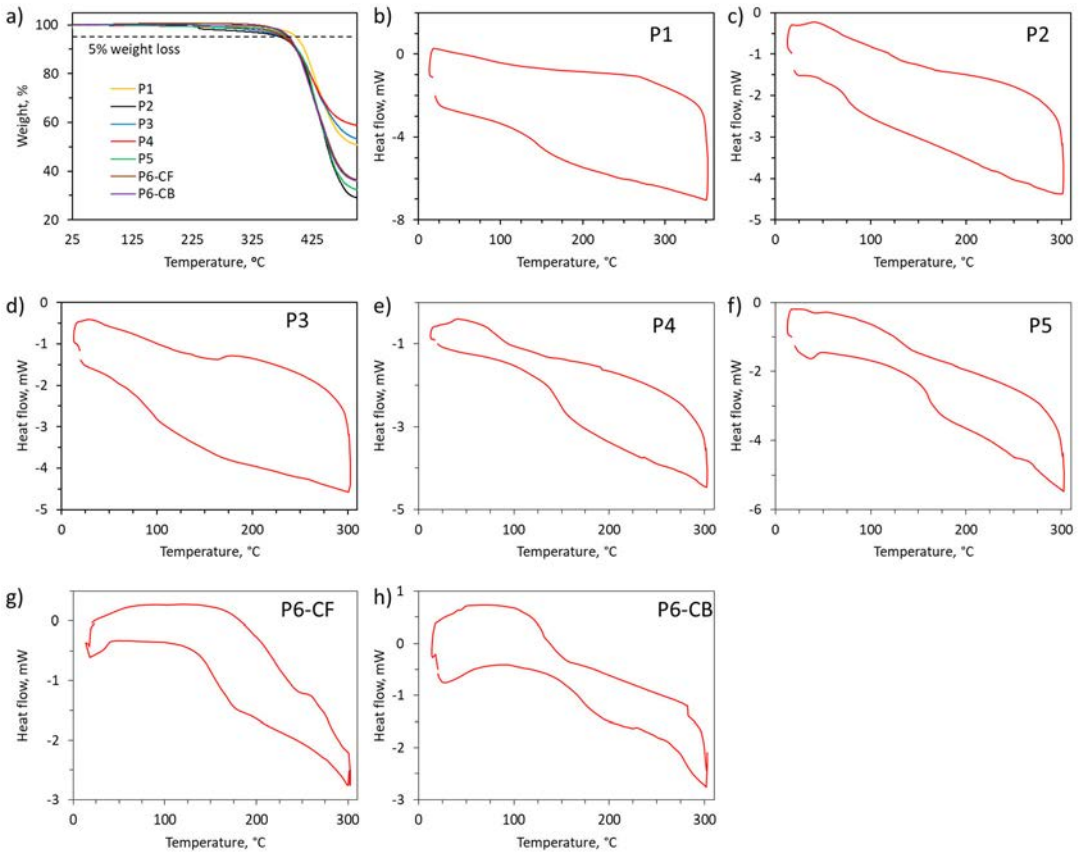


Figure 2.1. Thermal characterization results. (a) TGA curves of **P1–P6**. Second cycle DSC curves of (b) **P1**, (c) **P2**, (d) **P3**, (e) **P4**, (f) **P5**, (g) **P6-CF** and (h) **P6-CB**.

According to TGA measurements, the polymers were highly stable to heat (under N_2 flow) with T_d in the range of 375–400 °C (Figure 2.1a). Polymers also exhibited "step-down" changes in heating cycles of the DSC curves, indicating the glass transition of the amorphous phases (Figure 2.1b–h and Table 2.1). These changes happened near 75 °C for **P2** and **P3**, and at around 150 °C for other polymers. **P4**, **P5**, and **P6-CB** exhibited small exothermic peaks at 236, 264, and 233 °C, respectively. Assuming that

these are associated with crystallization of the polymer chains, these three polymers could be classified as semicrystalline.

2.3.3. Optical and electrochemical properties

The UV–vis–NIR spectra of the polymers consisted of two distinct absorption bands at 400–600 and 600–1200 nm (Figure 2.2). The absorption spectra of **P1** and **P3** were similar with bands near 500 and 860 nm, while those of **P4** and **P5** were also similar and had slightly red-shifted bands at ~510 and ~900 nm. This could be associated with the resemblances of the polymer backbone conformations in these pairs due to alkyl group placements.[7] For example, **P1** and **P3** had a similar extent of alkylation and had their alkyl side groups facing into the same space with regards to the polymer structure, which could cause very similar twist in the polymer backbone. On the other hand, due to the lack of an alky group on the thiophene flanking unit, **P4** could be expected to have more planar backbone than **P5**. As expected, **P4** exhibited a slightly bathochromically shifted absorption peak than **P5**. Furthermore, due to extensively alkylated backbone and high steric hindrance between flanking thiophene units and DTTE, **P2** had significantly hypsochromically shifted absorption band among the polymers. The most red-shifted absorption spectra (peak at 1065 nm) were obtained for

P6 (both **P6-CF** and **P6-CB** had identical spectra), whose backbone was expected to be highly planar.

Absorption band edges of **P1**, **P2**, and **P3** shifted to higher wavelengths when these polymers were cast into thin films. This could be attributed to the increase in the interchain overlap of the molecular orbitals in the solid phase due to the closely packed polymer chains.[7] On the other hand, **P4**, **P5**, and **P6-CF** films exhibited marginal red-shifts of the absorption bands, suggesting that these polymers were partially aggregated in their solutions. Absorption spectra of thermally annealed films of **P4**, **P5**, and **P6-CF** underwent a clear red-shift, with an additional shoulder appearing. This indicated that molecular orbital overlap increased because polymer chains packed more tightly into crystalline domains upon thermal treatment. Annealed films of **P1**, **P2**, and **P3** did not show any shifts of the absorption bands, suggesting that these polymers did not form long-range ordered crystallites of π-π stacked polymer chains. These observations were in good agreement with the DSC results, which revealed that **P4**, **P5**, and **P6** had crystallization peaks, while **P1**, **P2**, and **P3** were mostly amorphous. The $E_{g,opt}$ of the polymers were in the range of 1.00–1.44 eV (Figure 2.3b). By correlating the $E_{g,opt}$ with the backbone planarity of the polymers, they can be ordered as **P2** < **P1** ~ **P3** < **P4** ~ **P5** < **P6**.

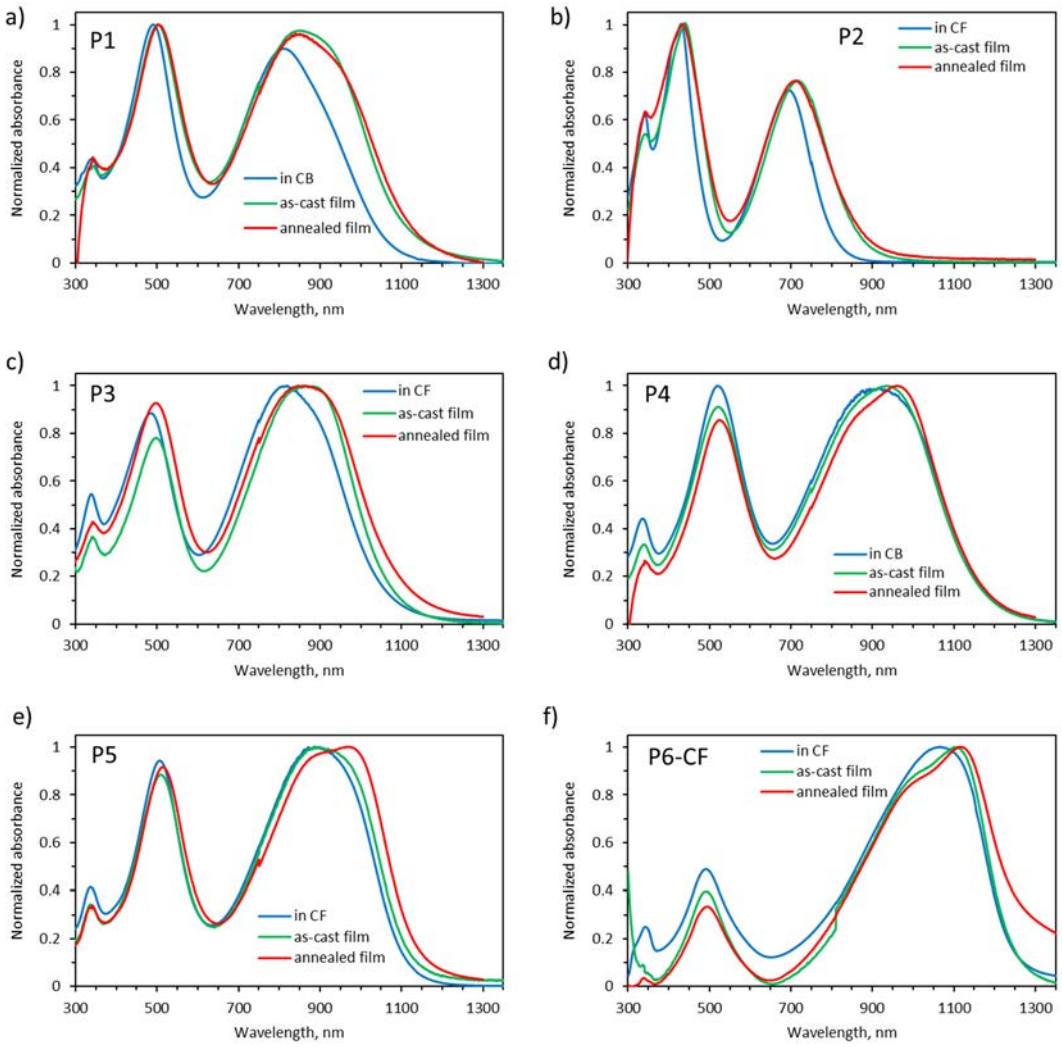


Figure 2.2. Absorption spectra of (a) **P1**, (b) **P2**, (c) **P3**, (d) **P4**, (e) **P5**, and (f) **P6** (**P6-CF**) in dilute solutions (in chloroform, CF, or chlorobenzene, CB), as-cast and annealed films.

CV curves of the polymers exhibited clear oxidation peaks, whereas the reduction peaks were not distinct (Figure 2.3), suggesting that the polymers had more p-type nature. Interestingly, the calculated E_{HOMO} of **P1** was identical to that of PTBZ-DTE (−5.00 eV), while the E_{LUMO} was shallower (−3.45 eV).[48] Taking into account the general uncertainty of the p-type semiconducting polymers' E_{LUMO} estimated from CV, the E_{HOMO} values of **P1**-**P6** were compared. Clear similarities can be observed for **P1**

and **P3** (around −5.00 eV), and for **P4** and **P5** (around −4.90 eV). This is in good agreement with the resemblances observed in the absorption spectra. The energy gaps estimated from the CV curves ($E_{g,EC}$) were in the range of 1.42–1.62 eV. It is agreed that $E_{g,EC}$ is typically 0.2–0.4 eV higher than the $E_{g,opt}$.[7] Nevertheless, the $E_{g,EC}$ and $E_{g,opt}$ values among the polymers had similar trends, which suggested that the same molecular orbitals were involved in both band gaps.

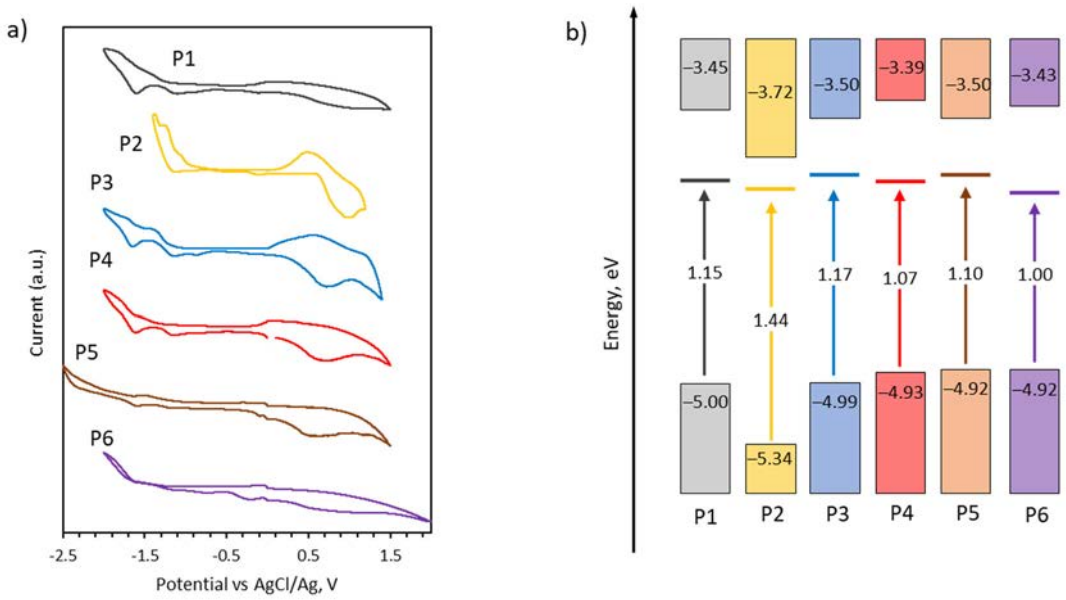


Figure 2.3. (a) CV curves of the films of **P1–P6** and (b) energy level diagram of electrochemically determined E_{HOMO} and E_{LUMO} of **P1–P6** as well as $E_{g,opt}$ extracted from UV–vis–NIR absorption spectra.

2.3.4. Theoretical calculations

DFT calculations were performed using the Gaussian 09 program with the B3LYP/6–31G(d) basis set (Figure 2.4). All alkyl groups were reduced to methyl

groups to decrease computational costs. Firstly, geometries of $(D-A)_4$ and D−A−D structures of **P1** were optimized and compared. Since there were no differences, calculations for all other polymers were conducted on D−A−D segments only, which allowed to avoid costly processes.

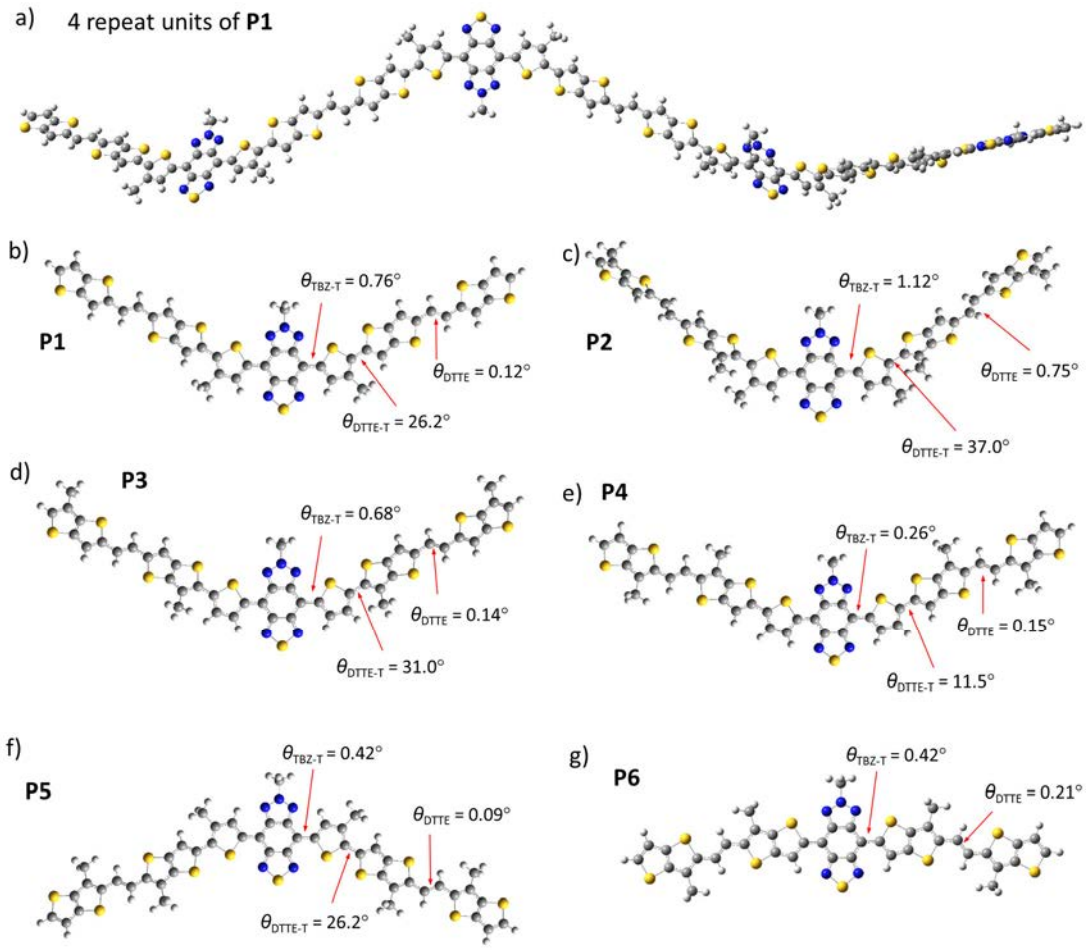


Figure 2.4. Optimized structures of the polymers calculated with DFT. (a) Optimized structure of the four repeat D−A segments of **P1**. Optimized structures of D−A−D segments of (b) **P1**, (c) **P2**, (d) **P3**, (e) **P4**, (f) **P5** and (g) **P6**. Alkyl substituents were reduced to methyl groups.

Polymers were evaluated on the basis of the dihedral angles between the TBZ and flanking thiophene units (θ_{TBZ-T}), between the DTTE and thiophene units (θ_{DTTE-T}), and

between vinylene-bridged thieno[3,2-*b*]thiophene units (θ_{DTTE}) (Figure 2.4b–g). Both θ_{DTTE} and $\theta_{TBZ–T}$ were negligible (≤1.75 and ≤1.12°, respectively) in all polymers. On the other hand, $\theta_{DTTE–T}$ fluctuated significantly depending on the presence/absence of alkyl groups at the thiophene spacer and/or at the 6,6'-positions of DTTE. Thus, $\theta_{DTTE–T}$ values were 26, 37, 31, 11 and 26° for **P1**, **P2**, **P3**, **P4** and **P5**, respectively. As expected, **P2** had the highest backbone torsion due to the steric hindrance between the two alkyl groups competing for common space. When the alkyl groups were removed from the flanking thiophene units as in **P3**, the backbone slightly planarized. Interestingly, when the alkyl groups were removed from the DTTE units (**P1** and **P5**), backbone became more planar than that of **P3**. This suggested that 3-alkylthiophene results in less steric hindrance than 6,6'-DTTE. Backbone of **P4** was even more planar due to the lack of alkyl groups on both thiophene and DTTE units. Remarkably, **P6** exhibited $\theta_{DTTE–T}$ = 1°, suggesting that its backbone was exceptionally coplanar and rigid. This can explain the low solubility of the polymer, which is likely caused by strong aggregation. Coplanarity of the backbone among the polymers can be ordered as **P2** < **P3** ≤ **P1** ~ **P5** < **P4** < **P6**.

In addition to the molecular geometries, frontier molecular orbital distributions were calculated as well (Figure 2.5). Thus, HOMOs of all polymers were delocalized over almost all of the conjugation length, whereas LUMOs were mostly confined to the

TBZ units. This supported the CV results in that the polymers were expected to exhibit p-type charge transport.

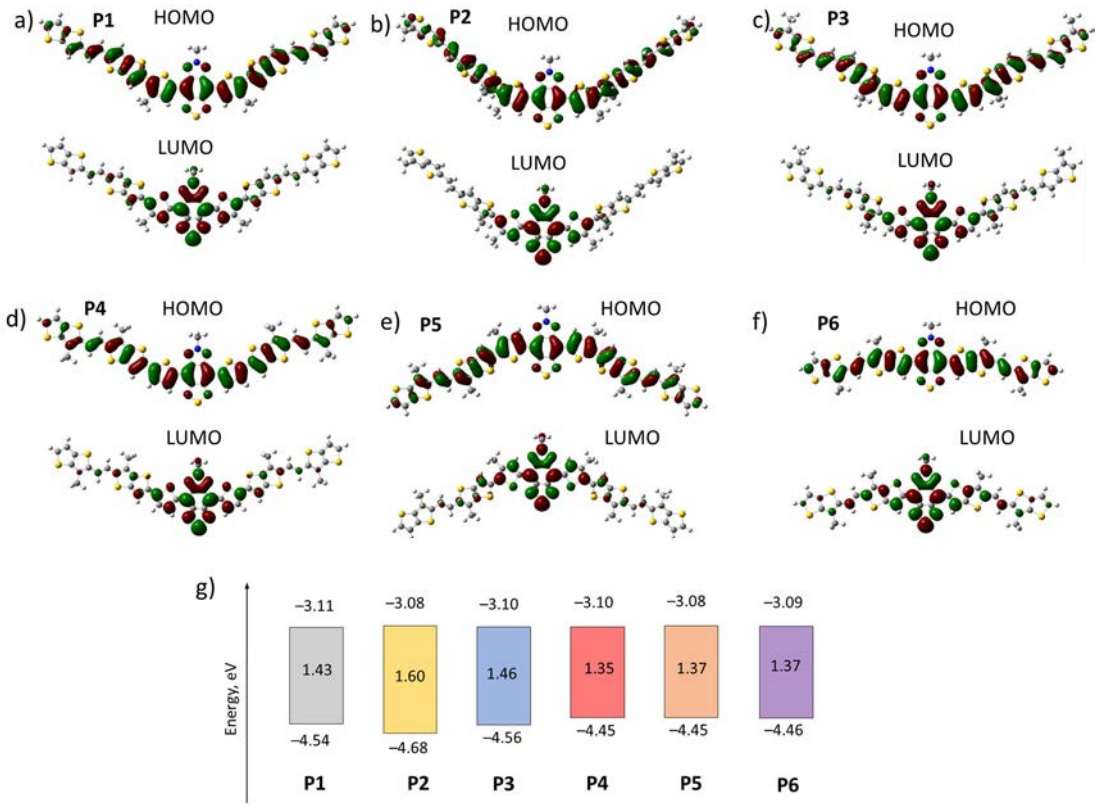


Figure 2.5. DFT-calculated HOMO and LUMO of (a) **P1**, (b) **P2**, (c) **P3**, (d) **P4**, (e) **P5** and (f) **P6**. Alkyl substituents were reduced to methyl groups. g) Representation of calculated energy levels.

2.3.5. OFET performances

Table 2.3. Summary of OFET performances of **P1**–**P6**

	Annealing T, °C	μ_h, cm^2 V^{-1} s^{-1}		I_{on}/I_{off}	V_T, V
		maximum [a]	average [b]		
P1	–	7.2×10^{-4}	$(5.2 \pm 1.6) \times 10^{-4}$	10^2–10^3	−25 to −12
	200	1.1×10^{-3}	$(9.1 \pm 1.7) \times 10^{-4}$	10^2–10^3	−20 to −10
	220	2.3×10^{-3}	$(2.0 \pm 0.2) \times 10^{-3}$	10^2–10^3	−10 to 0
	240	8.0×10^{-3}	$(6.4 \pm 1.1) \times 10^{-3}$	10–10^2	−5 to 10
	260	**8.1×10^{-3}**	**$(6.9 \pm 0.9) \times 10^{-3}$**	**10–10^2**	**−5 to 9**
	280	4.2×10^{-3}	$(2.8 \pm 1.4) \times 10^{-3}$	10–10^2	−10 to 5
P2	–	0.5×10^{-4}	$(3.0 \pm 1.8) \times 10^{-5}$	10^2–10^3	10 to 18
	150	**1.9×10^{-4}**	**$(1.5 \pm 0.4) \times 10^{-4}$**	**10^2–10^4**	**−20 to −14**
	200	1.1×10^{-4}	$(9.8 \pm 1.0) \times 10^{-5}$	10^3–10^4	−15 to −5
P3	–	1.9×10^{-3}	$(1.5 \pm 0.2) \times 10^{-3}$	10^3–10^4	−2 to 10
	150	4.2×10^{-3}	$(3.4 \pm 0.4) \times 10^{-3}$	10^3–10^5	−2 to 10
	200	8.9×10^{-3}	$(7.3 \pm 0.8) \times 10^{-3}$	10^4–10^5	−5 to 5
	250	1.9×10^{-2}	$(1.7 \pm 0.1) \times 10^{-2}$	10^4–10^5	−5 to 0
	300	4.8×10^{-2}	$(4.2 \pm 0.4) \times 10^{-2}$	10^2–10^3	−5 to 2
	325	**9.0×10^{-2}**	**$(7.7 \pm 0.6) \times 10^{-2}$**	**10^4–10^6**	**−6 to −3**
	350	8.1×10^{-2}	$(7.0 \pm 0.1) \times 10^{-2}$	10^3–10^5	−10 to 0
P4	–	0.04	0.03 ± 0.01	10^3–10^4	−4 to 8
	150	0.09	0.08 ± 0.01	10^4–10^5	−4 to 10
	200	0.14	0.12 ± 0.01	10^4–10^6	0 to 10
	250	**0.15**	**0.10 ± 0.02**	**10^2–10^3**	**5 to 15**
	300	0.14	0.12 ± 0.01	10^3–10^4	0 to 15
P5	–	0.08	0.07 ± 0.01	10^3–10^4	1 to 10
	150	0.12	0.10 ± 0.01	10^3–10^4	4 to 12
	200	0.14	0.12 ± 0.01	10^3–10^4	8 to 15
	250	**0.18**	**0.13 ± 0.02**	**10^3–10^4**	**12 to 14**
	300	0.11	0.09 ± 0.02	10^3–10^4	15 to 18
P6-CF	–	0.09	0.08 ± 0.01	10^2–10^3	22 to 31
	150	0.14	0.14 ± 0.01	10–10^2	25 to 41
	200	**0.21**	**0.18 ± 0.01**	**10^2–10^3**	**23 to 30**
	250	0.18	0.17 ± 0.01	10^2–10^3	26 to 30
	300	0.18	0.15 ± 0.01	10–10^2	20 to 32
P6-CB	–	0.24	0.20 ± 0.03	10^3–10^4	8 to 19
	150	0.29	0.25 ± 0.03	10^3–10^4	7 to 15
	200	0.43	0.34 ± 0.05	10^3–10^4	9 to 18
	250	**0.44**	**0.36 ± 0.05**	**10^3–10^4**	**9 to 21**
	300	0.41	0.29 ± 0.06	10–10^2	28 to 58

[a] The highest mobilities; [b] The average mobilities and their standard deviation ranges calculated from *I*–*V* performances of 10–20 devices, which were prepared on 2–3 separate films.

Thin films of **P2**, **P3**, **P5**, and **P6-CF** were spin-coated from chloroform solutions for OFET fabrication. Due to the lower solubilities in chloroform, chlorobenzene solutions were used for deposition of **P1** and **P6-CB**. On the other hand, despite its

sufficient solubility in chlorobenzene, films of **P4** were spin-coated from an *o*-DCB solution due to poor uniformity of films deposited from chlorobenzene solutions. Similarly, **P2** exhibited good solubility in *n*-hexane but a chloroform solution was used for spin-coating. As expected, all polymers showed unipolar p-type charge transport when the devices were tested under ambient air in the dark (Figure 2.6 and Table 2.3). **P6** with the highly coplanar backbone showed the highest μ_h among the polymers. Thus, the optimized μ_h values were 0.44 and 0.21 $cm^2\ V^{-1}\ s^{-1}$ for a **P6-CB** film annealed at 250 °C and a **P6-CF** film annealed at 200 °C, respectively. **P4** and **P5** showed μ_h of 0.15 and 0.18 $cm^2\ V^{-1}\ s^{-1}$, respectively. Since the $(-I_D)^{1/2}$–V_G curves for the **P5** devices were "kinked"[115] and the μ_h values were calculated from the high-slope region. The non-ideal *I*–*V* behavior could not be eliminated by altering the device fabrication conditions, such as deposition spin rate, solvent, and annealing temperature. Although, the reason for such a "kinked" transfer curve is debatable, some of the suggestions include charge trapping by the semiconductor,[116] charge trapping by the dielectric,[117] and gate-dependent contact resistance.[118] **P1** films exhibited the μ_h of $8.1 \times 10^{-3}\ cm^2\ V^{-1}\ s^{-1}$, which was over ten times lower than that of PTBZ-DTE copolymer with a similar *n*-hexadecyl alkyl group on the thiophene flanking units.[48] We attribute this to a lower alkylation extent in **P1**, which could negatively affect its film-forming properties. By changing the alkyl substituent from the thiophene flanking

unit to the DTTE unit, **P3** exhibited an improved μ_h of 0.09 $cm^2\ V^{-1}\ s^{-1}$. Interestingly, the optimized μ_h among the **P3** devices was obtained from films annealed at extremely high temperature of 325 °C. **P2** devices annealed at 150 °C gave a limited μ_h of $1.9 \times 10^{-4}\ cm^2\ V^{-1}\ s^{-1}$.

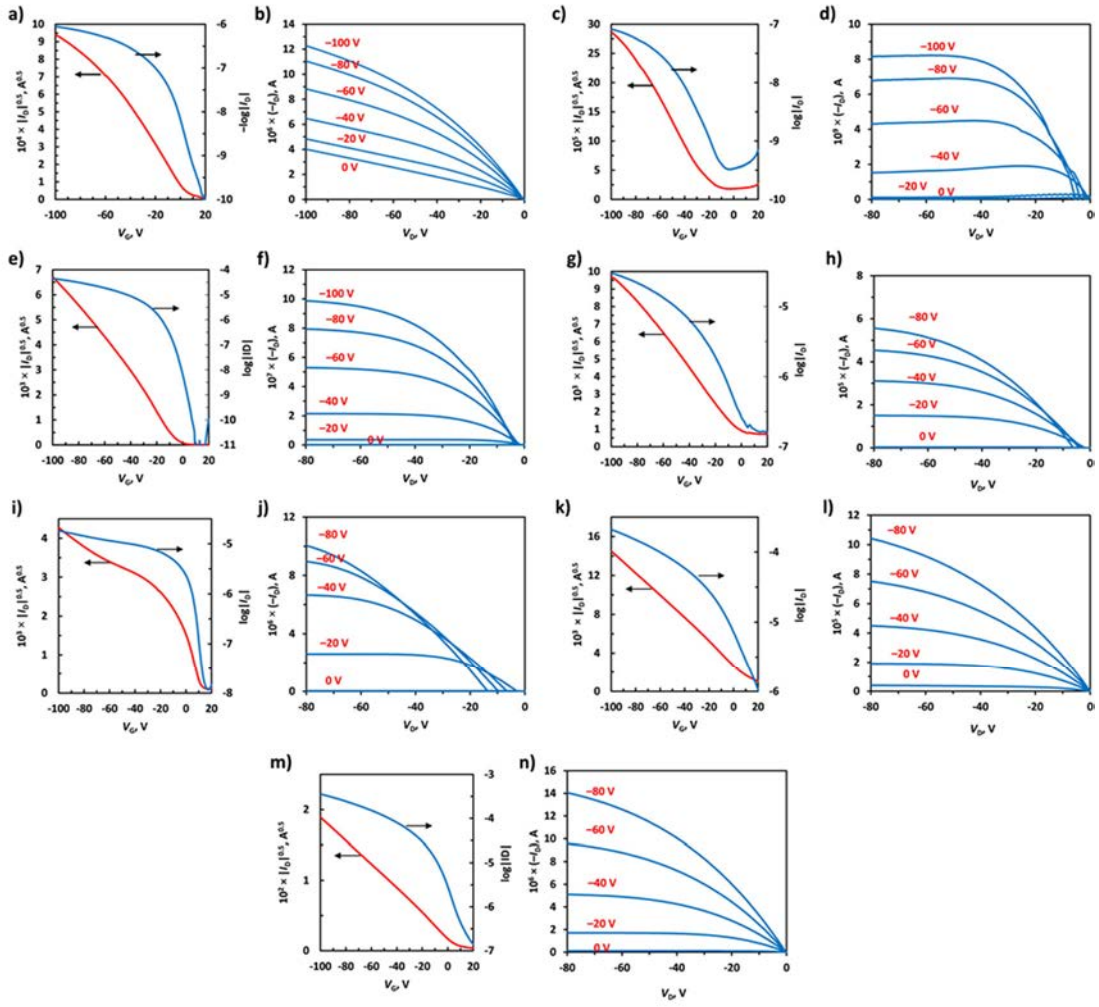


Figure 2.6. *I–V* behavior of polymers films in BGTC OFET devices: (a) transfer and (b) output curves of **P1** annealed at 260 °C; (c) transfer and (d) output curves of **P2** annealed at 150 °C; (e) transfer and (f) output curves of **P3** annealed at 325 °C; (g) transfer and (h) output curves of **P4** annealed at 250 °C; (i) transfer and (j) output curves of **P5** annealed at 250 °C; (k) transfer and (l) output curves of **P6-CF** annealed at 200 °C; (m) transfer and (n) output curves of **P6-CB** annealed at 250 °C. Measurements were done under ambient conditions in the dark. Transfer curves were recorded at V_D of −60 V.

Again, the polymers can be ordered according to their μ_h values as **P2** < **P1** ~ **P3** < **P4** ~ **P5** < **P6**. The trend of **P2** < **P1** < **P5** can be compared to PDPP-DTTE polymers with similar alkyl side group placements on the DTTE units: 3,3'-DTTE < DTTE < 6,6'-DTTE.[82,91,107] This relationship can be further extended to **P3** < **P4**. On the other hand, the effect of thiophene spacers was not studied in PDPP-DTTE polymers. However, PDPP-DTE polymers without a thiophene spacer showed lower μ_h compared to the one with spacers.[119] This was contrary to the trend observed in **P4** < **P6**.

2.3.6. Film morphology and microstructures

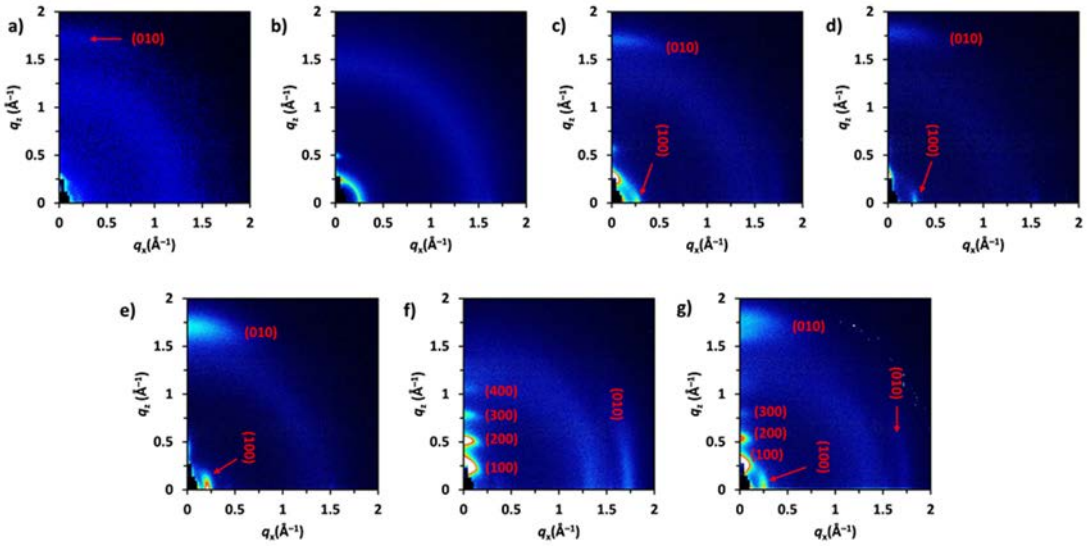


Figure 2.7. GIWAXS images of (a) **P1** film annealed at 260 °C, (b) **P2** film annealed at 150 °C, (c) **P3** film annealed at 325 °C, (d) **P4** film annealed at 250 °C, (e) **P5** film annealed at 250 °C, (f) **P6-CF** film annealed at 200 °C and (g) **P6-CB** film annealed at 250 °C. Films were deposited onto n^+-Si/SiO_2/OTMS substrates and annealed for 10 min under Ar atmosphere.

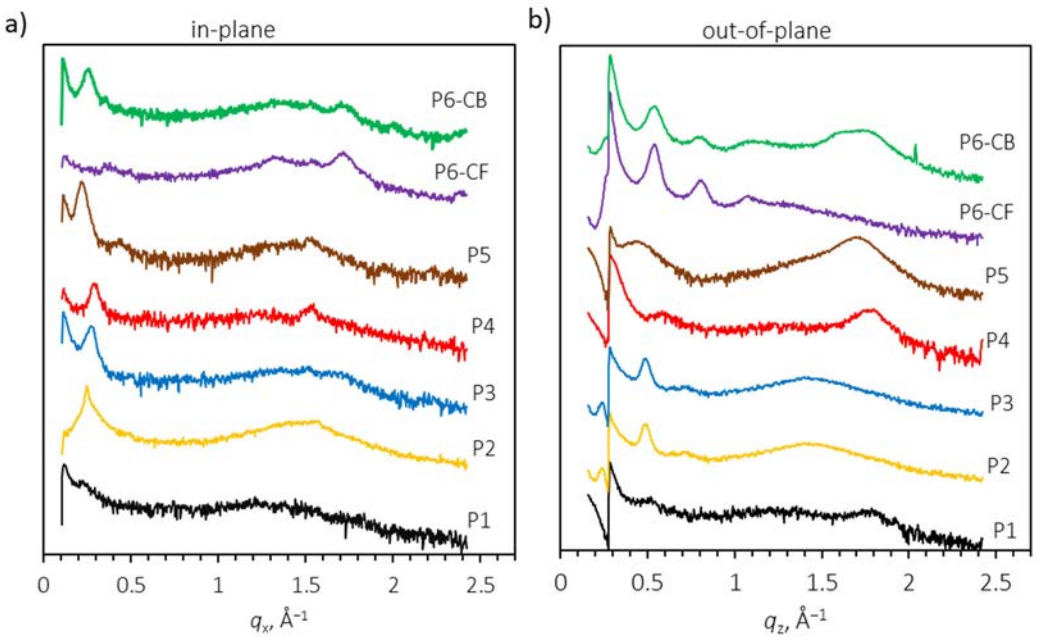


Figure 2.8. (a) Out-of-plane and (b) in-plane 1D GIWAXS peak intensities of **P1** film annealed at 260 °C, **P2** film annealed at 150 °C, **P3** film annealed at 325 °C, **P4** film annealed at 250 °C, **P5** film annealed at 250 °C, **P6-CF** film annealed at 200 °C and **P6-CB** film annealed at 250 °C. Films were deposited onto n^+-Si/SiO_2/OTMS substrates and annealed for 10 min under Ar atmosphere.

In order to investigate the crystallinity and polymer packing orientation, GIWAXS measurements of the polymer thin films were performed. According to a weak (010) reflection in the out-of-plane direction (q_z axis), **P1** acquired face-on molecular packing orientation with a short $d_{\pi\text{-}\pi}$ of 3.53 Å (Figure 2.7). Surprisingly, there were no clear peaks in the in-plane direction, indicating that it lacked a lamellar stacking. Although the $d_{\pi\text{-}\pi}$ was shorter in **P1** than that of similar PTBZ-DTE polymer (3.57 Å),[48] inferior μ_h of **P1** can be related to the absence of well-ordered crystallinity. **P2** was completely amorphous, as there were no observable reflections in any of the directions. **P3, P4** and **P5** films also exhibited face-on packing orientation. From the

(010) reflections in the out-of-plane direction, the $d_{\pi\text{-}\pi}$ values were 3.69, 3.56 and 3.69 Å, respectively. Tighter π-π stacking in **P4** could be caused by higher backbone planarity. From the (100) peaks in the in-plane direction, the d_L of **P3**, **P4** and **P5** were 22.52, 21.74 and 28.3 Å, respectively. Higher d_L of **P5** can be caused by the longer alkyl groups at the thiophene spacer (*n*-hexadecyl), as compared to the ones at the DTTE units in **P3** and **P4** (*n*-undecyl). Better OFET performance of **P3** compared to that of **P1** obviously originated from the higher crystallinity of **P3**, as observed from more intense (010) and (100) reflections. On the other hand, the peak intensities in **P3** and **P4** films were similar but **P4** showed higher μ_h, which was caused by the tighter π-π stacking (Figure 2.8). Despite the larger $d_{\pi\text{-}\pi}$, **P5** showed better μ_h than **P4** due to much higher crystallinity (judged from reflection intensities). Nevertheless, these unfavorable face-on molecular packing motifs in **P1**, **P3**, **P4** and **P5** could be the reason why these polymers showed inferior μ_h than the PTBZ-DTE polymer with *n*-hexadecyl alkyl group.[48] In addition, similar PDPP-DTTE polymers also showed much higher μ_h because these polymers acquired edge-on molecular packing orientation.[82,91,107]

P6-CF film showed up to four orders of (*h*00) peaks in the out-of-plane direction, as well as a sharp (010) peak in the in-plane direction, indicating that polymer chains packed in a long-range ordered edge-on orientation. On the other hand, **P6-CB** additionally exhibited a single (100) peak in the in-plane direction and an intense (010)

peak in the out-of-plane direction. This indicated that **P6-CB** had the mixture of edge-on and face-on packed crystallites. This bimodal packing mode is deemed to be beneficial for macro-scale charge transport due to the creation of alternative charge "hopping" pathways.[54,55] The $d_{\pi\text{-}\pi}$ and d_L values of both **P6-CF** and **P6-CB** were 3.66 Å and ~22 Å, respectively. Thus, improved μ_h of **P6-CB** can be attributed to the presence of bimodal packing motif, which in turn could be caused by the differences in the molecular weights (M_n of **P6-CB** > M_n of **P6-CF**).[88]

PDPP-DTE polymer without a thiophene spacer had a face-on packing orientation with $d_{\pi\text{-}\pi}$ = 3.89 Å, which was changed to edge-on packing with $d_{\pi\text{-}\pi}$ = 3.84 Å when the spacer was incorporated.[119] This was almost exactly the opposite to what was observed for **P6** (without thiophene spacer) and **P4** (with thiophene spacer). As a result, exclusion of the thiophene spacers in PTBZ-DTTE polymers led to superior OFET performances. In general, uniform distribution of alkyl side groups in **P4**, **P5** and **P6** gave films with higher crystallinity.[64,65] On the other hand, **P1** and **P3** had less crystalline films, due to the concentrated alkyl groups near or/at the TBZ unit only. In addition, excess alkylated **P2** gave completely amorphous films.

The AFM topographical images showed that **P1** failed to form a uniform film (Figure 2.9). The surface of the film was irregular with ~200-nm-wide fiber-like aggregates stretching up to several micrometers. The root-mean-squared (RMS) surface

roughnesses of **P1**, **P2**, **P3**, **P4**, **P5**, **P6-CF** and **P6-CB** films were 2.83, 0.27, 0.76, 0.49, 0.99, 1.45, and 1.18 nm, respectively. Excluding **P1**, the RMS surface roughness values were consistent with the intensities of the GIWAXS peaks. For example, **P2** film, earlier concluded as amorphous, was smooth due to the absence of crystalline aggregations. Surface roughness order of **P4** < **P3** < **P5** is also reflected by the intensities of (100) peaks in the GIWAXS images.

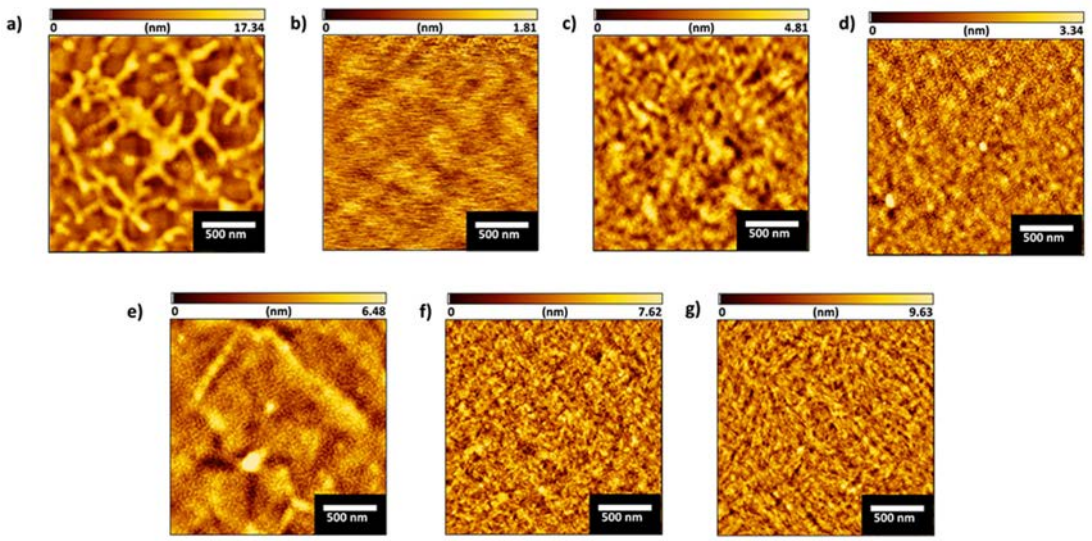


Figure 2.9. AFM images of (a) **P1** film annealed at 260 °C, (b) **P2** film annealed at 150 °C, (c) **P3** film annealed at 325 °C, (d) **P4** film annealed at 250 °C, (e) **P5** film annealed at 250 °C, (f) **P6-CF** film annealed at 200 °C and (g) **P6-CB** film annealed at 250 °C. Films were deposited onto n^+-Si/SiO_2/OTMS substrates and annealed for 10 min under Ar atmosphere.

In addition to the absence of long-range ordering in **P1**, its non-uniform surface morphology could also cause its low μ_h. Surface of **P5** was also not as uniform as those of the other polymers, which could be the reason for the deviation of its *I-V* behavior in OFETs.[116] The extent of crystallinity and surface morphology of the polymers can be

placed in the order of **P2** < **P1** < **P3** < **P4** < **P5** < **P6**. This is in good agreement with the observed OFET performances.

2.4. Conclusion

Backbone planarity in PTBZ-DTTE polymers was tuned by using side alkyl group engineering. Due to the rigidity of the DTTE unit and coplanarity of the TBZ−thiophene linkage, the only dihedral angle affected by the alkyl side group placement was that of the DTTE−thiophene segment. Thus, the overall dihedral angles estimated from DFT calculations were 26, 37, 31, 11, and 26° for **P1**, **P2**, **P3**, **P4** and **P5**, respectively, which had thiophene spacers in the π-conjugated backbone. Both experimental and theoretical optoelectronic properties showed good correlation with these results. On the other hand, film-forming properties of the polymers showed dependence on both the alkylation extent and its uniform distribution across the polymer backbone. As a result, highly alkylated **P2** with a strong backbone twist formed amorphous films which exhibited limited μ_h (0.0002 $cm^2\ V^{-1}\ s^{-1}$). By removing one of the alkyl side groups, the backbone planarity was improved in **P1** and **P3**, but clustering of alkyl groups near/at the TBZ unit gave less crystalline films with the moderate μ_h of 0.008 and 0.09 $cm^2\ V^{-1}\ s^{-1}$, respectively. The lower μ_h of **P1** was attributed to non-uniform film morphology. On the other hand, **P4** and **P5** with uniformly distributed

alkyl groups gave highly crystalline films that exhibited the improved μ_h of 0.14 and 0.18 $cm^2 V^{-1} s^{-1}$, respectively. Unlike other reported TBZ-based polymers, **P1**–**P5** films acquired unfavorable face-on molecular packing orientation, which could be the reason for the limited OFET performances of PTBZ-DTTE polymers in this work. Since the DTTE−thiophene segment was causing the main backbone torsion, a sixth polymer (**P6-CF** and **P6-CB)** without a thiophene spacer was also synthesized. Despite the limited molecular weights, both fractions gave highly crystalline films which contained advantageous edge-on packing motifs. As a result, **P6-CF** and **P6-CB** devices exhibited the improved μ_h of 0.21 and 0.44 $cm^2 V^{-1} s^{-1}$, respectively.

Chapter 3

Random Copolymers with Methoxy Conformational Locks

This chapter was adapted from the published article: Otep, S.; Lin, Y.-C.; Matsumoto, H.; Mori, T.; Wei, K.-H.; Michinobu, T. Diketopyrrolopyrrole–thiophene–methoxythiophene based random copolymers for organic field effect transistor applications. *Org. Electron.* **2020**, *87*, 105986. https://doi.org/10.1016/j.orgel.2020.105986. Copyright (2021) Elsevier.

3.1. Introduction

One of the first D-A polymers reported with μ comparable to that of amorphous Si (~1 $cm^2\ V^{-1}\ s^{-1}$) was PDPP-TT in 2010, which showed μ_h of 0.94 $cm^2\ V^{-1}\ s^{-1}$.[24] Since then, DPP was applied in many D-A designs for high-mobility OFET applications and turned into a versatile building block.[3,120,121] Structure-property relationship studies utilizing heteroatom substitution and side-group optimization have shown the importance of backbone planarity to achieve high performance polymers.[9–11,56,82,107,122] Prominent examples of DPP-based polymers that exhibited ultra-high μ_h approaching and exceeding 10 $cm^2\ V^{-1}\ s^{-1}$ are PDPP-TT,[9] PDPP-DTE,[10] PDPP-DSE,[10,11] and PDPP-DTTE.[82] Specifically, PDPP-DTE, PDPP-DSE and PDPP-DTTE formed

tightly packed semicrystalline films thanks to highly planar polymer backbones, which were achieved by incorporation of vinylene bridges into the design.[10,11,82]

Another method to enhance the planarity of the polymer backbone is the incorporation of noncovalent "conformational locks" into neighboring units. "Locks" can be formed by hydrogen bonding[51] and pairs of electron-deficient and electron-rich heteroatoms, such as halogen···sulfur (F···S, Cl···S and Br···S), oxygen···sulfur (O···S), and nitrogen···sulfur (N···S).[75,123,124] When a locking is realized, the actual distances between the atoms are significantly smaller than the sums of their van der Waals radii (by ~0.4–0.6 Å), due to strong attractive interactions. This causes the dihedral angle between adjacent aromatic rings to decrease. Typically, in addition to the planarizing effect, *N*-substitution and F-substitution are used as a means to enhance n-type charge transport by lowing the E_{LUMO}. In contrast, alkoxy substitution (i.e., incorporation of S···O locks) increases the E_{HOMO}, facilitating the p-type charge transport. For example, 3-alkoxy-2,2'-bithiophenes and 3,3'-dialkoxy-2,2'-bithiophenes exhibited narrow E_g due to the electron donating nature of alkoxy groups.[78,124–129] In the scope of this approach, 3,3'-dialkoxy-2,2'-bithiophenes were copolymerized with phthalimide,[125] thiophene and benzo[1,2-*b*:4,5-*b*']dithiophene[126] to improve the μ_h of the copolymers. However, in most cases, incorporation of 3-alkoxythiophenes resulted in higher $d_{\pi\text{-}\pi}$ values and formation of face-on dominant molecular packings.[78,125–127] As a result, the

method could be deemed less favorable to design semiconducting polymers for OFET applications.

Nevertheless, the recent development of random copolymerization approach has shown that a trade-off between the advantageous and negative effects of introducing a new unit can be controlled.[130–132] Generally, this is done by managing the monomer feed ratios to synthesize copolymers with $(A-B)_x(A-C)_{1-x}$ structures. For example, in the series of $(DPP-TT)_x(DPP-DSE)_{1-x}$ random copolymers, the μ_h was gradually improved from 3 to 9 $cm^2 V^{-1} s^{-1}$ with the increasing DSE content, while the solubility and most of the other physical properties exhibited extrema at around $x = 0.3–0.7$.[87] In other words, those properties did not change linearly when transitioning from pure PDPP-TT to pure PDPP-DSE. Thus, by controlling the extent of incorporation of the third monomer component, a synergy between the favorable properties of all building units can be achieved. This work focuses on a ternary copolymer approach by incorporating the 3,3'-dimethoxy-2,2'-bithiophene unit into PDPP-4T polymer in a controlled manner.

3.2. Materials and Methods

3.2.1. Materials

All chemicals were purchased from Tokyo Chemical Industry (TCI), Kanto Chemical,

Co., Inc., and Sigma Aldrich, and were used as received. Monomers **M1**,[133] **M2**[134] and **M3**[135] were synthesized according to reported procedures and reacted in controlled ratios to give copolymers **P7**, **P8**, **P9**, **P10** and **P11** (Scheme 3.1).

3.2.2. General measurements

Instrumentation and measurement procedures of ^{1}H NMR, ^{13}C NMR, GPC, TGA, DSC and UV–vis absorption spectroscopy were identical to those provided in Chapter 2. New and modified experimental methods are described below.

CV measurements were performed on a BAS electrochemical analyzer model 100 at room temperature in a three-electrode cell at the sweep rate of 50 mV s^{-1}. The working, reference, and auxiliary electrodes were a glassy carbon electrode, Ag/AgCl, and Pt wire, respectively. Solution of tetrabutylammonium hexafluorophosphate ($(C_4H_9)_4NPF_6$) in acetonitrile was used as electrolyte. Polymer films were drop cast onto the working electrode from 5 mg mL^{-1} solutions in chloroform. Redox potential of Fc/Fc^{+} was used for calibration and E_{HOMO} was calculated as $E_{HOMO} = -(\varphi_{ox} + 4.80)$ {eV}.

3.2.3. OFET fabrication and characterization

The preparation of n^{+}-Si/SiO_2/OTMS substrates and OFET testing equipment was similar to the ones provided in Chapter 2. Polymer thin films were deposited inside an Ar-filled glovebox onto the n^{+}-Si/SiO_2/OTMS substrates by spin-coating (1000–3000

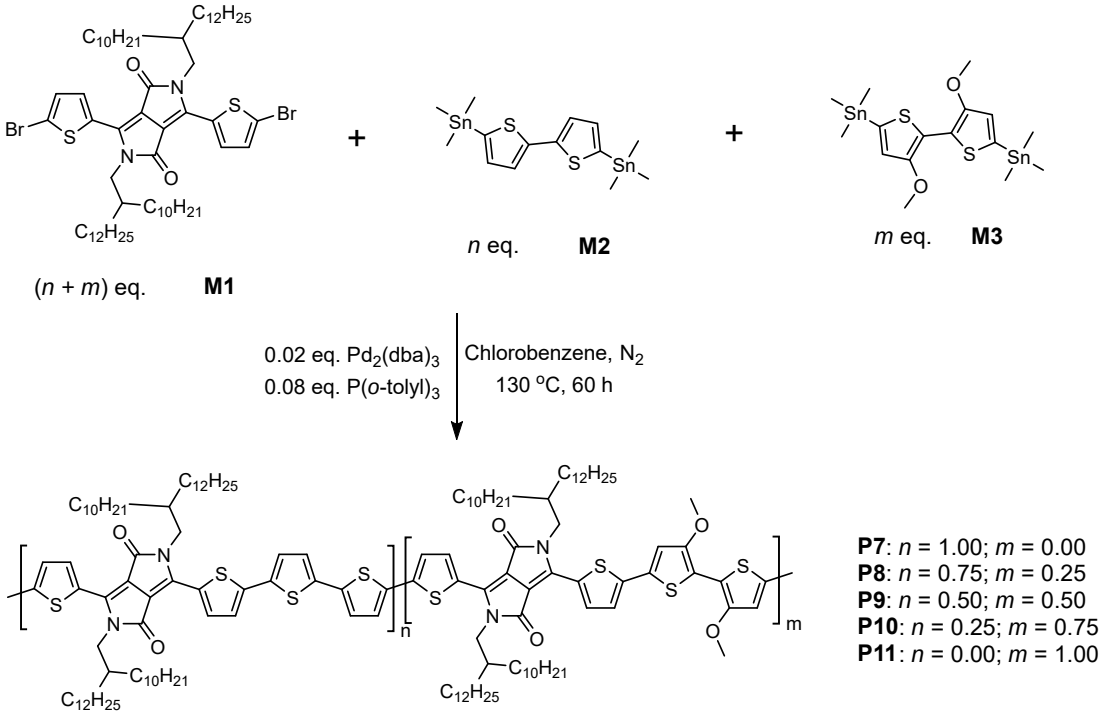
RPM) from 5 mg mL^{-1} chloroform solutions, followed by thermal annealing at temperatures of 150–300 °C for 15 min. After the polymer thin film deposition, a ~40-nm-thick gold layer was vacuum deposited as the source and drain contacts using a shadow mask (W/L = 100/1000 μm). For the incorporation of ionic additive tetramethyl ammonium iodide (Me_4NI), it was dissolved in dimethyl sulfoxide (1 mg mL^{-1}) and added to the above solution of polymers to meet the molar ratio of 1:30 between Me_4NI and DPP units. These solutions were kept heated (50–60 °C) to avoid precipitation of the salt. Transfer and output curves were measured under vacuum. The μ_h were calculated from the transfer curves in the saturated regime.

3.2.4. Film morphology and microstructures

For GIWAXS and tapping-mode AFM measurements, samples were prepared by the methods similar to the OFET devices under optimized conditions. The instrumentation and measurement procedures were identical to the ones described in Chapter 2.

3.3. Results and Discussion

3.3.1. Polymer synthesis



Scheme 3.1. Structures of the monomers **M1–M3** and synthetic route to copolymers **P7–P11**.

Table 3.1. Summary of properties of **P7**–**P11**.

	M_n, kg mol^{-1}	PDI	T_d, °C [a]	$E_{g,opt}$, eV [b]	E_{HOMO}, eV [c]	E_{LUMO}, eV [d]
P7	36.1	2.79	406	1.40	−5.30	−3.90
P8	64.4	4.81	412	1.39	−5.32	−3.93
P9	1.95	2.20	386	1.28	−5.17	−3.89
P10	2.59	1.83	384	1.25	−5.06	−3.81
P11	3.00	2.23	382	1.24	−4.86	−3.62

[a] Temperature corresponding to 5% weight loss. [b] Determined from the onset of absorption band in thin film. [c] Determined from the onset of the oxidation peak in cyclic voltammetry curve. [d] Calculated as $E_{LUMO} = E_{HOMO} + E_{g,opt}$.

The extent of incorporation of **M3** into the polymer backbone was evidenced from ^{1}H-NMR spectroscopy results (Figure 3.1). **P7**, which had no **M3**, exhibited peaks at 9.01 ppm and 6.20–7.40 ppm (thiophene rings), which are characteristic of PDPP-4T polymers. A peak at 4.05 ppm corresponding to −OCH_3 appeared in **P8** and its intensity

relative to that of the peak at 9.01 ppm gradually increased from **P8** to **P11**. This indicated that the **M3**/**M2** ratio raised in the given order and the integration ratios were close to the theoretically estimated values.

According to GPC results, **P7** and **P8** showed higher M_n of 36.1 and 64.4 kg mol^{-1}, respectively, while **P9**, **P10** and **P11** gave limited M_n in the range of 2–3 kg mol^{-1} (Table 3.1). Lower M_n of **P9**, **P10** and **P11** can partially be caused by their strong adhesion to the polystyrene gels used in GPC due to the high polymer backbone planarity induced by the 3,3'-dimethoxy-2,2'-bithiophene units.[124] This would increase the retention time of the polymers and result in apparent low M_n.

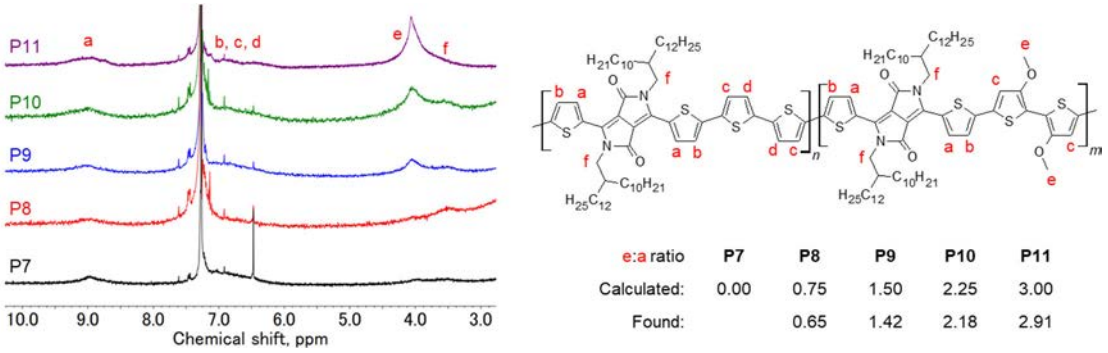


Figure 3.1. Amplified ^{1}H-NMR spectra of **P7–P11** (measured in $CDCl_3$) with assigned peaks shown on the chemical structure (right).

3.3.2. Thermal properties

Copolymers exhibited high thermal stability under N_2 flow with T_d in the range of 380–410 °C (Table 3.1 and Figure 3.2a). **P8** was more stable than **P7**, which could

be attributed to the higher M_n of the former. On the other hand, T_d gradually decreased from **P9** to **P10**. Since the polymers have similar M_n, this indicates the lower thermal stability of the methoxy groups. As expected from polymers with the low alkylation extent (only DPP units), DSC curves did not contain step-down changes attributable to glass transition in the heating/cooling range of 20–300 °C (Figure 3.2b–f). Interestingly, **P8** exhibited clear melting and crystallization peaks at 296 and 273 °C, respectively. Earlier, PDPP-4T was shown to have crystallization/melting transitions at temperatures close to or above 300 °C,[55,122] which was in good agreement with our results.

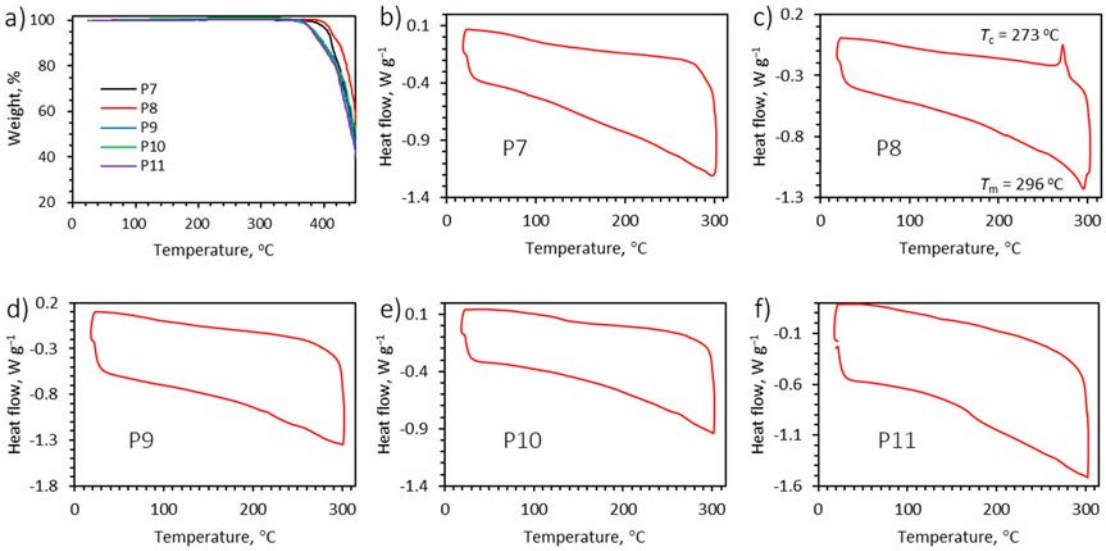


Figure 3.2. (a) TGA curves of **P7–P11** and DSC curves of (b) **P7**, (c) **P8**, (d) **P9**, (e) **P10** and (f) **P11**.

3.3.3. Optical and electrochemical properties

In UV–vis–NIR spectra, the absorption band peaks of dilute chloroform solutions

of **P7**, **P8**, **P9**, **P10** and **P11** were observed at 785, 785, 818, 868 and 873 nm, respectively (Figure 3.3a). With the increasing content of 3,3'-dimethoxy-2,2'-bithiophene units in **P8**–**P11**, the absorption gradually red-shifted. This was attributed to the stronger electron-donating nature of the methoxy groups, which facilitated charge transfer from the 3,3'-dimethoxy-2,2'-bithiophene donor to DPP acceptor.[124,136] However, with the 25mol% content of **M3** in **P8**, its absorption was nearly identical to that of **P7**. Statistically, the DPP−**M3**−DPP segments in **P8** were surrounded by DPP−**M2**−DPP segments, which could have negated the higher electron-donating effect of 3,3'-dimethoxy-2,2'-bithiophene. On the other hand, DPP−**M3**−DPP–**M3**–DPP segments (and even longer ones) were statistically possible in **P9-P11**, which efficiently lowered the E_g.

The main peaks and their lower-wavelength shoulders in the spectra of **P7**, **P8**, **P10** and **P11** were assigned to 0–0 and 0−1 transitions, respectively.[78] The presence of the shoulder hinted at the formation of polymer aggregates in the solutions. The relative intensities of the 0−0 and 0−1 peaks can reveal the structures of the aggregates: more intense 0–0 peaks arise from stronger intrachain interaction (J-aggregates), while more intense 0–1 peaks are caused by stronger interchain interactions (H-aggregates).[137,138] As-cast films of the polymers exhibited similar absorption band edges to the ones measured in solutions. Notably, the 0–1 transition peaks were more intense in films,

suggesting that the polymers packed closer in the films and tighter H-aggregates formed (Figure 3.3b). H-aggregation was significantly stronger in **P10** and **P11**, which can be confirmed from much more intense 0–1 peaks. The absorption band maxima were apparently blue-shifted. The high degree of H-aggregates in **P10** and **P11** was related to the improved backbone coplanarity compared to those of **P7** and **P8**.[53]

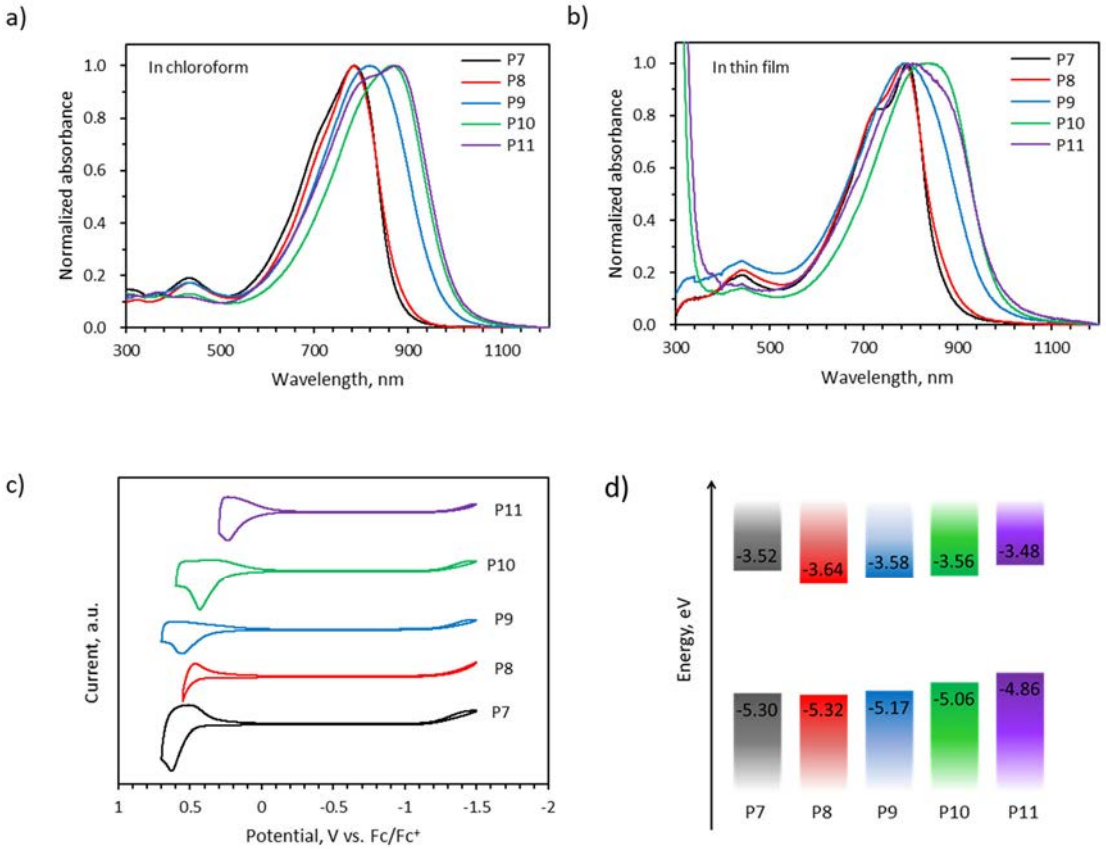


Figure 3.3. Optical and electrochemical properties of **P7–P11**. UV–vis–NIR absorption spectra of copolymers (a) in chloroform solutions and (b) in thin films. (c) CV curves. (d) Depiction of energy levels.

CV was measured in an Ar-bubbled CH_3CN with 0.1 M $(C_4H_9)_4NPF_6$ as the electrolyte. CV curves of all polymers displayed clear oxidation peaks, while the

positions of reduction peaks could not be determined with certainty. Thus, E_{LUMO} values were determined as $E_{LUMO} = E_{HOMO} + E_{g,opt}$. These results implied that all polymers exhibited p-type semiconductor properties. This was in agreement with expectations: PDPP-4T is known as a p-type semiconductor, and the incorporation of 3,3'-dimethoxy-2,2'-bithiophene should further improve its p-type nature of **P8**–**P11**. E_{HOMO} and E_{LUMO} of **P7** and **P8** differed only marginally, and could be rounded as −5.3 and −3.9 eV, respectively (Table 3.1 and Figure 3.3d). These results agreed with the previously reported E_{HOMO} and E_{LUMO} for PDPP-4T.[56] With the increasing extent of 3,3'-dimethoxy-2,2'-bithiophene, the E_{HOMO} values gradually raised, reaching the shallowest value of −4.86 eV for **P11**. Similar behavior was observed in other polymers that had 3-alkoxythiophene units in the backbone, which attributed to its electron-donating effect.[124,136] Since the shallowing of the E_{HOMO} values were more prominent than the narrowing of the $E_{g,opt}$, the E_{LUMO} values also underwent upwards shifts.

3.3.4. OFET performances

OFET devices were tested under vacuum (~10^{-5} mbar) and the copolymers exhibited potent p-type charge transport. Measurements of n-type charge transport resulted in transfer curves with large V_T and low I_{on}/I_{off}. Therefore, the structure-property relationship of the polymers was evaluated based on hole transport properties

only (Figure 3.4 and Table 3.2). The OFET devices of **P7** and **P8** prepared from films annealed at 300 °C exhibited average μ_h of 0.31 and 0.27 $cm^2\ V^{-1}\ s^{-1}$, respectively. PDPP-4T devices were reported to give μ_h <1 $cm^2\ V^{-1}\ s^{-1}$ in similar OFET configuration tested under N_2 atmosphere.[56] Optimized μ_h of the **P9**, **P10** and **P11** devices were 0.02, 0.03 and 0.07 $cm^2\ V^{-1}\ s^{-1}$, respectively (Table 3.2). Such a significantly low μ_h could be attributed to their low M_n. In a comprehensive study, short polymer chains (i.e., low M_n) were shown to form non-interconnected domains, which strongly decreased the μ_h due to large inter-domain boundaries.[88,89] Nevertheless, when compared separately, the μ_h increases in the order of **P9**, **P10** and **P11** with the increasing content of 3,3'-dimethoxy-2,2'-bithiophene in the polymer backbone.

Table 3.2. Summary of optimized OFET performances of **P7–P11**.

	Annealing T, °C [a]	μ, cm^2 V^{-1} s^{-1} [b]	V_{th}, V [b]	I_{on}/I_{off}
P7	–	0.141 ± 0.017	12.2 ± 5.5	10^3–10^5
	150	0.276 ± 0.057	12.8 ± 9.6	10^3–10^5
	200	0.233 ± 0.031	7.3 ± 6.6	10^3–10^5
	250	0.303 ± 0.029	9.9 ± 7.1	10^3–10^4
	300	0.308 ± 0.038	12.1 ± 7.0	10^2–10^4
P8	–	0.120 ± 0.010	5.1 ± 6.8	10^2–10^4
	150	0.216 ± 0.017	5.0 ± 4.3	10^3–10^5
	200	0.239 ± 0.024	6.0 ± 4.8	10^2–10^4
	250	0.256 ± 0.018	7.4 ± 5.8	10^2–10^4
	300	0.274 ± 0.058	0.3 ± 4.1	10^2–10^4
P9	–	0.003 ± 0.000	15.5 ± 2.7	10^2–10^4
	150	0.010 ± 0.001	10.3 ± 2.0	10^3–10^5
	200	0.013 ± 0.002	9.4 ± 2.6	10^3–10^5
	250	0.014 ± 0.002	13.0 ± 3.6	10^4–10^6
	300	0.018 ± 0.002	13.7 ± 3.0	10^3–10^5
P10	–	0.011 ± 0.001	3.6 ± 1.8	10^3–10^5
	150	0.020 ± 0.002	9.5 ± 3.6	10^2–10^4
	200	0.025 ± 0.002	10.3 ± 2.6	10^2–10^4
	250	0.026 ± 0.003	12.2 ± 2.5	10^2–10^4
	300	0.029 ± 0.002	6.1 ± 1.8	10^4–10^6
P11	–	0.020 ± 0.002	2.5 ± 2.8	10^3–10^5
	150	0.045 ± 0.004	3.3 ± 1.8	10^4–10^6
	200	0.051 ± 0.005	3.7 ± 1.3	10^3–10^5
	250	0.068 ± 0.004	7.7 ± 3.9	10^3–10^5
	300	0.066 ± 0.006	4.3 ± 3.2	10^4–10^6

[a] Annealed for 15 min under Ar. [b] Average of at least 20 devices prepared on two separate films. Error range shows the average deviation.

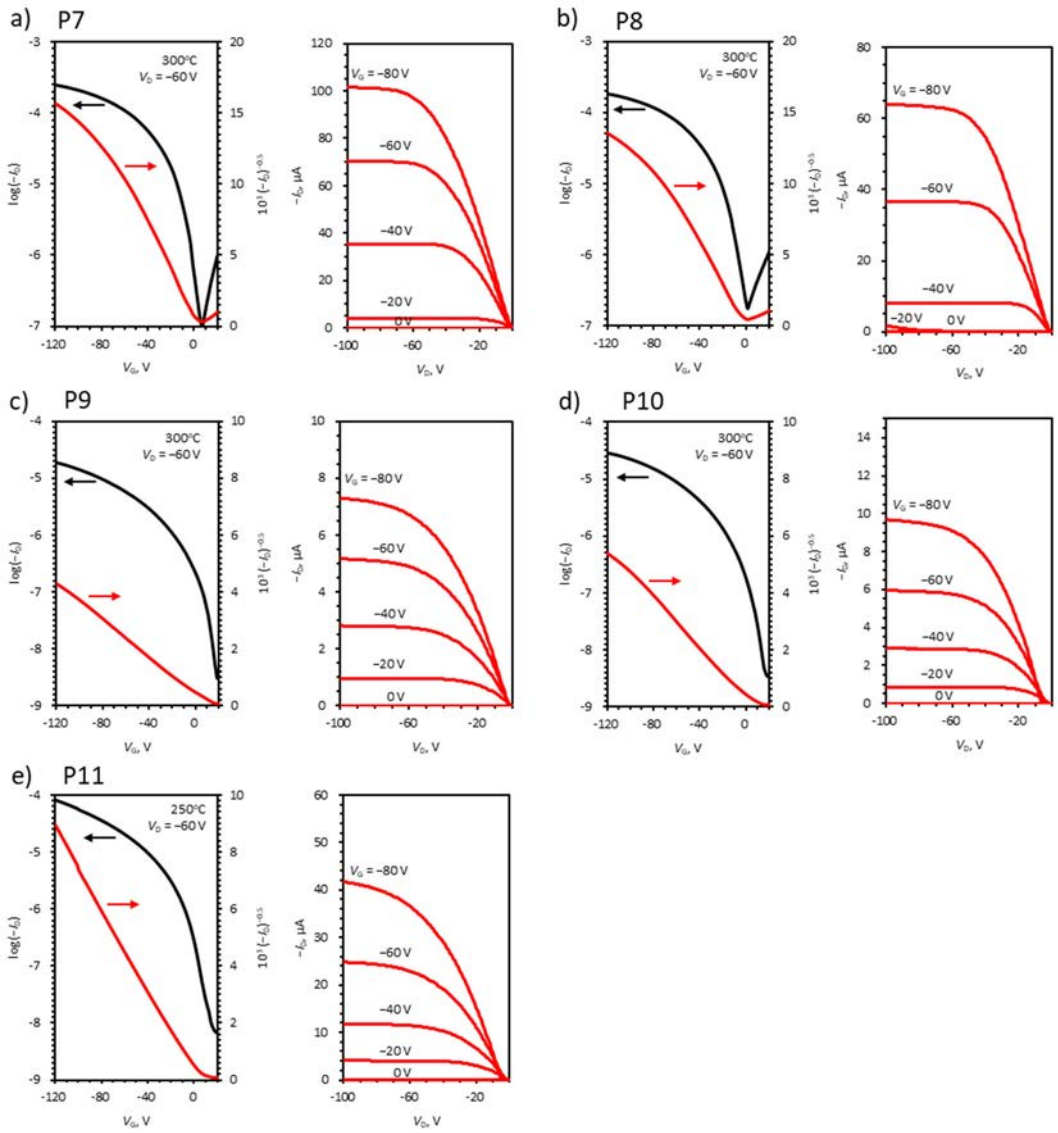


Figure 3.4. Selected transfer (left) and output (right) curves of (a) **P7**, (b) **P8**, (c) **P9**, (d) **P10** and (e) **P11**. All measurements were performed under vacuum.

3.3.5. Film morphology and microstructures

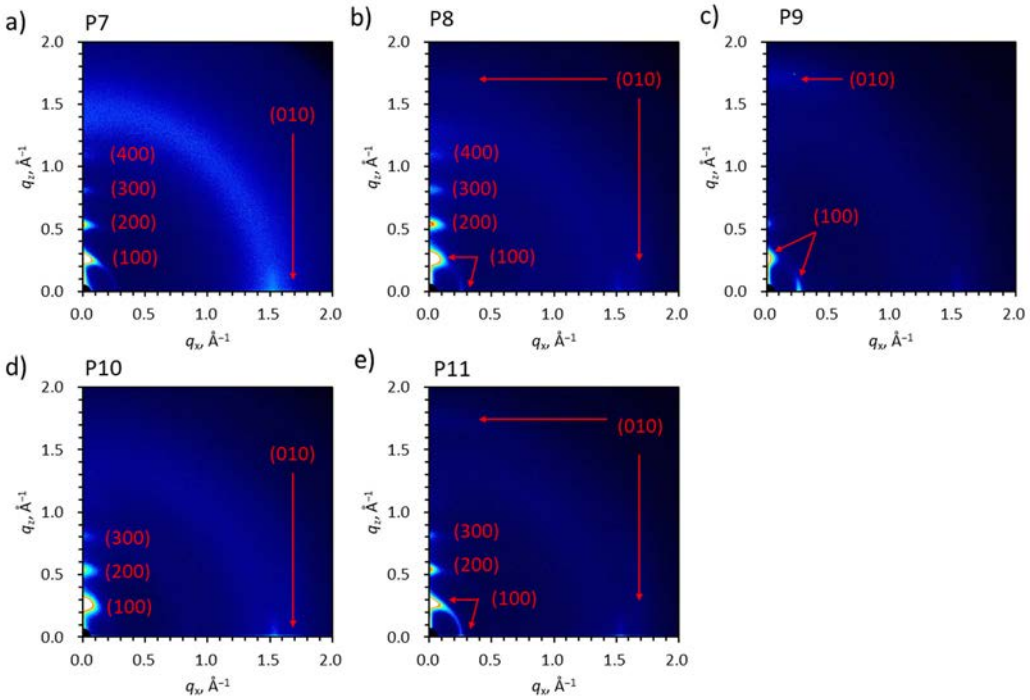


Figure 3.5. GIWAXS patterns of (a) **P7**, (b) **P8**, (c) **P9**, (d) **P10** and (e) **P11**. Films were prepared identically to the optimized ones for transistor measurements (see above).

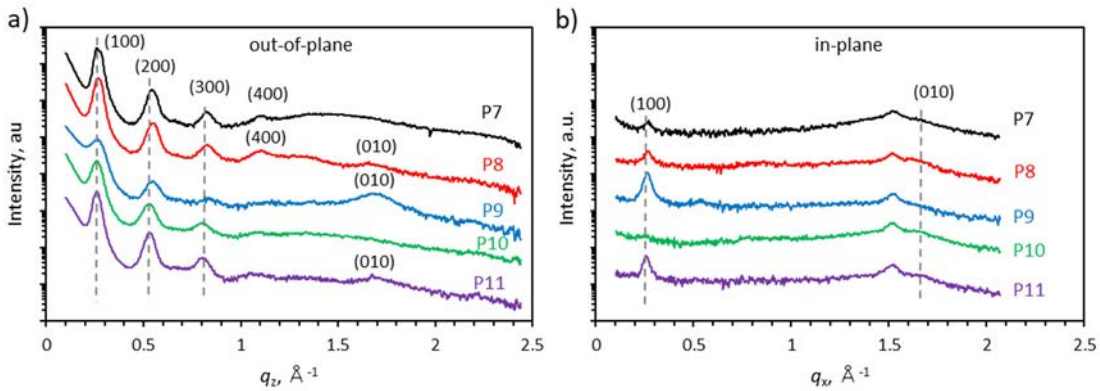


Figure 3.6. Out-of-plane and in-plane 1D-profiles of GIWAXS measurements of **P7–P11**.

GIWAXS was used to gain insight into the molecular packing orientations of the polymer films. Samples were prepared under conditions similar to those of the optimized OFETs. All polymers exhibited (*h*00) reflections in out-of-plane direction

(q_z) up to three and four orders (Figure 3.5 and Figure 3.6). This indicated that long-range face-on lamellar stackings were present in all films. The (100) peaks were located at ~0.26 Å corresponding to the d_L = ~24 Å (Table 3.3). The d_L depends on the length of the alkyl side groups and their interdigitation. All polymers had identical 2-octyldodecyl substituents at DPP and the length of the methoxy group with respect to the length of 2-octyldodecyl was negligible. Therefore, all polymers exhibited identical d_L. Thus, these results agreed with the previously reported d_L = 23.5 Å for DPP-based polymers, which also had 2-octyldodecyl substituents.[122] Crystalline coherence length was estimated from the (100) peaks using the Scherrer equation, which relates the sharpness of the peaks to the size of the crystallites.[139] Thus, crystallite sizes were 132.2, 134.4, 101.9, 115.9 and 146.8 Å for **P7**, **P8**, **P9**, **P10** and **P11**, respectively (Table 3.3). **P7**, **P8**, **P10** and **P11** films exhibited broadenings at 1.60–1.75 $Å^{-1}$ in the in-plane direction (q_x) corresponding to the (010) reflection. These were attributed to π-π stacking of the polymer chains in the edge-on orientation, but the broadness of the peaks indicated that the order in the packing was short-ranged. Nevertheless, the maxima of the reflections gave $d_{\pi\text{-}\pi}$ values of 3.77, 3.77, 3.74 and 3.75 Å for **P7**, **P8**, **P10** and **P11** films, respectively (Table 3.3). In addition to these, **P8**, **P9** and **P11** film showed (010) peaks in the out-of-plane direction as well, which indicated that a face-on molecular packing was present in these films. 1D profiles of **P9** films had strong in-plane (100),

(200) peaks and out-of-plane (010) peak ($d_{\pi\text{-}\pi}$ = 3.75 Å). As a result, from the presence of (h00) and (010) peaks either in q_z or q_x axes, it was concluded that **P7** and **P10** formed edge-on dominant packings; **P9** formed a face-on dominant packing; and **P8** and **P11** formed edge-on dominant bimodal packings.

Table 3.3. Summary of the analysis of GIWAXS results of **P7–P11**.

	out of plane (100)				out-of-plane (010)		in-plane (010)	
	q_z, Å^{-1}	d_L, Å	FWHM, Å^{-1}	L_c, Å	q_z, Å^{-1}	$d_{\pi\text{-}\pi}$, Å	q_x, Å^{-1}	$d_{\pi\text{-}\pi}$, Å
P7	0.259	24.27	0.04276	132.2	–	–	1.666	3.77
P8	0.265	23.70	0.04207	134.4	1.660	3.78	1.666	3.77
P9	0.265	23.70	0.05547	101.9	1.675	3.75	–	–
P10	0.259	24.27	0.04878	115.9	–	–	1.680	3.74
P11	0.262	23.98	0.03853	146.8	1.672	3.75	1.675	3.75

Scherrer equation: $L_c = 2\pi K/\text{FWHM}$, where K = 0.9, where L_c – size of the crystallites, FWHM – full width at half maximum.

Polymer packing orientation is determined by interplay of many factors. The important ones are the interactions between polymer chains, substrate surface and solvent molecules.[67] UV–vis–NIR spectroscopy showed that **P7**, **P8**, **P10** and **P11** tend to form pre-aggregates in chloroform. This leads to the formation of polymer chain clusters with π-π stacked backbones sandwiched between layers of hydrophobic alkyl side groups. During film deposition from solutions, these hydrophobic layers tend to attach to the SAM-modified surface of the substrate due to attractive hydrophobic interactions. This leads to the formation of edge-on dominant packing motifs in such polymer films. On the other hand, aggregation-free polymer chains of **P9** were more stabilized by attaching both alkyl side groups to the SAM surface. As a result, **P9**

formed a face-on dominant molecular packing motif. The pre-aggregation of the polymers, in the first place, could be facilitated by high planarity of the polymer backbone (in **P10** and **P11**) and/or high M_n (in **P7** and **P8**). **P9** had lower backbone coplanarity than **P10** and **P11** due to fewer 3,3'-methoxy-2,2'-bithiophene units. In combination with the low M_n, this led to the absence of pre-aggregates. Alternatively, the deviation of **P9** from the general trend could be caused by a so-called "segmental randomness" due to 1:1 ratio between 2,2'-bithiophene and 3,3'-methoxy-2,2'-bithiophene units.[87] In some series of random copolymers of the $(A{-}B)_x(A{-}C)_{1-x}$ structure, the ones with $x = 0.5$ were reported to exhibit out-of-trend low crystallinity [87,140] and high $d_{\pi\text{-}\pi}$.[141] It is worth noting that these effects did not necessarily result in poor device performances.

Edge-on packing is considered beneficial for the charge transport in OFETs due to the parallel stacking of π-π overlaps with respect to the substrate surface.[48,142] Bimodal packing further facilitates the macro-scale charge transport because additional pathways are created by face-on packed crystallites. In addition, polymer films with larger crystalline domains also give improved μ due to decreased inter-domain boundaries. Thus, the μ_h trend in **P9**, **P10** and **P11** was in good agreement with the above expectations: crystallite sizes increase in this order; and the molecular packing orientation changes from face-on in **P9** to edge-on in **P10** and further to bimodal in **P11**.

The μ_h trend is further supported by the elevation of E_{HOMO}, which improved the hole injection from the source electrode. On the other hand, despite the bimodal packing and similar crystallite size, **P8** showed a slightly lower μ_h than **P7**. Since $d_{\pi\text{-}\pi}$ and E_{HOMO} were also similar in both polymers, the bottleneck of the charge transport could be attributed to the wide molecular weight distribution of **P8** (PDI = 4.8). This could affect the film morphology, which was confirmed from AFM measurements (see below). However, It is worth noting that the effect of molecular weight distribution (i.e., PDI) on molecular packing, film morphology and charge transport properties of D-A semiconducting polymers is not fully understood.[88,89,143,144]

In AFM topographical images of the **P7** film, fiber-like textures were observed (Figure 3.7). Previous works have shown than fiber-like structures in conjugated polymer films are formed from π-π stacked polymer chains, which facilitates the charge transport.[88,89] The average width of the fibers were ~68 nm. The estimated length of a **P8** polymer chain containing 32 repeat units (~2 nm each) is ~64 nm. This confirmed that polymer chains were fully stretched across the fiber width.[89] Hence, the π-π stacking direction was along the fiber length, giving good charge transport in this direction. On the other hand, the surface of **P8** film had larger structures scattered in a more isolated manner. From the M_n, the estimated length of **P8** polymer chain was 112 nm (56 repeat units), which was within the range of the average sizes of the surface

structures in the AFM image. As a result, this morphology could cause the observed lower μ_h of **P8** devices compared to the one expected from the trend in GIWAXS results only: GIWAXS results predicted that **P8** should exhibit higher μ_h than **P7**. **P9** film exhibited much smaller surface structures randomly dispersed all over the surface, while **P10** and **P11** films formed larger features. This in part resembled the surface morphology of **P8** film. Since larger domain sizes facilitate the charge transport, these surface morphologies, in combination with the GIWAXS results, were in agreement with the observed μ_h trend in **P9**, **P10** and **P11**.

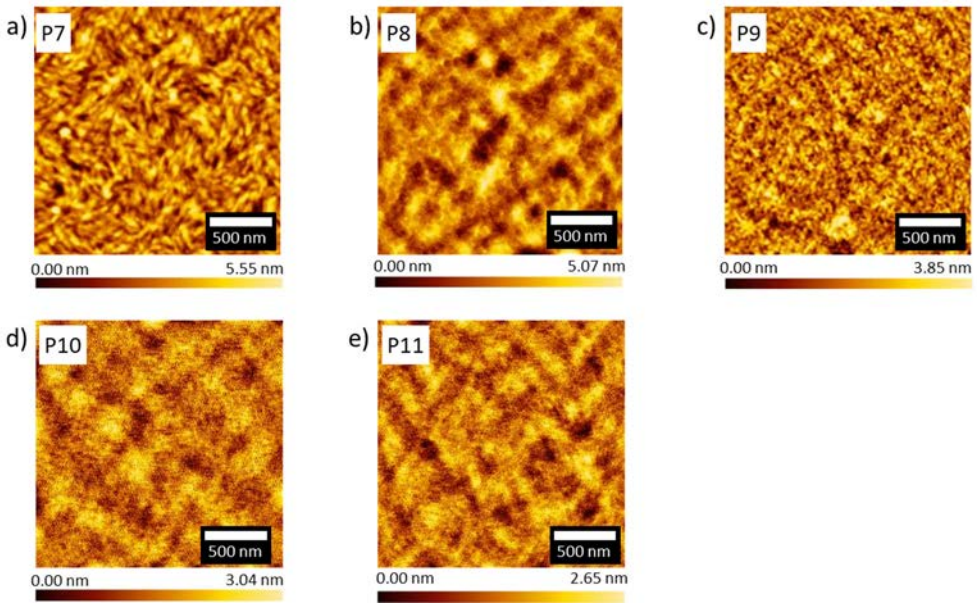


Figure 3.7. Atomic force microscopy images of (a) **P7**, (b) **P8**, (c) **P9**, (d) **P10** and (e) **P11**. Films were prepared identically to the optimized ones for transistor measurements (see above).

3.3.6. Effect of ionic additive on OFET performances

Recently, Me_4NI was reported as a potent ionic additive for DPP-based D-A semiconducting polymers.[101,145] Due to the localization of Me_4N^+ ions near the DPP unit, the rotation of alkyl side groups with respect to the polymer backbone was restricted.[101] This facilitated the formation of highly crystalline films with bimodal molecular packings. As a result, the average μ_h increased from 0.8 to 19.5 $cm^2\ V^{-1}\ s^{-1}$ upon incorporation of the additive at the molar ratio of Me_4NI/DPP = 1:30. Here we also investigated the effect of this additive on the charge transport properties of **P7**, **P8** and **P11** film. Although the optimized annealing temperatures for pure films were higher (300, 300 and 250 °C, respectively), annealing temperature for the additive-incorporated films were set to 200 °C. This was done to avoid possible thermal decomposition of the salt.[146] The μ_h of **P7** devices increased from 0.23 to 0.39 $cm^2\ V^{-1}\ s^{-1}$ upon incorporation of the additive (Me_4NI/DPP = 1:30). On the other hand, neither **P8** nor **P11** devices were not affected by the presence of Me_4NI (Figure 3.8). It is surprising that the content of 3,3'-dimethoxy-2,2'-bithiophene as low as 25mol% completely eliminated the additive's effect.

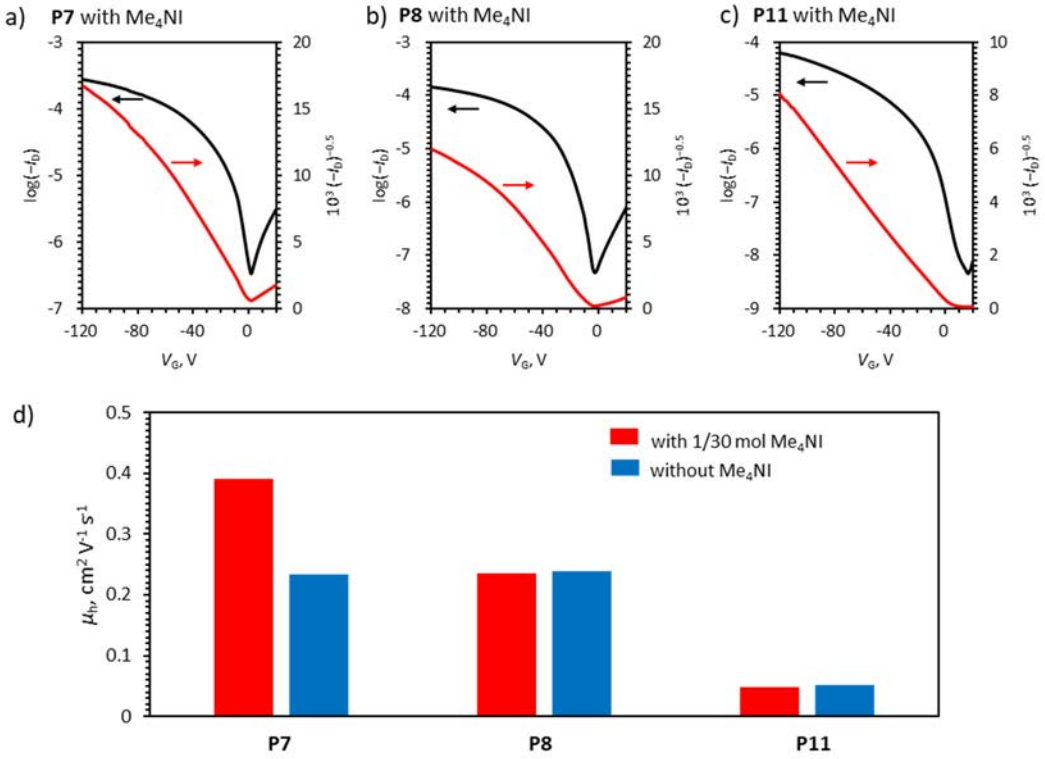


Figure 3.8. Transfer curves of OFET devices with Me_4NI ionic additive (Me_4NI/DPP = 1:30 mol) incorporated into thin films of (a) **P7**, (b) **P8** and (c) **P11**. (d) Average hole mobility measured with and without incorporation of Me_4NI ionic additive (Me_4NI/DPP = 1:30 mol) into thin films of **P7**, **P8** and **P11**. Films were annealed at 200 °C for 15 min. Values are the average of at least 20 devices prepared on two separate films.

3.4. Conclusion

By controlling the monomer ratios in the polymerization reaction, series of random copolymers based on PDPP-4T backbone with different contents of the 3,3'-dimethoxy-2,2'-bithiophene unit were synthesized. Due to the electron-donating effect of the methoxy group, $E_{g,opt}$ of the random copolymers decreased. This was accompanied by a gradual raising of E_{HOMO}, which positively affected the p-type charge

transport in the polymers. Polymers with higher 3,3'-dimethoxy-2,2'-bithiophene loading preferred the formation of edge-on dominant or bimodally packed films, which is deemed as advantageous for the charge transport in OFETs. **P8**, which contained 25mol% of the 3,3'-dimethoxy-2,2'-bithiophene unit showed a μ_h of ~0.27 $cm^2 V^{-1} s^{-1}$. This was comparable to μ_h = ~0.31 $cm^2 V^{-1} s^{-1}$ measured from **P7** (0mol%) devices. Random copolymers with higher 3,3'-dimethoxy-2,2'-bithiophene contents had limited M_n. This severely impaired their charge transport properties. Yet, μ_h increased as the 3,3'-dimethoxy-2,2'-bithiophene content increased from 50mol% in **P9** (0.02 $cm^2 V^{-1} s^{-1}$) to 75mol% in **P10** (0.03 $cm^2 V^{-1} s^{-1}$) and 100mol% in **P11** (0.07 $cm^2 V^{-1} s^{-1}$). GIWAXS and AFM revealed that these low-M_n polymers had inferior crystallinity and poor film morphology, which hindered their charge transport properties. Therefore, we theorize that high-M_n analogs of these polymers should exhibit enhanced μ_h. Finally, effects of incorporating the Me_4NI ionic additive into the polymer films on their OFET performances were evaluated. While **P7** exhibited improved μ_h, incorporation of merely 25mol% of the 3,3'-dimethoxy-2,2'-bithiophene unit into the backbone suppressed the effect of the additive.

Chapter 4

Cross-linking of Poly(arylenebutadiynylene)s and Its Effect on Charge Transport Properties

This chapter was adapted with permission from the published article: Otep, S.; Ogita, K.; Yomogita, N.; Motai, K.; Wang, Y.; Tseng, Y.-C.; Chueh, C.-C.; Hayamizu, Y.; Matsumoto, H.; Ishikawa, K.; Mori, T.; Michinobu, T. Cross-Linking of Poly(arylenebutadiynylene)s and Its Effect on Charge Carrier Mobilities in Thin-Film Transistors. *Macromolecules* **2021**, *54*, 4351–4362. https://doi.org/10.1021/acs.macromol.1c00008. Copyright (2021) American Chemical Society.

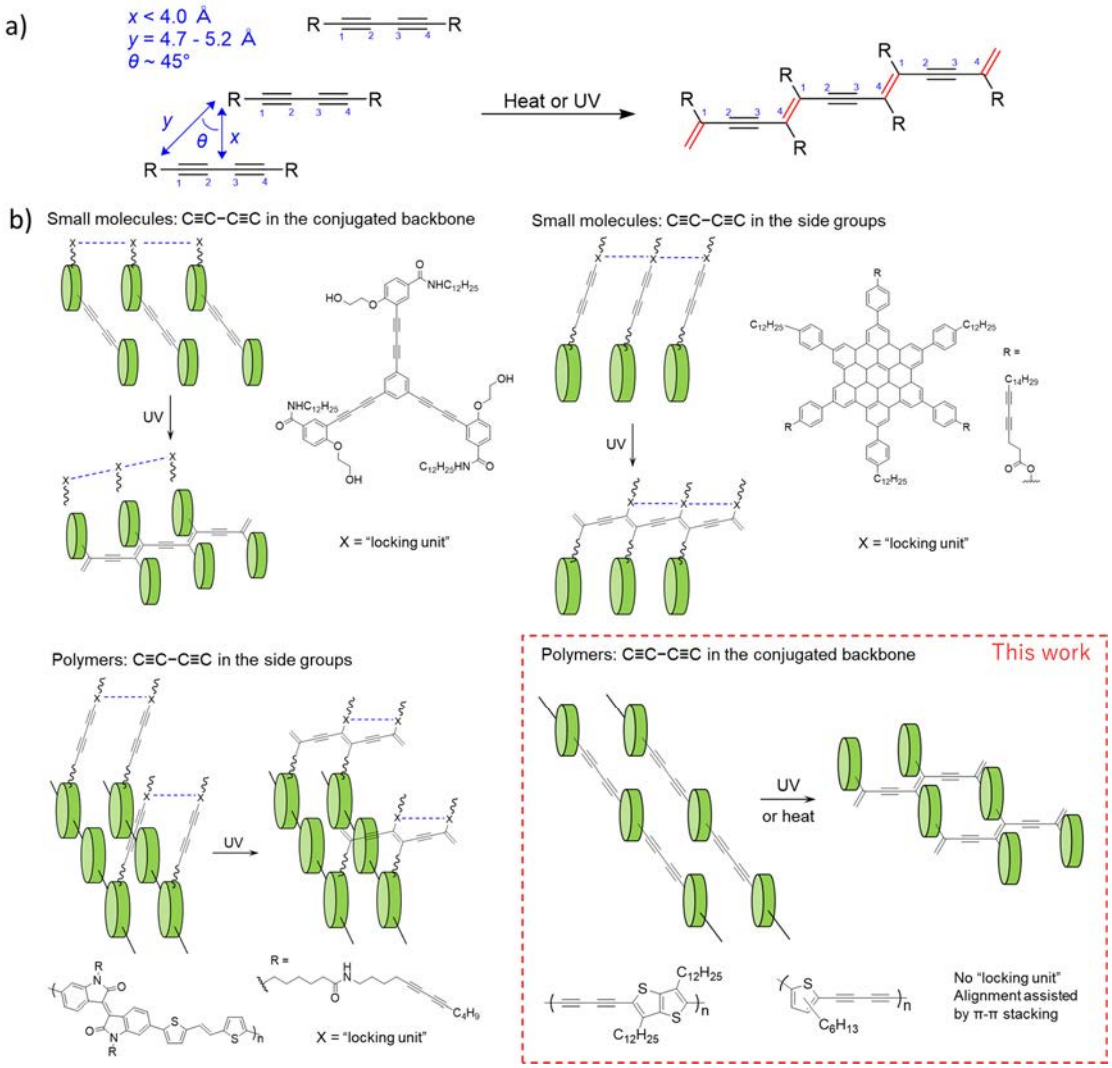
4.1. Introduction

Cross-linking can improve the π-π stacking and "freeze" the preferred molecular packing in organic semiconductor films. One of the ways to introduce cross-links is to utilize the topochemical 1,4-coupling reaction of 1,3-butadiyne units (i.e., C≡C−C≡C), which is also known as diacetylene.[147–149] The butadiyne units undergo polymerization under UV irradiation and/or thermal annealing to produce polydiacetylene (PDA) (Scheme 4.1a). Besides "freezing" the molecular packing motif, PDA chains can

contribute to the optoelectronic properties of the films because of the conjugated backbone. Due to the radical attack by the C1 atom of one C≡C−C≡C moiety to the C4 atom of the adjacent one (C4'), the monomer units must properly align.[150,151] If precisely controlled, this constraint can open prospects to create various anisotropic materials, such as 1D nanowires,[152] nanotubes[153] and 2D graphene-like polymers.[151] The most widely reported approach is the cross-linking of small molecules and polymers that possess butadiyne units in their side groups (Scheme 4.1b).[104,105,154] Some examples that were used for OFET applications are cross-linking of butadiyne-containing side groups of 1,6-di-(N-carbazolyl)-2,4-hexadiyne (DCHD) and hexa-*peri*-hexabenzocoronene (HBC).[103,104] Thus, cross-linked HBC films exhibited $\mu_h = 1.5$ cm^2 V^{-1} s^{-1}, which is up to three orders of magnitude higher than that of the pristine films.[104] To facilitate the alignment of the butadiyene moieties, hydrogen bond forming units (e.g., amides) were typically included into side groups.[105,152,154]

UV-induced interchain topochemical coupling of butadiyene units is also possible when they are included in the polymer main chain. The examples are mostly limited to amorphous non-conjugated polymers,[155–157] while the cross-linking of poly(arylenebutadiynylene)s are much less reported. For example, UV-induced cross-linking of poly(9-hexylcarbazole-3,6-diylbutadiynylene) was demonstrated in 1996 but no follow-up works were found in literature.[158] On the other hand, thermal cross-

linking of poly(thiophene-2,5-diylbutadiynylene)s[159,160] and poly(thieno[3,2-*b*]thiophene-2,5-diylbutadiynylene)[160] were reported as early as 1988 and 1992, respectively, but photopolymerization in these polymers has not been reported.



Scheme 4.1. (a) Topochemical polymerization of butadiyne (diacetylene) monomers by 1,4-coupling to form PDA. Newly formed bonds are given in red. (b) Examples of cross-linking of small molecules and conjugated polymers by topochemical polymerization of butadiynes.

There are at least two factors why cross-linking of poly(arylenebutadiynylene)s has now become an important topic. Firstly, poly(arylenebutadiynylene)s possess great

potential for the preparation of cross-linked films thanks to strong π-π stacking tendency of conjugated compounds, which can facilitate the alignment of the butadiyne units.[161] Secondly, poly(arylenebutadiynylene)s have gained increasing interest for semiconductor applications in recent years, but possible formation of cross-links has not been discussed.[162–167] The relative ease of topochemical polymerization of butadiyne (i.e., under device fabrication/test conditions) makes poly(arylenebutadiynylene) films susceptible to an unknown impact of potential cross-links. Therefore, it is timely to elucidate the possibility of cross-linking of poly(arylenebutadiynylene) films and its effect on the charge transport properties.

Poly(3-hethylthiophene-2,5-diylbutadiynylene) (PDET) and poly(3,6-didodecylthieno[3,2-*b*]thiophene-2,5-diylbutadiynylene) (PDETT) were chosen as potential candidates for in-film cross-linking, because in-bulk reactions have been well-studied for these polymers.[159,160] Solubilizing alkyl side groups were introduced into the polymers for solution processability. Spin-coated PDET films were cross-linked via thermal annealing and UV irradiation, while PDETT films were cross-linked only upon thermal annealing. The reaction was confirmed by UV–vis, Fourier-transform infrared (FTIR) and Raman spectroscopies, which showed that cross-links locally formed. Changes in film morphology before and after the cross-linking was studied by GIWAXS and tapping-mode AFM. DFT calculations and GIWAXS results showed that

PDETT possessed highly ordered molecular packing which was suitable for 1,4-coupling of butadiyne units. In addition, PDET films were amorphous. Therefore, PDETT film exhibited improved μ_h after cross-linking, despite its expected negative effect on the overall conjugation of the polymer backbone. On the other hand, butadiyne coupling reactions at random π-π stacked regions of PDET disrupted its macro-phase charge transport pathways.

4.2. Materials and Methods

4.2.1. Materials

All reagents and chemicals were purchased from Tokyo Chemical Industry (TCI), Kanto Chemical, Co., Inc., and Sigma Aldrich and used as received unless otherwise stated. 2,5-Bisethynyl-3-hexylthiophene (DET)[168] and 2,5-bisethynyl-3,6-didodecylthieno[3,2-*b*]thiophene (DETT)[168–170] were synthesized by using the modified procedures given in the literature. PDET and PDETT were from DET and DETT, respectively, as reported.[162]

4.2.2. General measurements

Instrumentation and measurement procedures of ^{1}H NMR, ^{13}C NMR, MALDI-TOF MS, GPC, TGA, DSC, UV–vis absorption spectroscopy and CV were identical to

those given in Chapter 2. New and modified experimental methods are described below.

Attenuated total reflection FTIR spectroscopy was measured on a JASCO FT/IR 4200 spectrometer. Raman spectra was measured on a custom-made micro-optical system comprising of a microscope of 100x objective lens (N.A. = 0.85), a 633-nm (for PDET) and 532-nm (for PDETT) excitation laser with a control of polarization angle, and a spectrometer (Isoplane 320, Princeton Instruments) for the detection of Raman-scattered light. Indium tin oxide (ITO)-coated glass was used as the working electrode in CV.

4.2.3. Cross-linking of films

For the characterization by FTIR and Raman spectroscopies, PDET and PDETT films (< 5 mm in diameter) were prepared by drop-casting 2–3 mg mL^{-1} chloroform solutions onto pre-cleaned glass substrates. For the UV–vis spectroscopy measurement, the films were spin-coated (1000 RPM) from 3 mg mL^{-1} chloroform solutions. For the CV measurements, the polymers were spin-coated from chloroform solutions (5–10 mg mL^{-1}) onto a 1 cm × 2 cm ITO/glass, and the excess film was removed to obtain the coated area of 1 cm × 1 cm. To induce cross-linking, the films (including OFET films below) were UV-irradiated in air for up to 3 h or thermally annealed in an Ar-filled glovebox on a hot plate at 100–200 °C for 10–15 min. Asahi MAX-303 Xenon Light

Source with an XHQA254 filter (254 nm with diameter of 20 nm) was used as a UV light source for cross-linking. The lamp was placed at a distance of ~8 cm from the films corresponding to the light intensity of ~500 W m^{-2}.

4.2.3. Theoretical calculations

DFT calculations were performed using Gaussian 16 and Gauss View 6 package[171,172] on TSUBAME 3.0 supercomputer at Global Scientific Information and Computing Center of Tokyo Institute of Technology. Alkyl side chains were reduced to methyl groups to save computational time in all calculations. For the details of the used basis set, see the results section.

4.2.4. OFET fabrication and characterization

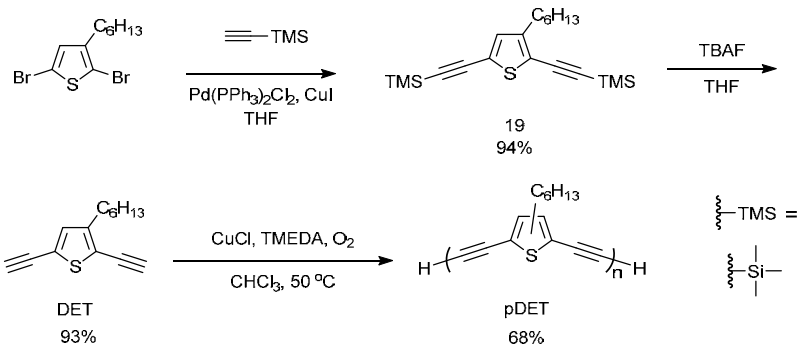
Preparation of n^+-Si/SiO_2/OTMS substrates and characterization of OFETs were done as described in Chapter 2. PDET films were spin-coated at the spin rate of 3000 RPM from 10 mg mL^{-1} chloroform solution, while PDETT films were drop-cast from 2 mg mL^{-1} chloroform solution. The films were cross-linked by thermal annealing or UV irradiation as described above. Gold electrodes were then vacuum deposited onto as-cast and cross-linked films to obtain BGTC OFETs.

4.2.5. Film morphology and microstructures

Films for GIWAXS and AFM were prepared by the methods similar to those of the OFETs. GIWAXS of PDETT films was measured at BL40B2 in SPring-8 (Hyogo, Japan). The samples were irradiated at a fixed incidence angle on the order of 0.125°, and the GIWAXS patterns were recorded with a 2-D image detector (PILATUS3 S 2M, Dectris, Ltd.). The wavelength of the X-ray beam was 1 Å, and the camera length was 350 mm. XRD patterns were obtained using a Bruker AXS D8 DISCOVER with GADDS (Cu Kα, wavelength = 0.154 nm) operated at 50 kV and 22 mA. The samples were exposed to the X-ray beam for 5 min with a sample-to-film distance of 200 mm. The GIWAXS pattern of PDET films was recorded on beamlines 13A1 in the National Synchrotron Radiation Research Center (NSRRC), Taiwan, with an X-ray wavelength of 1.02 Å and an incident angle of 0.12°. Tapping-mode AFM of as-cast and cross-linked PDET and PDETT films were measured as

4.3. Results and Discussion

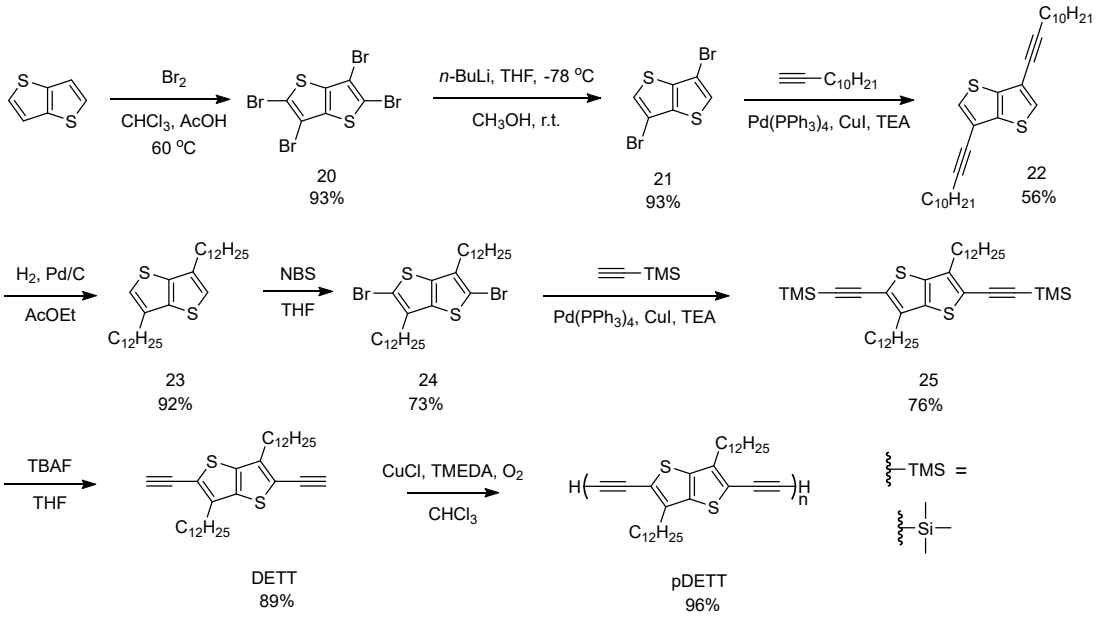
4.3.1. Polymer synthesis



Scheme 4.2. Synthesis of PDET.

PDET was synthesized in three steps from commercially available precursor (Scheme 4.2).[168] 2,5-Dibromo-3-hexylthiophene was converted into **19** by a typical Sonogashira coupling reaction using bis(triphenylphosphine)palladium(II) dichloride ($Pd(PPh_3)_2Cl_2$) and CuI as catalysts in a solution of THF and triethylamine (TEA). Trimethylsilyl (TMS) group was deprotected from **19** with tetrabutylammonium fluoride (TBAF) to afford DET. A colorless to pale yellow liquid DET monomer was highly unstable, and turned dark brown within 5–10 min upon removal of solvent at room temperature even under vacuum. On the other hand, an *n*-hexane solution (~40 mg mL^{-1}) of DET with a closed cap could be stored in a fridge at 10 °C, without noticeable color change for several days. However, as the high purity of the monomer is required, it was prepared immediately before the polymerization reaction. Freshly column-chromatographed fractions were combined and the *n*-hexane eluent was

evaporated in rotary evaporator (< 35 °C). When the solution was concentrated to ~2 mL, it was quickly added to the polymerization reaction flask containing a pre-made catalyst. Thus, PDET was prepared by Hay coupling in air-bubbled chloroform using CuCl/TMEDA as catalysts.[162] The crude polymer solution was precipitated into acidified methanol (with HCl) to remove the catalyst. Collected solid was not subjected to Soxhlet extraction to avoid the negative effect of heating. Instead, the solid was subsequently sonicated in cold acetone and chloroform. Most parts of the polymer were dissolved in chloroform (68%). Hence, this fraction was concentrated and re-precipitated into methanol to afford the target PDET. Note that molecular weight of the polymer could be conveniently controlled by adjusting the polymerization reaction time. PDET had M_n of 6.3 kg mol^{-1} and had excellent solubility in chloroform (>10 mg mL^{-1}).



Scheme 4.3. Synthesis of PDETT.

PDETT was synthesized in eight steps from commercially available precursor (Scheme 4.3).[162,168–170] Thieno[3,2-*b*]thiophene was treated with Br_2 under acidic conditions ($CHCl_3$ with AcOH) to give tetrabrominated product **20**.[169] Lithiation of **20** with 2 eq. of *n*-BuLi, followed by quenching with methanol gave 3,6-dibromo-thieno[3,2-*b*]thiophene (**21**).[170] Sonogashira coupling with 1-dodecyne, and the subsequent hydrogenation afforded the 3,6-dodecyl-thieno[3,2-*b*]thiophene (**23**). Then, **24** was obtained by bromination of **23** with NBS. Dibrominated product **24** was then converted into **25** by Sonogashira coupling reaction, followed by deprotection of TMS group with TBAF to afford DETT.[168] Again, a bright yellow solid DETT was unstable and darkened upon standing at room temperature, although the process took longer (>1 h) than that of DET. This allowed us to completely remove the *n*-hexane eluent from the column-chromatographed DETT prior to the polymerization reaction. Similar Hay coupling conditions as mentioned above were used for the preparation of PDETT.[162] After 3 h of reaction, the crude polymer contained mostly chloroform-soluble fraction (96%), while increasing the reaction time (>24 h) afforded the polymer that was only partially soluble in *o*-DCB. Thus, the chloroform-soluble fraction of PDETT had M_n of 5.1 kg mol^{-1}.

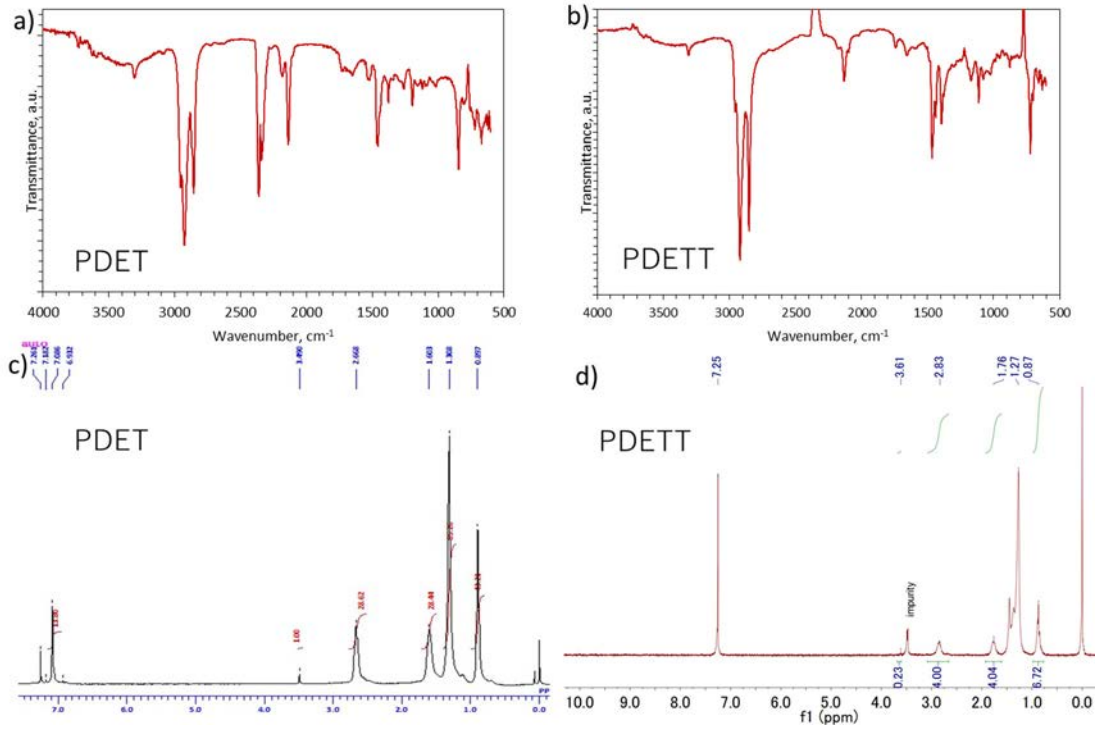


Figure 4.1. FTIR spectra of (a) PDET and (b) PDETT, and ^{1}H NMR spectra of (c) PDET and (d) PDETT.

Since the M_n of PDETT was hindered by its low solubility, the M_n of PDET was then deliberately decreased to a comparable value. Thus, PDET and PDETT had degrees of polymerization of ~29 and ~10, respectively. Successful synthesis of target polymers was confirmed using FTIR and ^{1}H NMR spectroscopies (Figure 4.1). The characteristic peaks of the C≡C−C≡C moiety were observed at ~2180 and ~2130 cm^{-1} in the FTIR spectra of both polymers. ^{1}H NMR spectra also contained the peak at ~3.5 ppm, which could be ascribed to the terminal alkynes (≡CH). Molecular weights, thermal, optical and electrochemical properties of PDET and PDETT are summarized in Table 4.1.

Table 4.1. Summary of the properties of PDET and PDETT.

	M_n, kg mol^{-1}	PDI	T_d, °C [(a)]	T_g, °C [(b)]	T_{exo}, °C [(b)]	$E_{g,opt}$, eV [(c)]	E_{HOMO}, eV [(d)]	E_{LUMO}, eV [(e)]
PDET	6.3	3.1	369	–	152, 198	2.33	−5.87	−3.54
PDETT	5.1	2.8	263	63	107, 172, 261	2.12	−5.68	−3.56

[(a)] Determined as the onset of weight loss. [(b)] Ddetermined from the first heating cycle in DSC. [(c)] Determined from UV–vis spectroscopy. [(d)] Evaluated by CV. [(e)] Calculated as $E_{LUMO} = E_{HOMO} + E_{g,opt}$.

Drop-cast films of PDET became insoluble in chloroform (although partially soluble in *o*-DCB), after irradiation with UV light (λ = 254 nm) for 1 h or thermally annealing at 200 °C for 15 min. In addition, films darkened from yellow to brownish red upon treatment. On the other hand, the PDETT was not sensitive to UV irradiation, and drop-cast films retained their solubility and color. The color changed from bright red to dark red after thermal annealing at 200 ºC for 15 min. The annealed films became insoluble both in chloroform and *o*-DCB. These changes can be considered as evidence of cross-linking in the polymer films.

4.3.2. Thermal properties

Firstly, cross-linking in bulk polymers was confirmed using DSC and TGA measurements, which could be compared to the previously reported results.[159,160] TGA showed that T_d of PDET and PDETT were 369 and 263 °C, respectively (Table 4.1 and Figure 4.2). Therefore, the exothermic peaks (T_{exo}) appearing below T_d could be assigned to 1,4-coupling reactions.[159,160] PDET exhibited well-defined exothermic

peaks with an onset at ~110 °C, while those of PDETT were less-defined (onset at ~100 °C). Rather large exothermic peak of PDETT at 261 °C was ascribed to its decomposition, which matched with the onset of the mass loss in the TGA curve. PDETT exhibited T_g at 63 °C thanks to high degree of alkylation. Thus, these results confirmed that both bulk PDET and PDETT underwent cross-linking upon thermal treatment. The following sections present the properties of the polymer films before and after cross-linking.

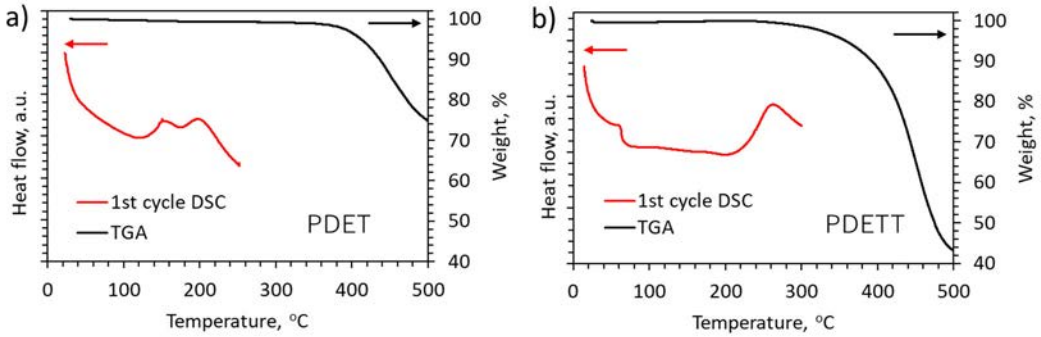


Figure 4.2. TGA and DSC curves of (a) PDET and (b) PDETT.

4.3.3. Optical and electrochemical properties

Cross-linking of the polymer films was studied by thermal annealing (on a hot plate in an Ar-filed glovebox) or UV irradiation (in air) of polymer films spin-coated onto glass substrates (Figure 4.3). PDET exhibited featureless UV–vis absorption spectra in solution with the absorption band onset of ~510 nm. A slight band shoulder

at 541 nm (i.e., 0−0 transition peak) appeared and the overall absorption onset shifted to 532 nm in the as-cast film, while the absorption maxima remained almost unchanged. This was attributed to the straightening of the polymer backbone and overall tighter π-π stacking. The absorption peak of the films shifted from 461 to 458 nm after UV irradiation and the absorption band shoulder decreased. The thermally annealed PDET film exhibited a further blue-shift of the absorption peak to 440 nm with the complete loss of the band shoulder. Backbone coplanarity was disturbed upon formation of cross-links due to the twisting of the polymer backbone, which led to the observed blueshifts and loss of the 0−0 transition peak.[137]

PDETT exhibited a well-defined shoulder peak in solution, indicating the presence of pre-aggregates. The as-cast film had essentially identical spectra, further suggesting that aggregation was substantial in the solution. This could be caused by the highly planar backbone of the polymer. Absorption peak of the PDETT film did not shift after thermal annealing but the intensity of the shoulder peak decreased. These results suggested that although the cross-links disturbed the backbone planarity,[137] it was not sufficient enough to overcome the π-π stacking interactions. This can be the case if the cross-links could not form globally but appeared in isolated sites.

Typically, upon quantitative formation of PDA-like structures the onset of absorption band blue-shifts, while a new band at ~300 nm forms.[105,153,154] The absence

of such changes in PDET and PDETT films further supported the hypothesis that the cross-links were not clustered. Similar behavior was observed for poly(9-hexylcarbazole-3,6-diylbutadiynylene).[158]

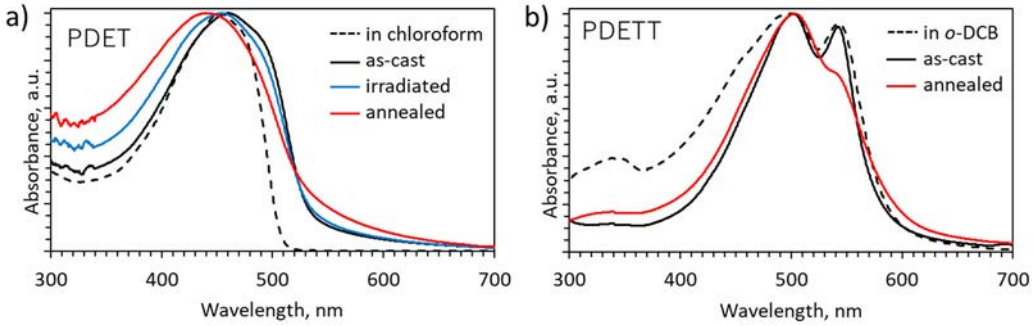


Figure 4.3. Solution and thin film UV–vis absorption spectra of (c) PDET and (d) PDETT.

CVs of the films before and after cross-linking were measured in a three-electrode setup with Pt wire, Ag/AgCl and ITO/glass as counter, reference and working electrodes, respectively (Figure 4.4). The onset of the oxidation peak ($E_{ox,onset}$) of the as-cast PDET was +1.08 V (vs. Fc/Fc^+), while those of the UV-irradiated and annealed PDET films were +1.12 and +1.19 V, respectively. The shift of the $E_{ox,onset}$ could be attributed to the disrupted conjugation and π-π stacking due to formation of cross-links. On the other hand, the CV curves of the pristine and cross-linked PDETT films showed strong resemblance with an $E_{ox,onset}$ at +0.88 V vs. Fc/Fc^+. This supported the fact that the cross-links were not global and did not negatively affect the π-π stacking. On the

other hand, the oxidation peak itself shifted to a lower potential, indicating that π-π stacking was in fact improved.

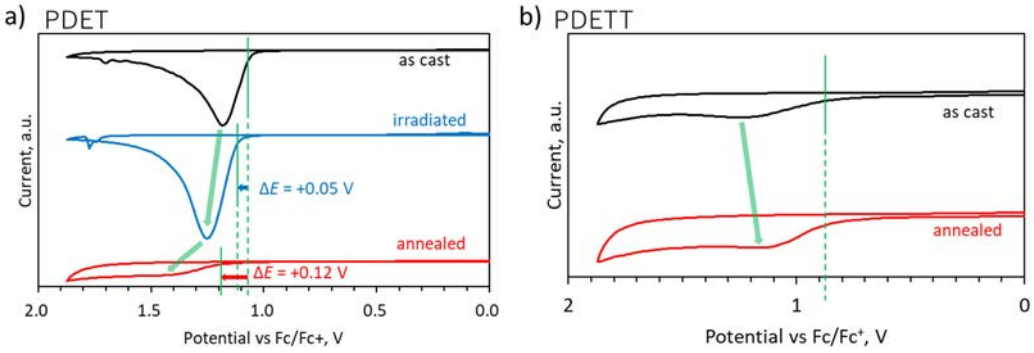


Figure 4.4. CV curves of (a) PDET and (b) PDETT films.

4.3.4. FTIR and Raman spectroscopy

The chemical changes upon cross-linking were investigated using FTIR and Raman spectroscopies (Figure 4.5). Films were drop-cast onto glass substrates followed by UV-irradiation in air or thermal annealing on a hot plate in an Ar-filled glovebox. The intensities of the peaks corresponding to the C≡C−C≡C moiety (at 2182 and 2134 cm^{-1})[152,158] decreased when the PDET film was UV-irradiated and thermally annealed. A part of the C≡C−C≡C units was consumed upon formation of the cross-links. The relative intensities of the peaks suggested that more C≡C−C≡C units reacted in the thermally annealed films than in UV-irradiated film. These results agreed with the more significant change of UV–vis spectra and CV curves for the heat-treated films.

Similarly, the intensities of the peaks at 2172 and 2132 cm^{-1} decreased in a thermally annealed PDETT film.

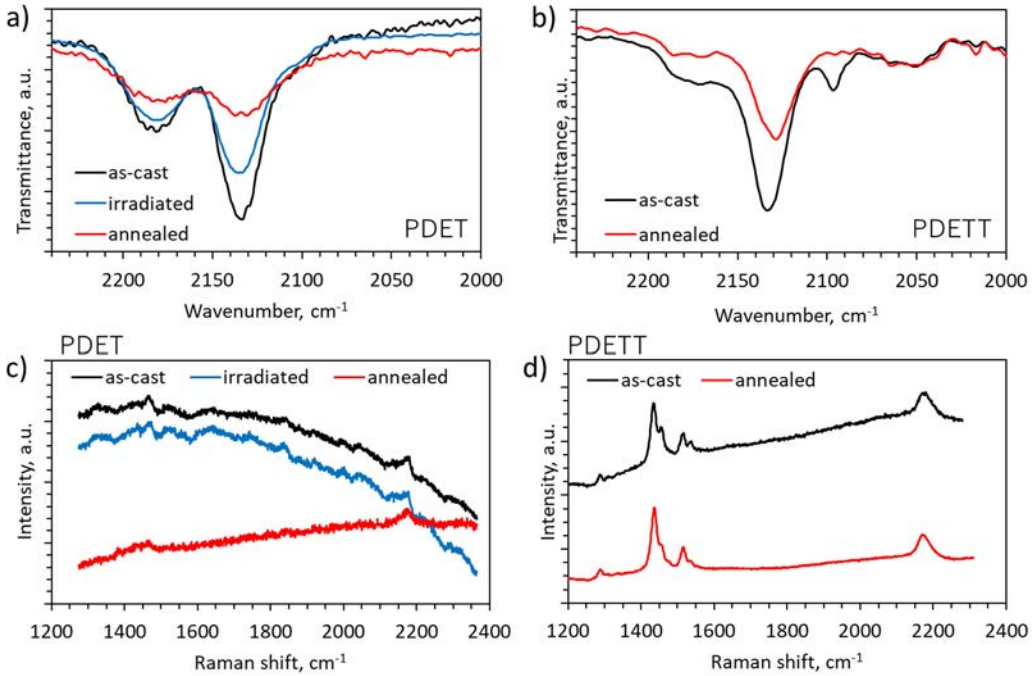
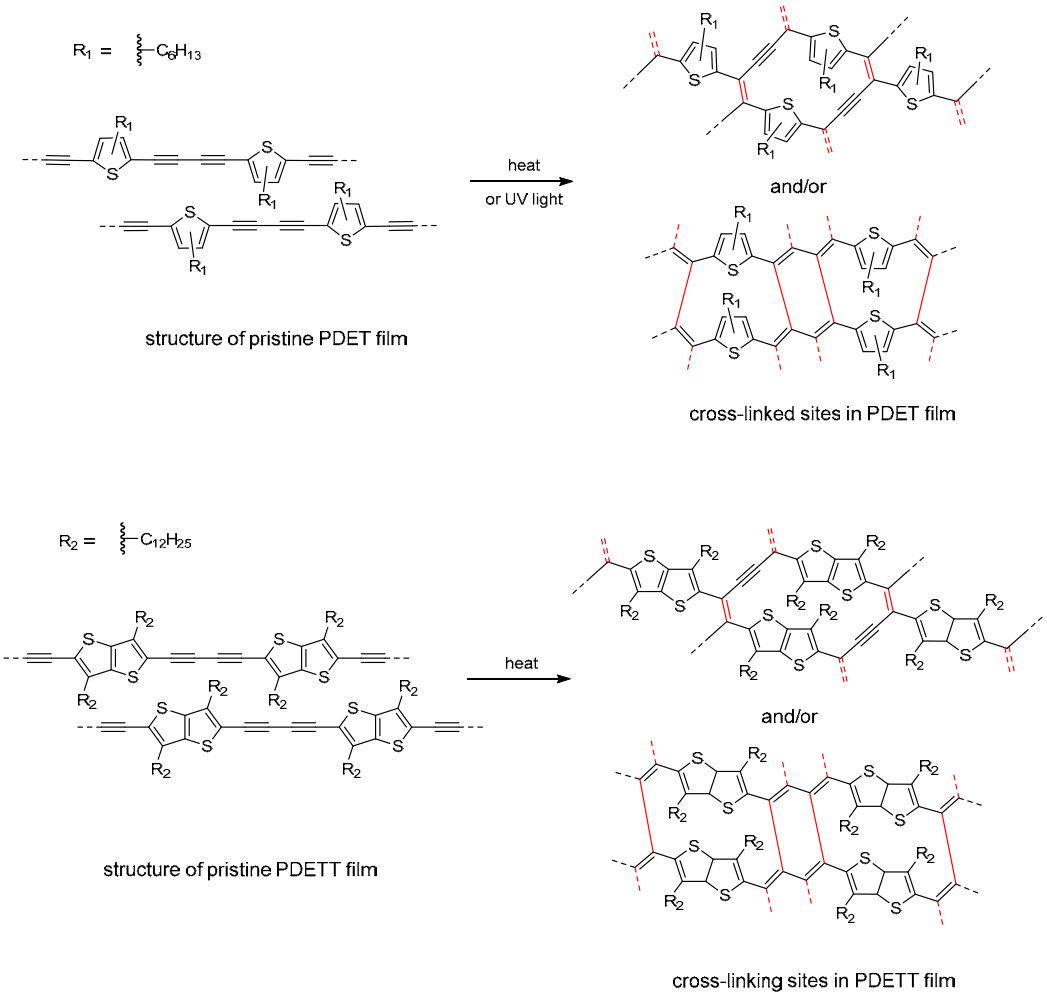


Figure 4.5. FTIR spectra of (a) PDET and (b) PDETT films and Raman spectra of (c) PDET and (d) PDETT films.

Typically, upon cross-linking of butadiyne-containing small molecules and polymers, complete loss of Raman peaks ascribed to C≡C−C≡C units were reported.[105,152,154,173] However, due to the non-quantitative reactions in PDET and PDETT films, the differences in Raman spectra of the pristine and cross-linked polymer films were small. Therefore, the relative ratios of the peaks were used to construct the possible chemical structures of the cross-links in the treated films. Raman spectra of PDET films had a large background noise (633-nm laser), which was caused by the

strong fluorescence of PDET.[174] The main peaks in PDET films were observed at 1435, 1521 (C=C), 2042, 2127 cm^{-1} (C=C−C≡C) and 2178 cm^{-1} (C≡C−C≡C).[153,173] The intensities of peaks at 1435, 1521, 2042, and 2127 cm^{-1} increased relative to that at 2178 cm^{-1} when the film was UV-irradiated, suggesting that the cross-linking underwent via formation of PDA-like segments (i.e., repeating C=C−C≡C). tThermally annealed films of both PDET and PDETT did not exhibit peaks at ~2050 and ~2130 cm^{-1}. These results indicated that the C=C−C≡C moieties did not form upon heat treatment, and that the cross-linking instead increased the content of C=C bonds. Previous reports concluded that thermally annealed PDET and PDETT cross-linked via formation of C=C−C=C segments, instead of C=C−C≡C.[159,160] However, the small amplitudes of changes in the Raman spectra makes it difficult to unambiguously identify the exact structure of the cross-links. Therefore, both C=C−C=C and C=C−C≡C segments can be present in cross-linked films (Scheme 4.4).



Scheme 4.4. Illustration of ideal cross-linking of the PDET and PDETT films by 1,4-coupling of butadiyne moieties (newly formed bonds are given in red).

4.3.5. Theoretical calculations

DFT calculations were used to elucidate the polymer backbone structure and possibility of alignment of butadiyne units leading to the cross-linking. Geometry optimization and molecular orbital calculations were done on isolated polymer chains with 6 repeat units (alkyl side chains reduced to methyl groups) using B3LYP method with 6-31+G(d,p) basis set (Figure 4.6). The results showed that the backbone of PDET

was zigzagged and the adjacent DET units were nearly coplanar (172.2–177.6°). The dihedral angles between DET units were significantly lower than those in benzene-ring based small molecules, such as 1,4-diphenylbutadiyne.[175] A polymer chain with a pair of *cis*-coupled DET units was also stable. This suggested that polymer chain can potentially be coiled into helical structures as reported for poly(benzene-1,3-diylbutadiynylene).[153] The backbone of PDETT was straight and completely planar.

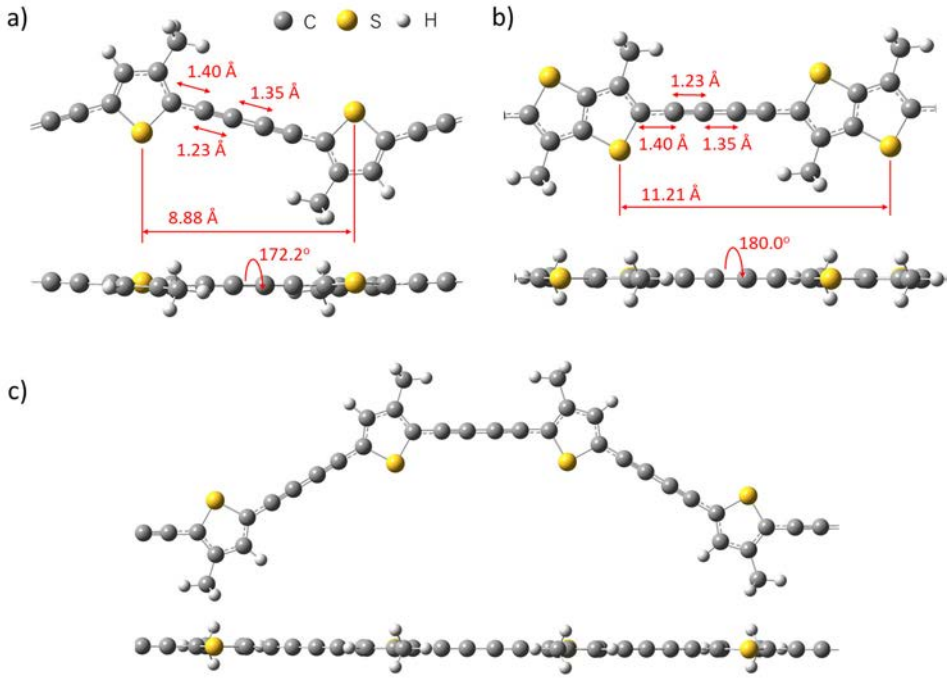


Figure 4.6. Geometry optimization results using DFT calculations. Top and side views of the two repeat unit segments of (a) PDET and (b) PDETT. (c) Top and side views of 4 repeat units of PDET with one of the DET–DET segments coupled in *cis*-configuration. Calculations were performed with B3LYP/6-31+G(d,p) basis set in 6 repeat units. Alkyl chains were reduced to methyl groups to save computational time.

The HOMOs and LUMOs were distributed uniformly along the polymer chain in both PDET and PDETT (Figure 4.7), owing to the absence of sharp difference in

electron affinities of the repeat units. The calculated E_{HOMO}s of PDET and PDETT were −5.29 and −5.14 eV, respectively, while the E_{LUMO}s were −3.00 and −2.90 eV, respectively. Thus, the theoretical calculations support the CV and UV–vis spectroscopy results that PDET has deeper energy levels than PDETT.

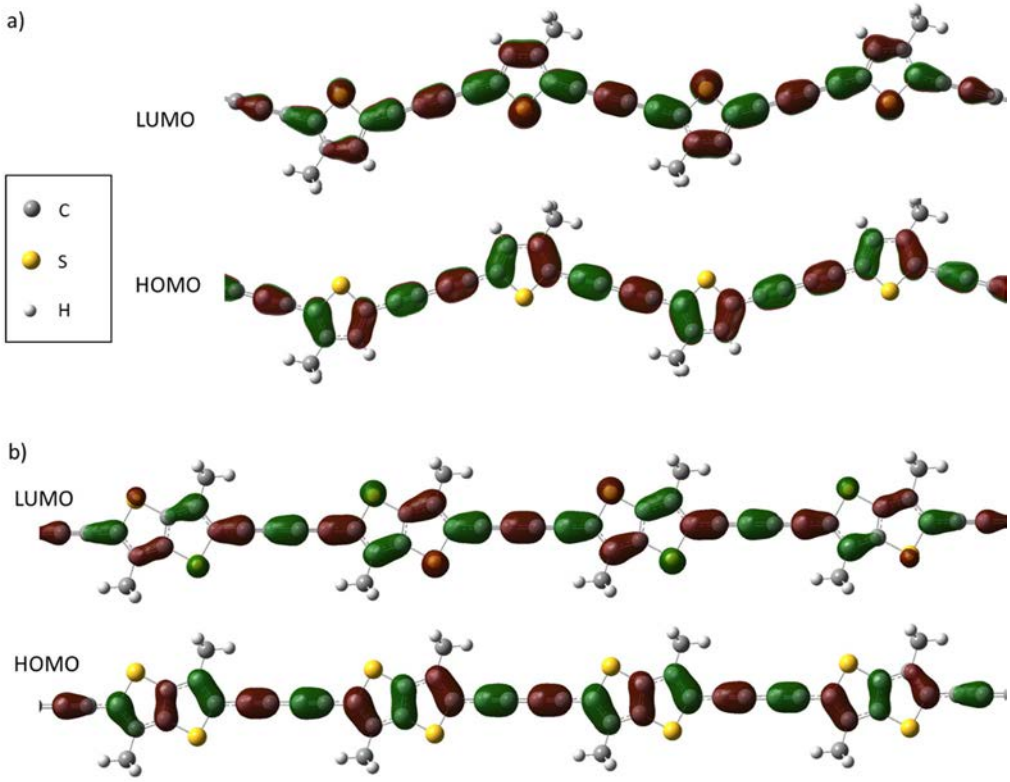


Figure 4.7. HOMOs and LUMOs of (a) PDET and (b) PDETT, calculated with B3LYP/6-31+G(d,p) basis set. Calculations were performed on 6 repeat units. Alkyl chains were reduced to methyl groups to save computational time.

The zigzagged backbone and possible coiling of PDET made its butadiyne moieties less probable to align for cross-linking. Thus, stacking of more rigid and straight PDETT polymer chains was simulated using DFT calculations. Since these calculations require a consideration of intermolecular interactions, the first objective

was to choose a level of theory that is modified for long-range interactions. The literature has shown that different functionals (e.g., ωB97X-D, CAM-B3LYP, M062X and B3LYP) give results with varying accuracy depending on the system of interest.[176–179] Therefore, in this work, performances of CAM-B3LYP[180] and ωB97X-D[181] functionals with 6-311+G(d,p) basis set were compared by optimizing the geometry of DETT−DETT segment. The ωB97X-D method gave an unexpectedly large DETT−DETT backbone twist with a vast deviation in the E_{HOMO} value compared to the experimental results. The CAM-B3LYP method gave reasonable results (i.e., planar backbone and E_{HOMO} deviation of <0.3 eV), hence further calculations were continued with this functional.

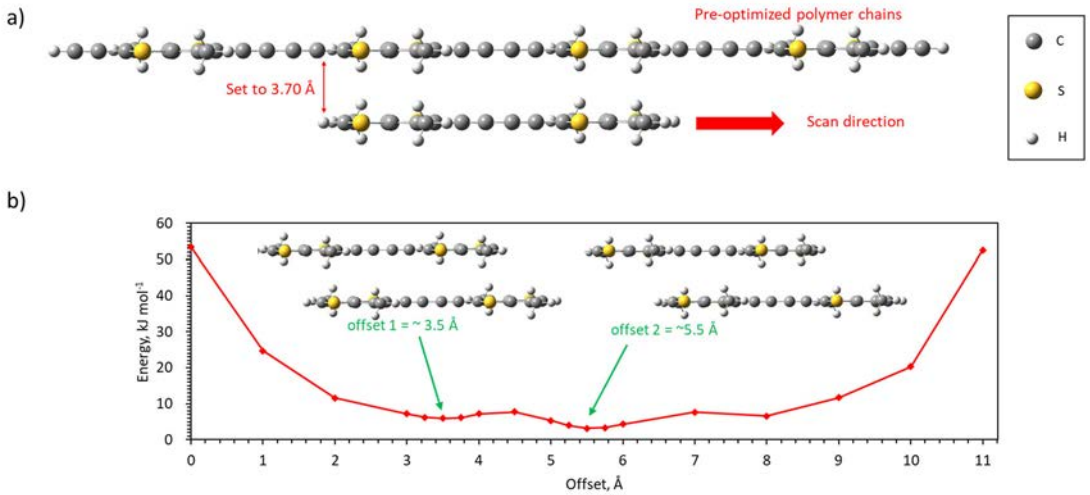


Figure 4.8. (a) Representation of a rigid scan of 4DETT and 2DETT separated by 3.7 Å. (b) Basis set superposition error (BSSE) corrected total electronic energies calculated at different offset values using CAM-B3LYP/6-31+G(d,p) basis set. 0 kJ mol^{-1} corresponds to the sum of the total electronic energies of isolated 4DETT and 2DETT. Due to high computational cost, counterpoise corrections to address BSSE were included only at offsets of 2, 4, 6 and 9. BSSE was extrapolated to other results by using a quadratic fit. Alkyl chains were reduced to methyl groups in all calculations to save computational time.

Rigid scan of a DETT dimer (2DETT) along the long axis of a DETT tetramer (4DETT) was performed using a smaller basis set of 6-31+G(d,p). The fragments were placed 3.70 Å apart (typical π-π stacking distance), and single point energy of the system was calculated at a scan step of 2 Å (Figure 4.8a). Basis set superposition error (BSSE) was addressed by extrapolating the counterpoise corrections calculated at 4 points to the whole energy scan region. In general, this approach can be helpful to approximate the stacking geometry that gives the lowest repulsion between the units. Thus, two minima were identified at offsets of ~3.50 and ~5.50 Å (Figure 4.8b). The latter was slightly deeper and it was closer to the structure with the lowest extent of face-on alignment between the thieno[3,2-*b*]thiophene units (i.e., half the length of DETT: 5.6 Å). These two offsets were then used to construct input structures for relaxed geometry optimizations of two face-on stacked 2DETT fragments with larger basis set of 6-311+G(d,p). Refined offsets of 3.42 and 5.46 Å were obtained, with the latter being marginally deeper by 1.77 kJ mol^{-1} (Figure 4.9). The offset 3.42 Å had a tighter packing of alkyl side groups and exhibited C1-to-C4' separation of 3.95 Å. This was within the required alignment range for the topochemical 1,4-coupling of C≡C−C≡C units.

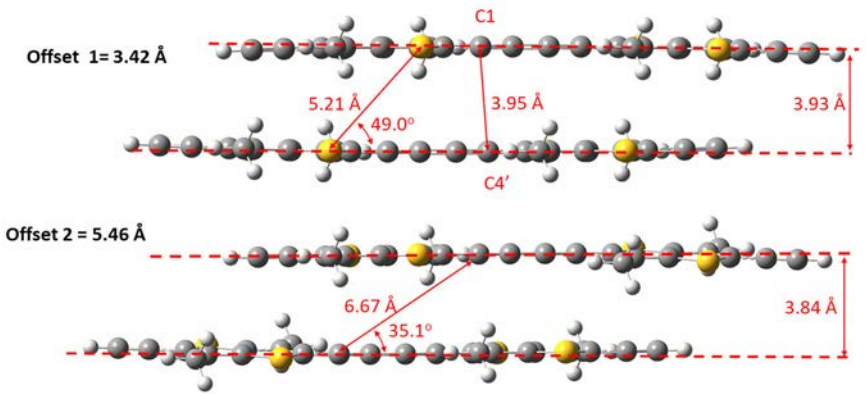


Figure 4.9. Face-stacked dimers of two repeat DETT units optimized with CAM-B3LYP/6-311+G(d,p). Alkyl chains were replaced with methyl groups to save computational time.

4.3.6. Film morphology and microstructures

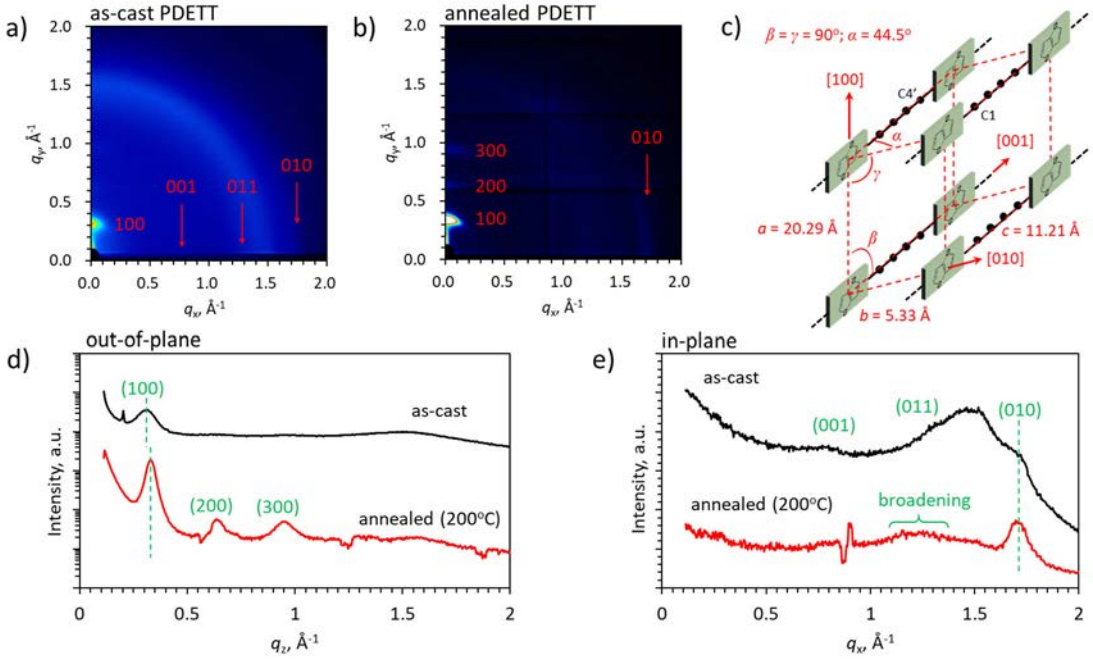


Figure 4.10. GIWAXS images of (a) as-cast and (b) annealed PDETT films. (c) Illustration of polymer packing and unit cell of as-cast PDETT (not to scale). Alkyl chains were omitted for clarity. GIWAXS 1D profiles of as-cast and annealed films of PDETT in (d) out-of-plane and (e) in-plane directions.

GIWAXS was used to gain insight into the actual molecular packing in polymer films. As-cast PDETT film exhibited a (100) peak in the out-of-plane direction (q_Z) and a weak (010) peak in the in-plane direction (q_X), which was attributed to the edge-on molecular packing orientation (Figure 4.10). The positions of the (100) and (010) peaks gave d_L = 20.29 Å and $d_{\pi\text{-}\pi}$ = 3.70 Å, respectively. Since d_L was slightly larger than the length of a dodecyl chain (~16 Å), the alkyl side groups were interdigitated. Two additional broadenings at 0.80 and 1.27 $Å^{-1}$ in the in-plane direction were determined, corresponding to separations of 7.87 and 5.02 Å, respectively. Considering the offset packing suggested by DFT calculations, these peaks were assigned to (001) and (011) reflections, respectively.[182] Then, DETT moieties assumed a monoclinic unit cell with a = 20.29 Å, b = 5.28 Å, c = 11.21 Å and α = 44.5° (Figure 4.10c). The offset packing in PDETT is not surprising because the $d_{\pi\text{-}\pi}$ = 3.70 Å is too short for alignment of alkyl side groups (~4.3 Å).[183] The offset between DETT units in this unit cell is 3.76 Å, which was closer to 3.42 Å than to 5.46 Å, contrary to DFT calculation results. Thus, the offset 5.46 Å was not the optimal one in the real film. This could be caused by the hydrophobic nature of alkyl side groups, which would prefer tighter packing (i.e., offset 3.76 Å) in a polar solvent like chloroform. The DFT calculations took into account neither the hydrophobic interactions nor the solvent effect. Nevertheless, the

monoclinic unit cell of the as-cast PDETT had the calculated C1-to-C4' separation of 3.99 Å, which is suitable for the topochemical polymerization.[150,153]

High crystallinity of the thermally annealed PDETT films can be seen from the presence of (*h*00) peaks up to three orders in the out-of-plane direction and much more intense (010) peak in the in-plane direction. Although $d_{\pi\text{-}\pi}$ remained the same, d_L was significantly shortened to 18.94 Å, showing the tendency of the alkyl groups to interdigitate even further upon heating above the T_g. Contrary to the intensification of the (010) peak, the intensities of the (001) and (011) reflections decreased significantly. A new broadening at 1.10–1.35 $Å^{-1}$ (4.65–5.71 Å) appeared. These results indicated that a new molecular packing phase emerged in the annealed film at the expense of the monoclinic unit cell found in the as-cast film. The new broadening could not be attributed to the stacking with ~5.6 Å offset, whose (001) and (011) peaks were both expected to appear at ~1.0 Å. In addition, the broadening did not correspond to reflections that could arise from slipped lamellar stacking (i.e., triclinic unit cell, $\beta \neq 90°$) with plausible alkyl chain separations. Therefore, it was concluded that the initial monoclinic unit cell was consumed in cross-linking. The formed covalent bonds then forced the remaining polymer chains to adopt a non-optimal packing and produce a new phase with possibly tilted π-π stacking (i.e., $\gamma \neq 90°$). However, since this packing would no longer be optimal for cross-linking, the reaction could not propagate to the whole

film. Thus, cross-linking was limited to certain sites and other parts of the polymer chains assumed a highly ordered packing. This hypothesis also explains why UV irradiation did not induce cross-linking in PDETT: the reorganization of molecular packing involved in the cross-linking was high in energy, which could not be provided by light absorption.

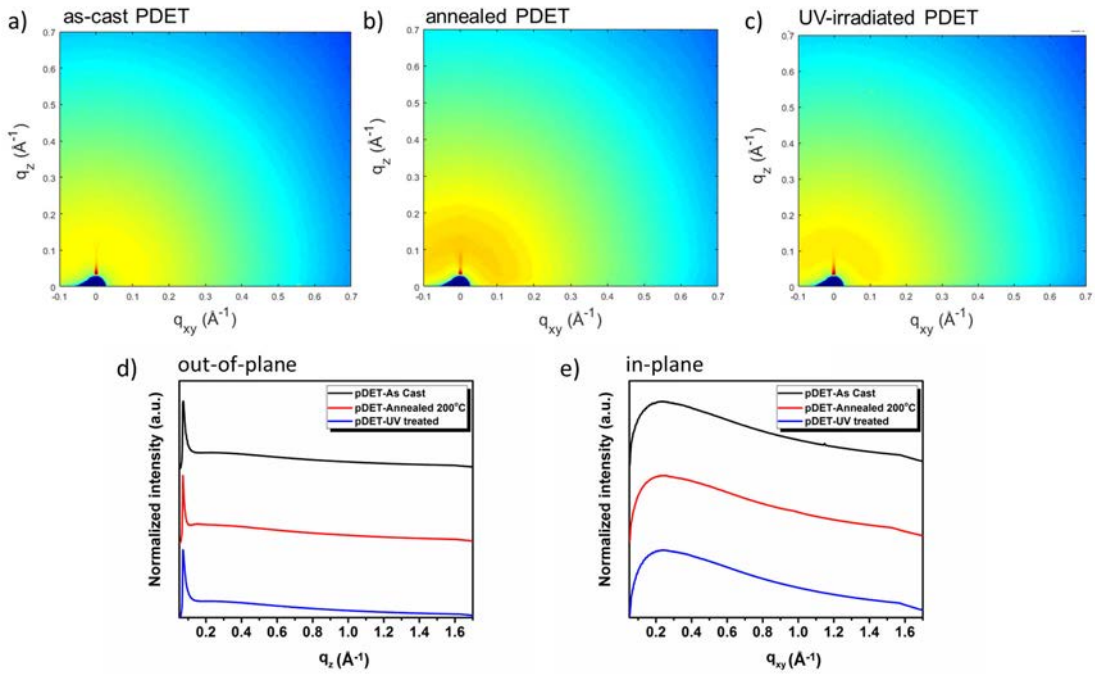


Figure 4.11. GIWAXS images of (a) as-cast, (b) annealed and (c) UV-irradiated PDET films. GIWAXS 1D profiles of as-cast, annealed and UV-irradiated films of PDET in (d) out-of-plane and (e) in-plane directions.

GIWAXS images of PDET before and after cross-linking did not show (*h*00) and (0*k*0) reflections (Figure 4.11). Thus, the films were amorphous without notable ordering, which could be expected from the zigzagged polymer backbone that also had potential for coiling. The absence of ordered π-π stackings suggested that there were no

large sites with aligned C≡C−C≡C units as well. The amorphousness of the films does not exclude the possibility of randomly distributed locations with proximity of C≡C−C≡C units between a few polymer chains. Cross-linking could take place at such isolated locations. A similar 1,4-coupling of butadiynes was reported for amorphous polymers, such as poly(*α*,*ω*-alkyldiyne)s[155] and various other non-conjugated polymers.[156,157] Note that such cross-linking is not truly PDA-like.

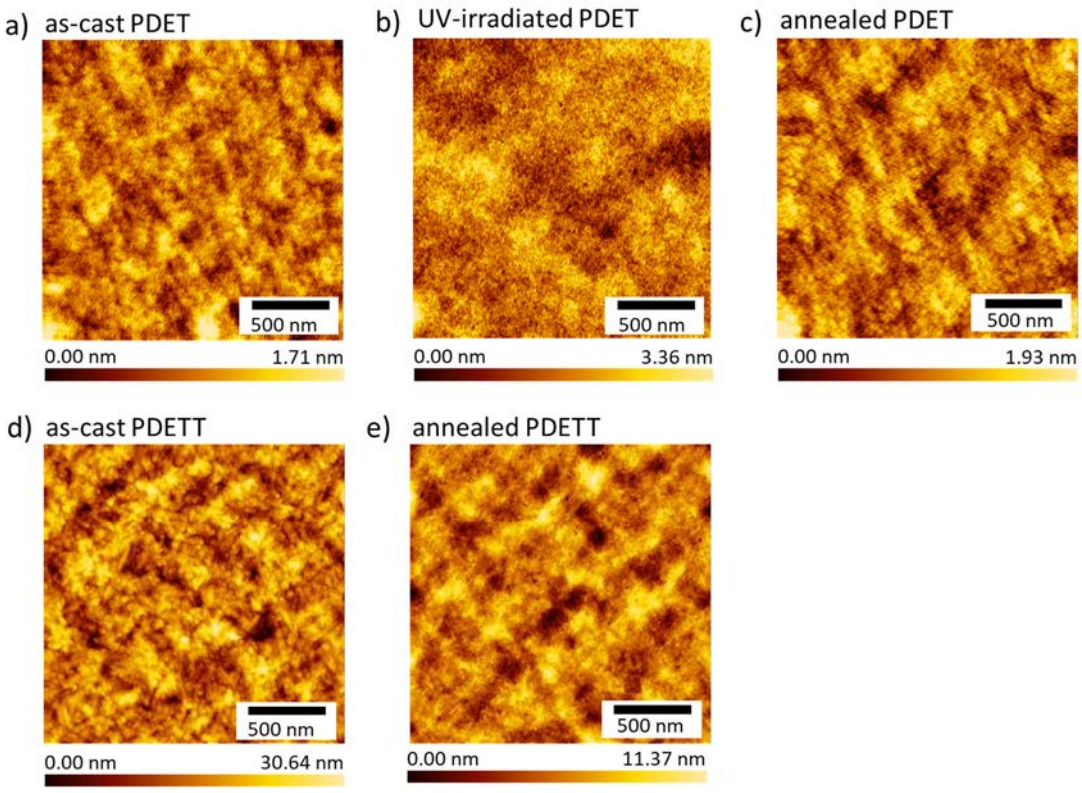


Figure 4.12. Tapping-mode AFM images of (a) as-cast, (b) UV-irradiated, (c) and thermally annealed PDET films, (d) as-cast and (e) thermally annealed PDETT films.

Tapping-mode topographical AFM was measured to investigate the surface morphology changes upon cross-linking of the polymers (Figure 4.12). The as-cast

PDET film exhibited uniform and smooth surface. The surface of the UV-irradiated film had fine structures, which could form due to the clustering of the polymer chains near the cross-linking sites Thus, the root mean square (RMS) surface roughness increased from 0.26 to 0.52 nm. The surface of the thermally annealed film resembled that of the as-cast one and the RMS surface roughness was similar at 0.30 nm.

The as-cast PDETT film had larger surface features and the RMS surface roughness was 4.73 nm. This was consistent with the presence of pre-aggregates in the deposition solution. Thermally annealed film exhibited small surface structures, while the underlying layer still resembled that of the as-cast film. The RMS surface roughness decreased to 1.73 nm. The smaller crystallites could form due to the phase separation between isolated cross-linking sites. Therefore, one can conclude that cross-linking sites could act as nucleation centers for highly ordered crystalline phase of the polymer. The high crystallinity of the annealed film observed in GIWAXS results is in agreement with these observations.

4.3.7. Effect of cross-linking on charge transport

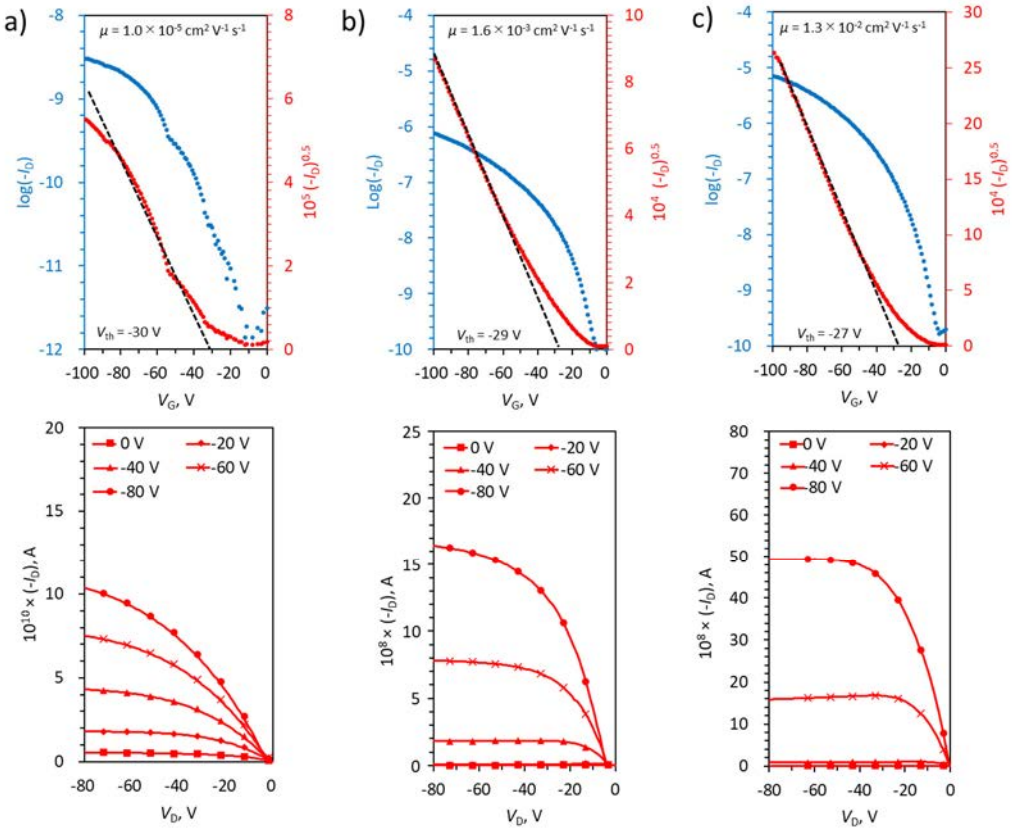


Figure 4.13. Selected transfer and output curves of BGTC OFETs based on (a) as-cast PDET film, (b) as-cast PDETT film and (c) thermally annealed (200 °C) PDETT film. Devices based on the UV-irradiated and thermally annealed PDET did not show transfer curves.

The effects of cross-linking on the charge transport properties were investigated in OFETs with BGTC configuration tested under air (Figure 4.13 and Table 4.2). The films were deposited onto n^+-Si/SiO_2/OTMS substrate and cross-linked by thermal annealing or UV-irradiation, followed by vacuum deposition of gold contacts. Due to the amorphousness, the as-cast film of PDET exhibited the limited μ_h of 1.0×10^{-5} cm^2 V^{-1} s^{-1} (Figure 7a). In addition, merely 3 out of 12 devices prepared on the same film showed transfer curves, indicating that the π-π stacked locations needed for interchain

charge hopping were scarce. Since cross-linking consumed these randomly distributed interchain charge transfer sites, both UV-irradiated and thermally annealed films lost the overall charge transport properties. The as-cast PDETT films exhibited the μ_h of 1.6×10^{-3} cm^2 V^{-1} s^{-1}, due to the higher crystallinity of PDETT films. The thermally annealed film showed an improved μ_h of 1.3×10^{-2} cm^2 V^{-1} s^{-1}, owing to the overall increase in the crystallinity of the film (GIWAXS results).

Table 4.2. Summary of OFET performances of PDET and PDETT.

	Annealing *T*, °C [(a)]	**μ_h, cm^2 V^{-1} s^{-1}** [(b)]	**V_{th}, V** [(b)]	**I_{on}/I_{off}**
PDET [(c)]	as-cast	$(1.0 \pm 0.5) \times 10^{-5}$	-26.2 ± 6.4	10^4
PDETT [(d)]	as-cast	$(1.6 \pm 0.4) \times 10^{-3}$	-28.4 ± 2.0	10^5
	150 °C	$(4.4 \pm 1.2) \times 10^{-3}$	-28.1 ± 4.7	10^5
	200 °C	$(1.3 \pm 0.7) \times 10^{-2}$	-30.9 ± 8.1	10^5
	250 °C	$(2.1 \pm 1.2) \times 10^{-3}$	-38.1 ± 6.1	10^4

[(a)] Annealed on a hot plate in an Ar-filled glovebox for 15 min. [(b)] Range represents average deviation.

[(c)] Results are average of 3 devices. UV-irradiated and annealed films did not exhibit transfer curves.

As observed throughout this work, cross-links did not form globally in the films. Therefore, the effect of charge transport in the PDA backbone[184] can be neglected in the further discussion. Then, thermal annealing and low-extent cross-linking of the butadiyne units of poly(arylenebutadiynylene)s should have an opposing effect on the charge transport properties. On the one hand, thermal annealing improves the μ due to the increased crystallinity of the film. However, cross-linking sites degrade it due to the perpendicular geometry, which is unfavorable for interchain charge hopping. In other words, the positive effect of the thermal annealing outweighed the negative effect of

low-extent cross-linking in PDETT due to rigid and straight polymer backbone. There were fewer π-π stacked regions with long-range order in PDET. Consumption of these sites by the cross-linking led to the loss of the interchain charge hopping locations. Therefore, the cross-linked PDET films lost the macro-scale charge transport properties. This hypothesis is illustrated in Figure 4.14.

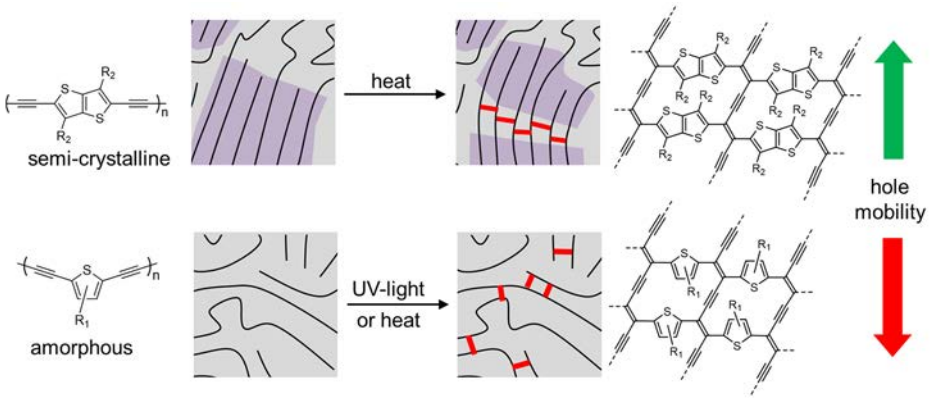


Figure 4.14. Illustration of the effect of cross-linking on the film microstructure and charge transport pathways in PDET and PDETT. Red bars indicate cross-links that block the interchain charge transfer sites due to the chemical bond geometry.

4.4. Conclusion

Low-extent topochemical cross-linking of the PDET and PDETT films via 1,4-coupling of butadiyne moieties was confirmed. DFT calculations and GIWAXS results showed that PDETT had molecular packing that is suitable for the cross-linking. However, due to necessary energy for the reorganization of molecular packing, only thermal annealing could induce the cross-linking. PDET exhibited amorphous films and

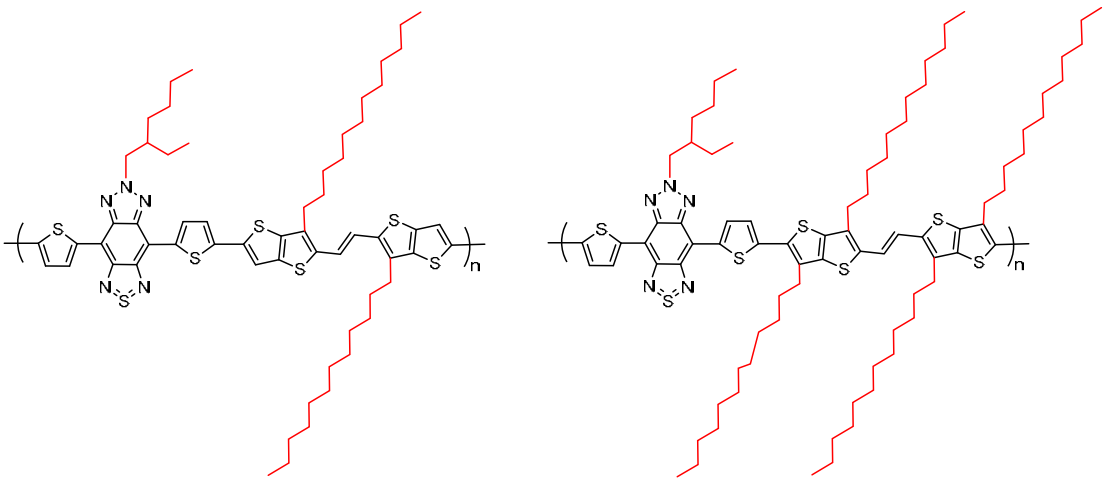
the randomly located π-π stacked regions had the alignment of C≡C−C≡C units necessary for the cross-linking. Due to the amorphousness, PDET films could be cross-linked by both UV irradiation and thermal annealing. Raman spectroscopy suggested that UV-irradiated PDET film was likely to form cross-links with C=C−C≡C (i.e., PDA-like) structure, while thermally annealed PDET and PDETT films exhibited signs of cross-linking via formation of C=C−C=C units. However, due to the low level of cross-linking degree, the formed cross-links were not expected to be truly polymeric. Cross-linked PDET films lost the charge transport properties due to the depletion of the interchain π-overlap pathways. On the other hand, despite the negative effect of the cross-linking site on the conjugation of the polymer backbone, thermally annealed PDETT film exhibited improved μ_h. These results suggest that thermal annealing facilitated growth of crystalline domains (GIWAXS), and the simultaneously formed cross-links fixed the crystallites. Thus, poly(arylenebutadiynylene)s with rigid backbone and high crystallinity could benefit from low-degree cross-linking.

In both polymers, cross-links were isolated and small, so that the effect of the conjugated backbone of the cross-links (i.e., C=C−C≡C or C=C−C=C) on the overall charge transport was assumed to be minimal. To differentiate this impact from the advantageous effect of thermal annealing, other poly(arylenebutadiynylene)s that can undergo high-extent cross-linking by UV irradiation alone must be studied.

Chapter 5

Conclusion and Future Outlook

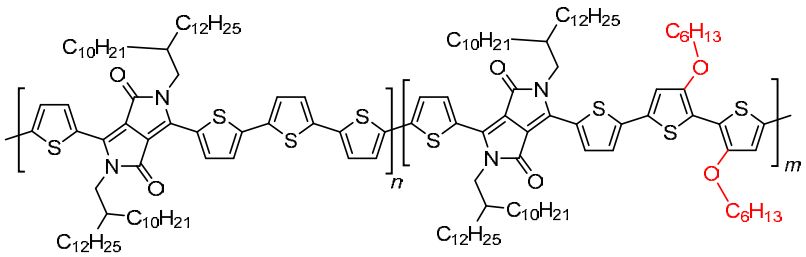
Thanks to the versatility of synthesis and solution-processability, as an alternative to Si-based semiconductors, conjugated polymers have grown into a class of promising materials for OFET applications. Chemical structure of a semiconducting polymer strongly affects its optoelectronic and film-forming properties. These in turn determine the charge transport characteristics of the polymer film. Therefore, matching of optimal acceptor-donor pairs proved to be an effective tool to design high-performance polymers. Given the large set of building blocks that has been developed over the past two decades, fine-tuning of the polymer backbone has now become essential to further improve the OFET performances. An extensive review of the literature showed that the most impactful strategy to optimize the polymer structure is the control of donor/acceptor ratio, heteroatom substitution, side group engineering, backbone planarity tuning, and random copolymerization. Based on the currently accepted understanding of the structure-property relationship in semiconducting polymers, this thesis demonstrated further development of novel polymers for OFET applications. Further recommendations and outlook for possible follow-up research are briefly provided in this chapter.



Scheme 5.1. Examples of PTBZ-DTTE polymers with alternative side group placements.

Firstly, a novel PTBZ-DTTE polymer was designed by introducing the more π-extended planarizing DTTE unit into the backbone (as compared to PTBZ-DTE). Based on the main conjugated backbone, a series of five polymers were prepared by side-group engineering. It was shown that by merely changing the positions of alkyl substituents, molecular packing orientation and film crystallinity can be deliberately controlled. All of the changes were supported by the theoretical calculations of the backbone planarity of the polymers. Thus, a link between the chemical structure of the PTBZ-DTTE polymers and their OFET properties was established. These findings can be implemented for further development of other TBZ-based polymers for OFET applications. For example, a shorter alkyl group on the TBZ unit and longer ones at the DTTE unit can be utilized (Scheme 5.1). Other later works have shown that shorter alkyl chains on the TBZ unit gave much tighter molecular packings.[51] In addition, high-performance polymers of other building blocks (e.g., DPP, NDI, IID) all contain

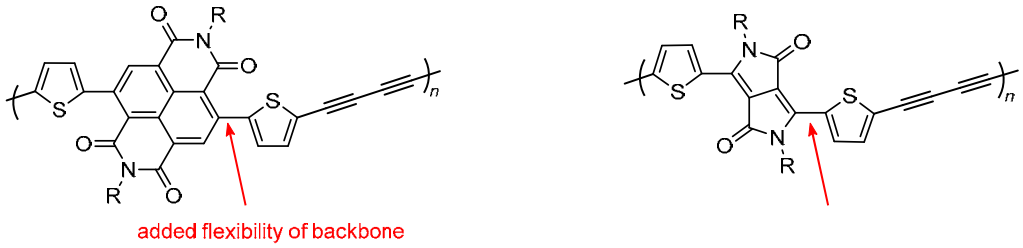
alkyl substituents on both sides of their conjugated backbones.[10,32,38] Such an approach should give much better control over the π-π stacking of the polymer chains.[63] Notably, availability of several alkyl-substitution positions in DTTE units opens up new prospects for further optimizations.



Scheme 5.2. Structure of random copolymers with longer alkoxy groups for better solubility.

Next, incorporation of electron-donating methoxy groups into a well-studied PDPP-4T polymer was studied by applying random copolymerization approach. At a loading ratio of 25 mol%, the resulting copolymer showed a slightly better OFET performance than the original polymer (depending on the film fabrication process). Obvious differences started to be observed at the higher loadings, and μ_h was improved when the methoxy-substituted monomer unit increased from 50 to 100 mol%. However, due to their limited M_n, it was suggested to compare these random copolymers separately from the high-M_n ones (i.e., 0 and 25 mol%). Loss of solubility could be caused by high backbone planarity induced by the "conformational lock" effect of the methoxy groups. Therefore, this design could be improved by using longer alkoxy

groups (Scheme 5.2).[75,78]



Scheme 5.3. Examples of possible robust poly(arylenebutadiynylene)s.

Finally, in-film cross-linking of two poly(arylenebutadiynylene)s were demonstrated. Straight backbone of PDETT allowed to observe the necessary alignment of the cross-linking units in the polymer films. However, due to the high re-organization energy necessary for the coupling reactions, the polymer could undergo cross-linking only under thermal annealing conditions. On the other hand, PDET could undergo cross-linking by UV irradiation at the randomly π-π stacked sites due to the amorphousness of the films. This work was the first study reporting the effect of in-film 1,4-addition cross-linking of poly(arylenebutadiynylene)s on their charge transport properties. The obtained results can be used to design more robust poly(arylenebutadiynylene)s for OFET applications. In addition, these findings can help to better understand performances of other devices based on this class of polymers. In the work, however, it was not possible to resolve the thermal annealing effect from that of the cross-linking in PDETT. Therefore, to elucidate on this matter, new polymers

with straight but less rigid backbones should be synthesized to achieve cross-linking by UV irradiation only (Scheme 5.3). For example, the dihedral angles in NDI-T and DPP-T moieties can serve as a source of the necessary flexibility of the backbone.[71,72]

References

[1] Heeger, A. J. Semiconducting Polymers: The Third Generation. *Chem. Soc. Rev.* **2010**, *39*, 2354–2371. https://doi.org/10.1039/b914956m.

[2] Wang, C.; Dong, H.; Hu, W.; Liu, Y.; Zhu, D. Semiconducting π-Conjugated Systems in Field-Effect Transistors: A Material Odyssey of Organic Electronics. *Chem. Rev.* **2012**, *112*, 2208–2267. https://doi.org/10.1021/cr100380z.

[3] Yang, J.; Zhao, Z.; Wang, S.; Guo, Y.; Liu, Y. Insight into High-Performance Conjugated Polymers for Organic Field-Effect Transistors. *Chem* **2018**, *4*, 2748–2785. https://doi.org/10.1016/j.chempr.2018.08.005.

[4] Gelinck, G.; Heremans, P.; Nomoto, K.; Anthopoulos, T. D. Organic Transistors in Optical Displays and Microelectronic Applications. *Adv. Mater.* **2010**, *22*, 3778–3798. https://doi.org/10.1002/adma.200903559.

[5] Diao, Y.; Shaw, L.; Bao, Z.; Mannsfeld, S. C. B. Morphology Control Strategies for Solution-Processed Organic Semiconductor Thin Films. *Energy Environ. Sci.* **2014**, *7*, 2145–2159. https://doi.org/10.1039/c4ee00688g.

[6] Coropceanu, V.; Cornil, J.; da Silva Filho, D. A.; Oliver, Y.; Silbey, R.; Bredas, J.-L. Charge Transport in Organic Semiconductors. *Chem. Rev.* **2007**, *107*, 926–952. https://doi.org/10.1021/cr050140x.

[7] Bässler, H.; Köhler, A. Charge Transport in Organic Semiconductors. *Top. Curr. Chem.* **2012**, *312*, 1–65. https://doi.org/10.1007/128_2011_218.

[8] Dong, H.; Fu, X.; Liu, J.; Wang, Z.; Hu, W. 25th Anniversary Article: Key Points for High-Mobility Organic Field-Effect Transistors. *Adv. Mater.* **2013**, *25*, 6158–6183. https://doi.org/10.1002/adma.201302514.

[9] Li, J.; Zhao, Y.; Tan, H. S.; Guo, Y.; Di, C. A.; Yu, G.; Liu, Y.; Lin, M.; Lim, S. H.; Zhou, Y.; Su, H.; Ong, B. S. A Stable Solution-Processed Polymer Semiconductor with Record High-Mobility for Printed Transistors. *Sci. Rep.* **2012**, *2*, 754. https://doi.org/10.1038/srep00754.

[10] Kang, I.; Yun, H.-J.; Chung, D. S.; Kwon, S.-K.; Kim, Y.-H. Record High Hole Mobility in Polymer Semiconductors via Side-Chain Engineering. *J. Am. Chem. Soc.* **2013**, *135*, 14896–14899. https://doi.org/10.1021/ja405112s.

[11] Back, J. Y.; Yu, H.; Song, I.; Kang, I.; Ahn, H.; Shin, T. J.; Kwon, S.-K.; Oh, J. H.; Kim, Y.-H. Investigation of Structure-Property Relationships in Diketopyrrolopyrrole-Based Polymer Semiconductors via Side-Chain Engineering. *Chem. Mater.* **2015**, *27*, 1732–1739. https://doi.org/10.1021/cm504545e.

[12] Shirakawa, H.; Louis, E. J.; MacDiarmid, A. G.; Chiang, C. K.; Heeger, A. J.

Synthesis of Electrically Conducting Organic Polymers: Halogen Derivatives of Polyacetylene, $(CH)_x$. *J. Chem. Soc. Chem. Commun.* **1977**, 578–580. https://doi.org/10.1039/c39770000578.

[13] Saxman, A. M.; Liepins, R.; Aldissi, M. Polyacetylene: Its Synthesis, Doping and Structure. *Prog. Polym. Sci.* **1985**, *11*, 57–89. https://doi.org/10.1016/0079-6700(85)90008-5.

[14] MacDiarmid, A. G.; Heeger, A. J. Organic Metals and Semiconductors: The Chemistry of Polyacetylene, $(CH)_x$, and Its Derivatives. *Synth. Met.* **1980**, *1*, 101–118. https://doi.org/10.1016/0379-6779(80)90002-8.

[15] Druy, M. A.; Tsang, C.-H.; Brown, N.; Heeger, A. J.; MacDiarmid, A. G. Tensile Properties and Partial Alignment of Polyacetylene, $(CH)_x$, Films. *J. Polym. Sci. Polym. Phys. Ed.* **1980**, *18*, 429–441. https://doi.org/10.1002/pol.1980.180180303.

[16] Ebisawa, F.; Kurokawa, T.; Nara, S. Electrical Properties of Polyacetylene/Polysiloxane Interface. *J. Appl. Phys.* **1983**, *54*, 3255–3259. https://doi.org/10.1063/1.332488.

[17] Tsumura, A.; Koezuka, H.; Ando, T. Macromolecular Electronic Device: Field-Effect Transistor with a Polythiophene Thin Film. *Appl. Phys. Lett.* **1986**, *49*, 1210–1212. https://doi.org/10.1063/1.97417.

[18] Assadi, A.; Svensson, C.; Willander, M.; Inganas, O. Field-effect Mobility of Poly(3-hexylthiophene). *Appl. Phys. Lett.* **1988**, *53*, 195–197. https://doi.org/10.1063/1.100171.

[19] Heeney, M.; Bailey, C.; Genevicius, K.; Shkunov, M.; Sparrowe, D.; Tierney, S.; McCulloch, I. Stable Polythiophene Semiconductors Incorporating Thieno[2,3-*b*]thiophene. *J. Am. Chem. Soc.* **2005**, *127*, 1078–1079. https://doi.org/10.1021/ja043112p.

[20] McCulloch, I.; Heeney, M.; Bailey, C.; Genevicius, K.; MacDonald, I.; Shkunov, M.; Sparrowe, D.; Tierney, S.; Wagner, R.; Zhang, W.; Chabinyc, M. L.; Kline, R. J.; McGehee, M. D.; Toney, M. F. Liquid-Crystalline Semiconducting Polymers with High Charge-Carrier Mobility. *Nat. Mater.* **2006**, *5*, 328–333. https://doi.org/10.1038/nmat1612.

[21] Ong, B. S.; Wu, Y.; Liu, P.; Gardner, S. High-Performance Semiconducting Polythiophenes for Organic Thin-Film Transistors. *J. Am. Chem. Soc.* **2004**, *126*, 3378–3379. https://doi.org/10.1021/ja039772w.

[22] Rieger, B. R.; Beckmann, D.; Pisula, W.; Steffen, W.; Kastler, M.; Müllen, K. Rational Optimization of Benzo[2,1-b;3,4-b']dithiophene-Containing Polymers for Organic Field-Effect Transistors. *Adv. Mater.* **2010**, *22*, 83–86. https://doi.org/10.1002/adma.200901286.

[23] Yang, C.; Cho, S.; Chiechi, R. C.; Walker, W.; Coates, N. E.; Moses, D.; Heeger, A. J.; Wudl, F. Visible-Near Infrared Absorbing Dithienylcyclopentadienone-Thiophene Copolymers for Organic Thin-Film Transistors. *J. Am. Chem. Soc.* **2008**, *130*, 16524–16526. https://doi.org/10.1021/ja806784e.

[24] Li, Y.; Singh, S. P.; Sonar, P. A High Mobility P-Type DPP-Thieno[3,2-*b*]Thiophene Copolymer for Organic Thin-Film Transistors. *Adv. Mater.* **2010**, *22*, 4862–4866. https://doi.org/10.1002/adma.201002313.

[25] Yi, Z.; Ma, L.; Chen, B.; Chen, D.; Chen, X.; Qin, J.; Zhan, X.; Liu, Y.; Ong, W. J.; Li, J. Effect of the Longer β-Unsubstituted Oligothiophene Unit (6T and 7T) on the Organic Thin-Film Transistor Performances of Diketopyrrolopyrrole- Oliogothiophene Copolymers. *Chem. Mater.* **2013**, *25*, 4290–4296. https://doi.org/10.1021/cm402381w.

[26] Chen, Z.; Lee, M. J.; Shahid Ashraf, R.; Gu, Y.; Albert-Seifried, S.; Meedom Nielsen, M.; Schroeder, B.; Anthopoulos, T. D.; Heeney, M.; McCulloch, I.; Sirringhaus, H. High-Performance Ambipolar Diketopyrrolopyrrole-Thieno[3,2-*b*]thiophene Copolymer Field-Effect Transistors with Balanced Hole and Electron Mobilities. *Adv. Mater.* **2012**, *24*, 647–652. https://doi.org/10.1002/adma.201102786.

[27] Park, J. H.; Jung, E. H.; Jung, J. W.; Jo, W. H. A Fluorinated Phenylene Unit as a Building Block for High-Performance n-Type Semiconducting Polymer. *Adv. Mater.* **2013**, *25*, 2583–2588. https://doi.org/10.1002/adma.201205320.

[28] Sun, B.; Hong, W.; Yan, Z.; Aziz, H.; Li, Y. Record High Electron Mobility of 6.3 $cm^2 V^{-1} s^{-1}$ Achieved for Polymer Semiconductors Using a New Building Block. *Adv. Mater.* **2014**, *26*, 2636–2642. https://doi.org/10.1002/adma.201305981.

[29] Gao, Y.; Zhang, X.; Tian, H.; Zhang, J.; Yan, D.; Geng, Y.; Wang, F. High Mobility Ambipolar Diketopyrrolopyrrole-Based Conjugated Polymer Synthesized Via Direct Arylation Polycondensation. *Adv. Mater.* **2015**, *27*, 6753–6759. https://doi.org/10.1002/adma.201502896.

[30] Lei, T.; Cao, Y.; Zhou, X.; Peng, Y.; Bian, J.; Pei, J. Systematic Investigation of Isoindigo-Based Polymeric Field-Effect Transistors: Design Strategy and Impact of Polymer Symmetry and Backbone Curvature. *Chem. Mater.* **2012**, *24*, 1762–1770. https://doi.org/10.1021/cm300117x.

[31] Lei, T.; Dou, J.-H.; Pei, J. Influence of Alkyl Chain Branching Positions on the Hole Mobilities of Polymer Thin-Film Transistors. *Adv. Mater.* **2012**, *24*, 6457–6461. https://doi.org/10.1002/adma.201202689.

[32] Kim, G.; Kang, S.-J.; Dutta, G. K.; Han, Y.-K.; Shin, T. J.; Noh, Y.-Y.; Yang,

C. A Thienoisoindigo-Naphthalene Polymer with Ultrahigh Mobility of 14.4 $cm^2/V \cdot s$ That Substantially Exceeds Benchmark Values for Amorphous Silicon Semiconductors. *J. Am. Chem. Soc.* **2014**, *136*, 9477–9483. https://doi.org/10.1021/ja504537v.

[33] Huang, J.; Mao, Z.; Chen, Z.; Gao, D.; Wei, C.; Zhang, W.; Yu, G. Diazaisoindigo-Based Polymers with High-Performance Charge-Transport Properties: From Computational Screening to Experimental Characterization. *Chem. Mater.* **2016**, *28*, 2209–2218. https://doi.org/10.1021/acs.chemmater.6b00154.

[34] Yan, H.; Chen, Z.; Zheng, Y.; Newman, C.; Quinn, J. R.; Dotz, F.; Kastler, M.; Facchetti, A. A High-Mobility Electron-Transporting Polymer for Printed Transistors. *Nature* **2009**, *457*, 679–686. https://doi.org/10.1038/nature07727.

[35] Kang, B.; Kim, R.; Lee, S. B.; Kwon, S.-K.; Kim, Y.-H.; Cho, K. Side-Chain-Induced Rigid Backbone Organization of Polymer Semiconductors through Semifluoroalkyl Side Chains. *J. Am. Chem. Soc.* **2016**, *138*, 3679–3686. https://doi.org/10.1021/jacs.5b10445.

[36] Lee, W.; Lee, C.; Yu, H.; Kim, D.-J.; Wang, C.; Woo, H. Y.; Oh, J. H.; Kim, B. J. Side Chain Optimization of Naphthalenediimide-Bithiophene-Based Polymers to Enhance the Electron Mobility and the Performance in All-Polymer Solar Cells. *Adv. Funct. Mater.* **2016**, *26*, 1543–1553. https://doi.org/10.1002/adfm.201504191.

[37] Guo, X.; Kim, F. S.; Seger, M. J.; Jenekhe, S. A.; Watson, M. D. Naphthalene Diimide-Based Polymer Semiconductors: Synthesis, Structure−Property Correlations, and n-Channel and Ambipolar Field-Effect Transistors. *Chem. Mater.* **2012**, *24*, 1434–1442. https://doi.org/10.1021/cm2034273.

[38] Kim, R.; Amegadze, P. S. K.; Kang, I.; Yun, H.-J.; Noh, Y.-Y.; Kwon, S.-K.; Kim, Y.-H. High-Mobility Air-Stable Naphthalene Diimide-Based Copolymer Containing Extended π-Conjugation for n-Channel Organic Field Effect Transistors. *Adv. Funct. Mater.* **2013**, *23*, 5719–5727. https://doi.org/10.1002/adfm.201301197.

[39] Sung, M. J.; Luzio, A.; Park, W.-T.; Kim, R.; Gann, E.; Maddalena, F.; Pace, G.; Xu, Y.; Natali, D.; de Falco, C.; Dang, L.; McNeill, C.R.; Caironi, M.; Noh, Y.-Y; Kim, Y.-H. High-Mobility Naphthalene Diimide and Selenophene-Vinylene-Selenophene-Based Conjugated Polymer: N-Channel Organic Field-Effect Transistors and Structure–Property Relationship. *Adv. Funct. Mater.* **2016**, *26*, 4984–4997. https://doi.org/10.1002/adfm.201601144.

[40] Dai, Y.-Z.; Ai, N.; Lu, Y.; Zheng, Y.-Q.; Dou, J.-H.; Shi, K.; Lei, T.; Wang, J.-Y.; Pei, J. Embedding Electron-Deficient Nitrogen Atoms in Polymer Backbone

towards High Performance n-Type Polymer Field-Effect Transistors. *Chem. Sci.* **2016**, *7*, 5753–5757. https://doi.org/10.1039/c6sc01380e.

[41] Lei, T.; Dou, J.-H.; Cao, X.-Y.; Wang, J.-Y.; Pei, J. A BDOPV-Based Donor-Acceptor Polymer for High-Performance n-Type and Oxygen-Doped Ambipolar Field-Effect Transistors. *Adv. Mater.* **2013**, *25*, 6589–6593. https://doi.org/10.1002/adma.201302278.

[42] Wang, Y.; Michinobu, T. Benzothiadiazole and Its π-Extended, Heteroannulated Derivatives: Useful Acceptor Building Blocks for High-Performance Donor-Acceptor Polymers in Organic Electronics. *J. Mater. Chem. C* **2016**, *4*, 6200–6214. https://doi.org/10.1039/c6tc01860b.

[43] Tsao, H. N.; Cho, D. M.; Park, I.; Hansen, M. R.; Mavrinskiy, A.; Yoon, D. Y.; Graf, R.; Pisula, W.; Spiess, H. W.; Müllen, K. Ultrahigh Mobility in Polymer Field-Effect Transistors by Design. *J. Am. Chem. Soc.* **2011**, *133*, 2605–2612. https://doi.org/10.1021/ja108861q.

[44] Lee, J.; Jang, M.; Myeon Lee, S.; Yoo, D.; Shin, T. J.; Oh, J. H.; Yang, C. Fluorinated Benzothiadiazole (BT) Groups as a Powerful Unit for High-Performance Electron-Transporting Polymers. *ACS Appl. Mater. Interfaces* **2014**, *6*, 20390–20399. https://doi.org/10.1021/am505925w.

[45] Yuen, J. D.; Fan, J.; Seifter, J.; Lim, B.; Hufschmid, R.; Heeger, A. J.; Wudl, F. High Performance Weak Donor-Acceptor Polymers in Thin Film Transistors: Effect of the Acceptor on Electronic Properties, Ambipolar Conductivity, Mobility, and Thermal Stability. *J. Am. Chem. Soc.* **2011**, *133*, 20799–20807. https://doi.org/10.1021/ja205566w.

[46] Yuen, J. D.; Kumar, R.; Zakhidov, D.; Seifter, J.; Lim, B.; Heeger, A. J.; Wudl, F. Ambipolarity in Benzobisthiadiazole-Based Donor-Acceptor Conjugated Polymers. *Adv. Mater.* **2011**, *23*, 3780–3785. https://doi.org/10.1002/adma.201101134.

[47] Wang, Y.; Masunaga, H.; Hikima, T.; Matsumoto, H.; Mori, T.; Michinobu, T. New Semiconducting Polymers Based on Benzobisthiadiazole Analogues: Tuning of Charge Polarity in Thin Film Transistors via Heteroatom Substitution. *Macromolecules* **2015**, *48*, 4012–4023. https://doi.org/10.1021/acs.macromol.5b00802.

[48] Wang, Y.; Hasegawa, T.; Matsumoto, H.; Mori, T.; Michinobu, T. Rational Design of High-Mobility Semicrystalline Conjugated Polymers with Tunable Charge Polarity: Beyond Benzobisthiadiazole-Based Polymers. *Adv. Funct. Mater.* **2017**, *27*, 1604608. https://doi.org/10.1002/adfm.201604608.

[49] Zhu, C.; Zhao, Z.; Chen, H.; Zheng, L.; Li, X.; Chen, J.; Sun, Y.; Liu, F.; Guo, Y.; Liu, Y. Regioregular Bis-Pyridal[2,1,3]thiadiazole-Based Semiconducting

Polymer for High-Performance Ambipolar Transistors. *J. Am. Chem. Soc.* **2017**, *139*, 17735–17738. https://doi.org/10.1021/jacs.7b10256.

[50] Wang, Y.; Hasegawa, T.; Matsumoto, H.; Mori, T; Michinobu, T. High-Performance n-Channel Organic Transistors Using High-Molecular-Weight Electron-Deficient Copolymers. *Adv. Mater.* **2018**, *30*, 1707164. https://doi.org/10.1002/adma.201707164.

[51] Wang, Y.; Hasegawa, T.; Matsumoto, H.; Michinobu, T. Significant Improvement of Unipolar N-Type Transistor Performances by Manipulating the Coplanar Backbone Conformation of Electron-Deficient Polymers via Hydrogen Bonding. *J. Am. Chem. Soc.* **2019**, *141*, 3566–3575. https://doi.org/10.1021/jacs.8b12499.

[52] Horowitz, G. Organic Field-Effect Transistors. *Adv. Mater.* **1998**, *10*, 365–377. https://doi.org/10.1002/(sici)1521-4095(199803)10:5<365::aid-adma365>3.0.co;2-u.

[53] Xu, Y.; Liu, C.; Khim, D.; Noh, Y.-Y. Development of High-Performance Printed Organic Field-Effect Transistors and Integrated Circuits. *Phys. Chem. Chem. Phys.* **2015**, *17*, 26553–26574. https://doi.org/10.1039/c4cp02413c.

[54] Sirringhaus, H.; Brown, P. J.; Friend, R. H.; Nielsen, M. M.; Bechgaard, K.; Langeveld-Voss, B. M. W.; Spiering, A. J. H.; Janssen, R. A. J.; Meijer, E. W.; Herwig, P.; de Leeuw, D. M. Two-Dimensional Charge Transport in Self-Organized, High-Mobility Conjugated Polymers. *Nature* **1999**, *401*, 685–688. https://doi.org/10.1038/44359.

[55] Sirringhaus, H. 25th Anniversary Article: Organic Field-Effect Transistors: The Path beyond Amorphous Silicon. *Adv. Mater.* **2014**, *26*, 1319–1335. https://doi.org/10.1002/adma.201304346.

[56] Li, Y.; Sonar, P.; Singh, S. P.; Soh, M. S.; Van Meurs, M.; Tan, J. Annealing-Free High-Mobility Diketopyrrolopyrrole-Quaterthiophene Copolymer for Solution-Processed Organic Thin Film Transistors. *J. Am. Chem. Soc.* **2011**, *133*, 2198–2204. https://doi.org/10.1021/ja1085996.

[57] Yi, Z.; Sun, X.; Zhao, Y.; Guo, Y.; Chen, X.; Qin, J.; Yu, G.; Liu, Y. Diketopyrrolopyrrole-Based π-Conjugated Copolymer Containing β-Unsubstituted Quintetthiophene Unit: A Promising Material Exhibiting High Hole-Mobility for Organic Thin-Film Transistors. *Chem. Mater.* **2012**, *24*, 4350–4356. https://doi.org/10.1021/cm302341m.

[58] Shi, Y.; Guo, H.; Qin, M.; Zhao, J.; Wang, Y.; Wang, H.; Wang, Y.; Facchetti, A.; Lu, X.; Guo, X. Thiazole Imide-Based All-Acceptor Homopolymer: Achieving High-Performance Unipolar Electron Transport in Organic Thin-Film Transistors. *Adv. Mater.* **2018**, *30*, 1705745.

https://doi.org/10.1002/adma.201705745.

[59] Liu, Q.; Wang, Y.; Ren, Y.; Kohara, A.; Matsumoto, H.; Chen, Y.; Manzhos, S.; Feron, K.; Bottle, S. E.; Bell, J.; Zhou, Y.; Michinobu, T.; Sonar, P. Diketopyrrolopyrrole-Based Dual-Acceptor Copolymers to Realize Tunable Charge Carrier Polarity of Organic Field-Effect Transistors and High-Performance Nonvolatile Ambipolar Flash Memories. *ACS Appl. Electron. Mater.* **2020**, *2*, 1609–1618. https://doi.org/10.1021/acsaelm.0c00169.

[60] Wang, Y.; Kim, S. W.; Lee, J.; Matsumoto, H.; Kim, B. J.; Michinobu, T. Dual Imide-Functionalized Unit-Based Regioregular D-A_1-D-A_2 Polymers for Efficient Unipolar n-Channel Organic Transistors and All-Polymer Solar Cells. *ACS Appl. Mater. Interfaces* **2019**, *11*, 22583–22594. https://doi.org/10.1021/acsami.9b05537.

[61] Li, W.; Lee, T.; Oh, S. J.; Kagan, C. R. Diketopyrrolopyrrole-Based π-Bridged Donor-Acceptor Polymer for Photovoltaic Applications. *ACS Appl. Mater. Interfaces* **2011**, *3*, 3874–3883. https://doi.org/10.1021/am200720e.

[62] Ha, J. S.; Kim, K. H.; Choi, D. H. 2,5-Bis(2-octyldodecyl)pyrrolo[3,4-*c*]pyrrole-1,4-(2H,5H)-dione-Based Donor–Acceptor Alternating Copolymer Bearing 5,5'-Di(thiophen-2-yl)-2,2'-biselenophene Exhibiting 1.5 $cm^2 V^{-1} s^{-1}$ Hole Mobility in Thin-Film Transistors. *J. Am. Chem. Soc.* **2011**, *133*, 10364–10367.

[63] Osaka, I.; Takimiya, K. Backbone Orientation in Semiconducting Polymers. *Polymer* **2015**, *59*, A1–A15. https://doi.org/10.1016/j.polymer.2014.12.066.

[64] Osaka, I.; Houchin, Y.; Yamashita, M.; Kakara, T.; Takemura, N.; Koganezawa, T.; Takimiya, K. Contrasting Effect of Alkylation on the Ordering Structure in Isomeric Naphthodithiophene-Based Polymers. *Macromolecules* **2014**, *47*, 3502–3510. https://doi.org/10.1021/ma402518d.

[65] Osaka, I.; Saito, M.; Koganezawa, T.; Takimiya, K. Thiophene-Thiazolothiazole Copolymers: Significant Impact of Side Chain Composition on Backbone Orientation and Solar Cell Performances. *Adv. Mater.* **2014**, *26*, 331–338. https://doi.org/10.1002/adma.201303059.

[66] Noriega, R.; Rivnay, J.; Vandewal, K.; Koch, F. P. V.; Stingelin, N.; Smith, P.; Toney, M. F.; Salleo, A. A General Relationship between Disorder, Aggregation and Charge Transport in Conjugated Polymers. *Nat. Mater.* **2013**, *12*, 1038–1044. https://doi.org/10.1038/nmat3722.

[67] Chen, M. S.; Lee, O. P.; Niskala, J. R.; Yiu, A. T.; Tassone, C. J.; Schmidt, K.; Beaujuge, P. M.; Onishi, S. S.; Toney, M. F.; Zettl, A.; Frechet, J. M. J. Enhanced Solid-State Order and Field-Effect Hole Mobility through Control of Nanoscale Polymer Aggregation. *J. Am. Chem. Soc.* **2013**, *135*, 19229–19236. https://doi.org/10.1021/ja4088665.

[68] Chen, H.; Guo, Y.; Yu, G.; Zhao, Y.; Zhang, J.; Gao, D.; Liu, H.; Liu, Y. Highly π-Extended Copolymers with Diketopyrrolopyrrole Moieties for High-Performance Field-Effect Transistors. *Adv. Mater.* **2012**, *24*, 4618–4622. https://doi.org/10.1002/adma.201201318.

[69] Mei, J.; Bao, Z. Side Chain Engineering in Solution-Processable Conjugated Polymers. *Chem. Mater.* **2014**, *26*, 604–615. https://doi.org/10.1021/cm4020805.

[70] Song, K. W.; Song, H. J.; Lee, T. H.; Heo, S. W.; Moon, D. K. An Effect on the Side Chain Position of D-π-A-Type Conjugated Polymers with sp^2-Hybridized Orbitals for Organic Photovoltaics. *Polym. Chem.* **2013**, *4*, 3225–3235. https://doi.org/10.1039/c3py00195d.

[71] Nielsen, C. B.; Turbiez, M.; McCulloch, I. Recent Advances in the Development of Semiconducting DPP-Containing Polymers for Transistor Applications. *Adv. Mater.* **2013**, *25*, 1859–1880. https://doi.org/10.1002/adma.201201795.

[72] Ning, L.; Han, G.; Yi, Y. Intra-Chain and Inter-Chain Synergistic Effect Gives Rise to High Electron Mobilities for Naphthalenediimide Based Copolymers. *J. Mater. Chem. C* **2020**, *8*, 16527–16532. https://doi.org/10.1039/d0tc03715j.

[73] Chen, L.; Zhao, K.; Chi, S.; Liu, J.; Yu, X.; Han, Y. Improving Fiber Alignment by Increasing the Planar Conformation of Isoindigo-Based Conjugated Polymers. *Mater. Chem. Front.* **2017**, *1*, 286–293. https://doi.org/10.1039/c6qm00024j.

[74] Otep, S.; Wang, Y.; Kohara, A.; Matsumoto, H.; Mori, T.; Michinobu, T. Tuning Backbone Planarity in Thiadiazolobenzotriazole–Bis(Thienothiophenyl)Ethylene Copolymers for Organic Field-Effect Transistors. *ACS Appl. Polym. Mater.* **2019**, *1*, 2302–2312. https://doi.org/10.1021/acsapm.9b00329.

[75] Huang, H.; Yang, L.; Facchetti, A.; Marks, T. J. Organic and Polymeric Semiconductors Enhanced by Noncovalent Conformational Locks. *Chem. Rev.* **2017**, *117*, 10291–10318. https://doi.org/10.1021/acs.chemrev.7b00084.

[76] Guo, X.; Quinn, J.; Chen, Z.; Usta, H.; Zheng, Y.; Xia, Y.; Hennek, J. W.; Ortiz, R. P.; Marks, T. J.; Facchetti, A. Dialkoxybithiazole: A New Building Block for Head-to-Head Polymer Semiconductors. *J. Am. Chem. Soc.* **2013**, *135*, 1986–1996. https://doi.org/10.1021/ja3120532.

[77] Cheng, Y.; Qi, Y.; Tang, Y.; Zheng, C.; Wan, Y.; Huang, W.; Chen, R. Controlling Intramolecular Conformation through Nonbonding Interaction for Soft-Conjugated Materials: Molecular Design and Optoelectronic Properties. *J. Phys. Chem. Lett.* **2016**, *7*, 3609–3615.

https://doi.org/10.1021/acs.jpclett.6b01695.

[78] Kim, H. G.; Kang, B.; Ko, H.; Lee, J.; Shin, J.; Cho, K. Synthetic Tailoring of Solid-State Order in Diketopyrrolopyrrole-Based Copolymers via Intramolecular Noncovalent Interactions. *Chem. Mater.* **2015**, *27*, 829–838. https://doi.org/10.1021/cm503864u.

[79] Meille, S. V.; Farina, A.; Bezziccheri, F.; Gallazzi, M. C. The Influence of Alkoxy Side Chains on the Conformational Flexibility of Oligo- and Polythiophenes. *Adv. Mater.* **1994**, *6*, 848–851. https://doi.org/10.1002/adma.19940061109.

[80] Sakamoto, Y.; Komatsu, S.; Suzuki, T. Tetradecafluorosexithiophene: The First Perfluorinated Oligothiophene. *J. Am. Chem. Soc.* **2001**, *123*, 4643–4644. https://doi.org/10.1021/ja015712j.

[81] Zhang, W.; Yu, G. Rational Design of Diarylethylene-Based Polymeric Semiconductors for High-Performance Organic Field-Effect Transistors. *J. Polym. Sci. Part A Polym. Chem.* **2017**, *55*, 585–603. https://doi.org/10.1002/pola.28391.

[82] Gao, D.; Tian, K.; Zhang, W.; Huang, J.; Chen, Z.; Mao, Z.; Yu, G. Approaching High Charge Carrier Mobility by Alkylating Both Donor and Acceptor Units at the Optimized Position in Conjugated Polymers. *Polym. Chem.* **2016**, *7*, 4046–4053. https://doi.org/10.1039/c6py00469e.

[83] Kim, J.; Han, A.-R.; Hong, J.; Kim, G.; Lee, J.; Shin, T. J.; Oh, J. H.; Yang, C. Ambipolar Semiconducting Polymers with π-Spacer Linked Bis-Benzothiadiazole Blocks as Strong Accepting Units. *Chem. Mater.* **2014**, *26*, 4933–4942. https://doi.org/10.1021/cm500800u.

[84] Du, Y.; Yao, H.; Galuska, L.; Ge, F.; Wang, X.; Lu, H.; Zhang, G.; Gu, X.; Qiu, L. Side-Chain Engineering to Optimize the Charge Transport Properties of Isoindigo-Based Random Terpolymers for High-Performance Organic Field-Effect Transistors. *Macromolecules* **2019**, *52*, 4765–4775. https://doi.org/10.1021/acs.macromol.9b00474.

[85] Nair, V. S.; Sun, J.; Qi, P.; Yang, S.; Liu, Z.; Zhang, D.; Ajayaghosh, A. Conjugated Random Donor-Acceptor Copolymers of [1]Benzothieno[3,2-*b*]benzothiophene and Diketopyrrolopyrrole Units for High Performance Polymeric Semiconductor Applications. *Macromolecules* **2016**, *49*, 6334–6342. https://doi.org/10.1021/acs.macromol.6b00954.

[86] Ohnishi, I.; Hashimoto, K.; Tajima, K. Synthesis of Diketopyrrolopyrrole-Based Polymers with Polydimethylsiloxane Side Chains and Their Application in Organic Field-Effect Transistors. *R. Soc. Open Sci.* **2018**, *5*, 172025. https://doi.org/10.1098/rsos.172025.

[87] Yun, H.-J.; Cho, J.; Chung, D. S.; Kim, Y.-H.; Kwon, S.-K. Comparative Studies on the Relations between Composition Ratio and Charge Transport of Diketopyrrolopyrrole-Based Random Copolymers. *Macromolecules* **2014**, *47*, 7030–7035. https://doi.org/10.1021/ma501980m.

[88] Gasperini, A.; Sivula, K. Effects of Molecular Weight on Microstructure and Carrier Transport in a Semicrystalline Poly(thieno)thiophene. *Macromolecules* **2013**, *46*, 9349–9358. https://doi.org/10.1021/ma402027v.

[89] Gasperini, A.; Jeanbourquin, X. A.; Sivula, K. Effect of Molecular Weight in Diketopyrrolopyrrole-Based Polymers in Transistor and Photovoltaic Applications. *J. Polym. Sci. Part B Polym. Phys.* **2016**, *54*, 2245–2253. https://doi.org/10.1002/polb.24135.

[90] Kwon, J.; Takeda, Y.; Fukuda, K.; Cho, K.; Tokito, S.; Jung, S. Three-Dimensional, Inkjet-Printed Organic Transistors and Integrated Circuits with 100% Yield, High Uniformity, and Long-Term Stability. *ACS Nano* **2016**, *10*, 10324–10330. https://doi.org/10.1021/acsnano.6b06041.

[91] Shin, J.; Hong, T. R.; Lee, T. W.; Kim, A.; Kim, Y. H.; Cho, M. J.; Choi, D. H. Template-Guided Solution-Shearing Method for Enhanced Charge Carrier Mobility in Diketopyrrolopyrrole-Based Polymer Field-Effect Transistors. *Adv. Mater.* **2014**, *26*, 6031–6035. https://doi.org/10.1002/adma.201401179.

[92] Kim, G. W.; Kwon, E. H.; Kim, M.; Park, Y. D. Uniform and Reliable Dip-Coated Conjugated Polymers for Organic Transistors as Obtained by Solvent Vapor Annealing. *J. Phys. Chem. C* **2019**, *123*, 23255–23263. https://doi.org/10.1021/acs.jpcc.9b06996.

[93] Ito, Y.; Virkar, A. A.; Mannsfeld, S.; Joon, H. O.; Toney, M.; Locklin, J.; Bao, Z. Crystalline Ultrasmooth Self-Assembled Monolayers of Alkylsilanes for Organic Field-Effect Transistors. *J. Am. Chem. Soc.* **2009**, *131*, 9396–9404. https://doi.org/10.1021/ja9029957.

[94] Park, W.-T.; Kim, G.; Yang, C.; Liu, C.; Noh, Y.-Y. Effect of Donor Molecular Structure and Gate Dielectric on Charge-Transporting Characteristics for Isoindigo-Based Donor–Acceptor Conjugated Polymers. *Adv. Funct. Mater.* **2016**, *26*, 4695–4703. https://doi.org/10.1002/adfm.201504908.

[95] Wang, Y.; Huang, X.; Li, T.; Li, L.; Guo, X.; Jiang, P. Polymer-Based Gate Dielectrics for Organic Field-Effect Transistors. *Chem. Mater.* **2019**, *31*, 2212–2240. https://doi.org/10.1021/acs.chemmater.8b03904.

[96] Joshi, S.; Grigorian, S.; Pietsch, U.; Pingel, P.; Zen, A.; Neher, D.; Scherf, U. Thickness Dependence of the Crystalline Structure and Hole Mobility in Thin Films of Low Molecular Weight Poly(3-hexylthiophene). *Macromolecules* **2008**, *41*, 6800–6808. https://doi.org/10.1021/ma702802x.

[97] Duong, D. T.; Toney, M. F.; Salleo, A. Role of Confinement and Aggregation in Charge Transport in Semicrystalline Polythiophene Thin Films. *Phys. Rev. B* **2012**, *86*, 205205. https://doi.org/10.1103/PhysRevB.86.205205.

[98] Rivnay, J.; Steyrleuthner, R.; Jimison, L. H.; Casadei, A.; Chen, Z.; Toney, M. F.; Facchetti, A.; Neher, D.; Salleo, A. Drastic Control of Texture in a High Performance n-Type Polymeric Semiconductor and Implications for Charge Transport. *Macromolecules* **2011**, *44*, 5246–5255. https://doi.org/10.1021/ma200864s.

[99] Jang, M.; Huh, Y.-I.; Chang, M. Effects of Solvent Vapor Annealing on Morphology and Charge Transport of Poly(3-hexylthiophene) (P3HT) Films Incorporated with Preformed P3HT Nanowires. *Polymers* **2020**, 12, 1188. https://doi.org/10.3390/polym12051188.

[100] Park, M. S.; Kim, F. S. Synergistic Effects of Processing Additives and Thermal Annealing on Nanomorphology and Hole Mobility of Poly(3-hexylthiophene) Thin Films. *Polymers* **2019**, *11*, 112. https://doi.org/10.3390/polym11010112.

[101] Luo, H.; Yu, C.; Liu, Z.; Zhang, G.; Geng, H.; Yi, Y.; Broch, K.; Hu, Y.; Sadhanala, A.; Jiang, L.; Qi, P.; Cai, Z.; Sirringhaus, H.; Zhang, D. Remarkable Enhancement of Charge Carrier Mobility of Conjugated Polymer Field-Effect Transistors upon Incorporating an Ionic Additive. *Sci. Adv.* **2016**, *2*, e1600076. https://doi.org/10.1126/sciadv.1600076.

[102] Yao, Y.; Dong, H.; Liu, F.; Russell, T. P.; Hu, W. Approaching Intra- and Interchain Charge Transport of Conjugated Polymers Facilely by Topochemical Polymerized Single Crystals. *Adv. Mater.* **2017**, *2*, 1701251. https://doi.org/10.1002/adma.201701251.

[103] Lin, F.-J.; Tao, Y.-T. Aligning Poly[1,6-di-(N-carbazolyl)-2,4-hexadiyne] Crystalline Fibers as Conducting Channels for Transistor Applications. *J. Chin. Chem. Soc.* **2019**, *66*, 1227–1235. https://doi.org/10.1002/jccs.201900275.

[104] Lin, F.-J.; Yang, C.-W.; Chen, H.-H.; Tao, Y.-T. Alignment and Photopolymerization of Hexa-*peri*-hexabenzocoronene Derivatives Carrying Diacetylenic Side Chains for Charge-Transporting Application. *J. Am. Chem. Soc.* **2020**, *142*, 11763–11771. https://doi.org/10.1021/jacs.0c02055.

[105] Nyayachavadi, A.; Langlois, A.; Tahir, M. N.; Billet, B.; Rondeau-Gagne, S. Conjugated Polymer with Polydiacetylene Cross-Links Through Topochemical Polymerization of 1,3-Butadiyne Moieties Toward Photopatternable Thin Films. *ACS Appl. Polym. Mater.* **2019**, *1*, 1918–1924. https://doi.org/10.1021/acsapm.9b00520.

[106] Tam, T. L.; Li, H.; Lam, Y. M.; Mkasilkar, S. G.; Grimsdale, A. C. Synthesis and Characterization of [1,2,5]Chalcogenazolo[3,4-f]benzo[1,2,3]triazole and

[1,2,3]Triazolo [3,4-g]quinoxaline Derivatives. *Org. Lett*. **2011**, *13*, 4612 –4615. https://doi.org/10.1021/ol201829s.

[107] Jang, M.; Kim, J.-H.; Hwang, D.-H.; Yang, H. Controlling Conjugation and Solubility of Donor-Acceptor Semiconducting Copolymers for High-Performance Organic Field-Effect Transistors. *ACS Appl. Mater. Interfaces* **2015**, *7*, 12781–12788. https://doi.org/10.1021/acsami.5b01746.

[108] Kotowski, D.; Luzzati, S.; Bianchi, G.; Calabrese, A.; Pellegrino, A.; Po, R.; Schimperna, G.; Tacca, A. Double Acceptor D-A Copolymers Containing Benzotriazole and Benzothiadiazole Units: Chemical Tailoring Towards Efficient Photovoltaic Properties. *J. Mater. Chem. A* **2013**, *1*, 10736–10744. https://doi.org/10.1039/c3ta11698k.

[109] Irie, S.; Fuse, S.; Maitani, M. M.; Wada, Y.; Ogomi, Y.; Hayase, S.; Kaiho, T.; Masui, H.; Tanaka, H.; Takahashi, T. Rapid Synthesis of D-A'-π-A Dyes through a One-Pot Three-Component Suzuki–Miyaura Coupling and an Evaluation of their Photovoltaic Properties for Use in Dye-Sensitized Solar Cells. *Chem. Eur. J.* **2016**, *22*, 2507–2514. https://doi.org/10.1002/chem.201504277.

[110] Steckler, T. T.; Lee, M. J.; Chen, Z.; Fenwick, O.; Andersson, M. R.; Cacialli, F.; Sirringhaus, H. Multifunctional Materials for OFETs, LEFETs and NIR PLEDs. *J. Mater. Chem. C* **2014**, *2*, 5133–5141. https://doi.org/10.1039/c4tc00342j.

[111] Zhang, X.; Kohler, M.; Matzger, A. J. Alkyl-Substituted Thieno[3,2-*b*]thiophene Polymers and Their Dimeric Subunits. *Macromolecules* **2004**, *37*, 6306–6315. https://doi.org/10.1021/ma049107n.

[112] Cahiez, G.; Moyeux, A.; Gager, O.; Poizat, M. Copper-Catalyzed Decarboxylation of Aromatic Carboxylic Acids: En Route to Milder Reaction Conditions. *Adv. Synth. Catal.* **2013**, *355*, 790–796. https://doi.org/10.1002/adsc.201201018.

[113] Frisch, M.J.; Trucks, G.W.; Schlegel, H.B.; Scuseria, G.E.; Robb, M.A.; Cheeseman, J.R.; Montgomery Jr., J.A.; Vreven, T.; Kudin, K.N.; Burant, J.C.; et al. *Gaussian 09, Revision A.02;* Gaussian, Inc.: Pittsburgh, KS, USA, 2009.

[114] Nielsen, A.B.; Holder, A.J. *Gauss View 5.0, User's Reference;* Gaussian Inc.: Pittsburgh, KS, USA, 2009.

[115] McCulloch, I.; Salleo, A.; Chabinyc, M. Avoid the kinks when measuring mobility. *Science* **2016**, *352*, 1521–1522. https://doi.org/10.1126/science.aaf9062.

[116] Okachi, T.; Kashiki, T.; Ohya, K. Device Operation Mechanism of Field-Effect Transistors with High Mobility Donor-Acceptor Polymer Semiconductors. *Proc. SPIE* **2015**, *9568*, 95680I. https://doi.org/10.1117/12.2187572.

[117] Un, H.-I.; Cheng, P.; Lei, T.; Yang, C.-Y.; Wang, J.-Y.; Pei, J. Charge-Trapping-Induced Non-Ideal Behaviors in Organic Field-Effect Transistors. *Adv. Mater.* **2018**, *30*, 1800017. https://doi.org/10.1002/adma.201800017.

[118] Bittle, E. G.; Basham, J. I.; Jackson, T, N.; Jurchescu, O. D.; Gundlach, D. J. Mobility Overestimation Due to Gated Contacts in Organic Field-Effect Transistors. *Nat. Commun.* **2016**, *7*, 10908. https://doi.org/10.1038/ncomms10908.

[119] Yoo, D.; Nketia-Yawson, B.; Kang, S.-J.; Ahn, H.; Shin, T. J.; Noh, Y.-Y.; Yang, C. A Timely Synthetic Tailoring of Biaxially Extended Thienylenevinylene-Like Polymers for Systematic Investigation on Field-Effect Transistors. *Adv. Funct. Mater.* **2015**, *25*, 586–596. https://doi.org/10.1002/adfm.201403527.

[120] Li, Y.; Sonar, P.; Murphy, L.; Hong, W. High Mobility Diketopyrrolopyrrole (DPP)-Based Organic Semiconductor Materials for Organic Thin Film Transistors and Photovoltaics. *Energy Environ. Sci.* **2013**, *6*, 1684–1710. https://doi.org/10.1039/c3ee00015j.

[121] Liu, Q.; Bottle, S. E.; Sonar, P. Developments of Diketopyrrolopyrrole-Dye-Based Organic Semiconductors for a Wide Range of Applications in Electronics. *Adv. Mater.* **2020**, *32*, 1903882. https://doi.org/10.1002/adma.201903882.

[122] Kim, H. J.; Pei, M.; Ko, J. S.; Ma, M. H.; Park, G. E.; Baek, J.; Yang, H.; Cho, M. J.; Choi, D. H. Influence of Branched Alkyl Ester-Labeled Side Chains on Specific Chain Arrangement and Charge-Transport Properties of Diketopyrrolopyrrole-Based Conjugated Polymers. *ACS Appl. Mater. Interfaces* **2018**, *10*, 40681–40691. https://doi.org/10.1021/acsami.8b13292.

[123] Wang, Y.; Tan, A. T.-R.; Mori, T.; Michinobu, T. Inversion of Charge Carrier Polarity and Boosting the Mobility of Organic Semiconducting Polymers Based on Benzobisthiadiazole Derivatives by Fluorination. *J. Mater. Chem. C* **2018**, *6*, 3593–3603. https://doi.org/10.1039/c7tc04993e.

[124] Imae, I.; Tada, N.; Harima, Y. Synthesis and Properties of Donor-Acceptor-Type Polymers Comprising Alkoxy-Substituted Bithiophene Units. *J. Photopolym. Sci. Technol.* **2019**, *32*, 585–592. https://doi.org/10.2494/photopolymer.32.585.

[125] Guo, X.; Liao, Q.; Manley, E. F.; Wu, Z.; Wang, Y.; Wang, W.; Yang, T.; Shin, Y.-E.; Cheng, X.; Liang, Y.; Chen, L. X.; Baeg, K.-J.; Marks, T. J.; Guo, X. Materials Design via Optimized Intramolecular Noncovalent Interactions for High-Performance Organic Semiconductors. *Chem. Mater.* **2016**, *28*, 2449−2460. https://doi.org/10.1021/acs.chemmater.6b00850.

[126] Nielsen, C. B.; Giovannitti, A.; Sbircea, D.-T.; Bandiello, E.; Niazi, M. R.; Hanifi, D. A.; Sessolo, M.; Amassian, A.; Malliaras, G. G.; Rivnay, J.;

McCulloch, I. Molecular Design of Semiconducting Polymers for High-Performance Organic Electrochemical Transistors. *J. Am. Chem. Soc.* **2016**, *138*, 10252−10259. https://doi.org/10.1021/jacs.6b05280.

[127] Shi, S.; Liao, Q.; Tang, Y.; Guo, H.; Zhou, X.; Wang, Y.; Yang, T.; Liang, Y.; Cheng, X.; Liu, F.; Guo, X. Head-to-Head Linkage Containing Bithiophene-Based Polymeric Semiconductors for Highly Efficient Polymer Solar Cells. *Adv. Mater.* **2016**, *28*, 9969–9977. https://doi.org/10.1002/adma.201603112.

[128] Chen, J.; Yan, Z.; Tang, L.; Uddin, M.A.; Yu, J.; Zhou, X.; Yang, K.; Tang, Y.; Shin, T. J.; Woo, H. Y.; Guo, X. 1,4-Di(3-alkoxy-2-thienyl)-2,5-difluorophenylene: A Building Block Enabling High-Performance Polymer Semiconductors with Increased Open-Circuit Voltages. *Macromolecules* **2018**, *51*, 5352−5363. https://doi.org/10.1021/acs.macromol.8b00975.

[129] Hendriks, K. H.; Li, W.; Wienk, M. M.; Janssen, R. A. J. Band Gap Control in Diketopyrrolopyrrole-Based Polymer Solar Cells Using Electron Donating Side Chains. *Adv. Energy Mater.* **2013**, 3, 674–679. https://doi.org/10.1002/aenm.201200950.

[130] Cho, J.; Park, S. J.; Lee, S. M.; Ha, J. U.; Ahn, E. S.; Chang, S. T.; Kwon, S.-K.; Chung, D. S.; Kim, Y.-H. Synergetic Evolution of Diketopyrrolopyrrole-Based Polymeric Semiconductor for High Reproducibility and Performance: Random Copolymerization of Similarly Shaped Building Blocks. *Macromol. Rapid Commun.* **2016**, *37*, 2057–2063. https://doi.org/10.1002/marc.201600537.

[131] Li, H.; Liu, F.; Wang, X.; Gu, C.; Wang, P.; Fu, H. Diketopyrrolopyrrole–Thiophene–Benzothiadiazole Random Copolymers: An Effective Strategy to Adjust Thin-Film Crystallinity for Transistor and Photovoltaic Properties. *Macromolecules* **2013**, *46*, 9211–9219. https://doi.org/10.1021/ma401873s.

[132] Qi, P.; Wang, Z.; Liu, Z.; Yang, S.; Yang, Y.; Yao, J.; Zhang, G.; Zhang, D. Conjugated Donor–Acceptor Terpolymers Entailing the Pechmann Dye and Dithienyl-diketopyrrolopyrrole as Co-Electron Acceptors: Tuning HOMO/LUMO Energies and Photovoltaic Performances. *Polym. Chem.* **2016**, *7*, 3838–3847. https://doi.org/10.1039/c6py00400h.

[133] Kang, I.; An, T. K.; Hong, J.-a.; Yun, H.-J.; Kim, R.; Chung, D. S.; Park, C. E.; Kim, Y.-H.; Kwon, S.-K. Effect of Selenophene in a DPP Copolymer Incorporating a Vinyl Group for High-Performance Organic Field-Effect Transistors. *Adv. Mater.* **2013**, *25*, 524–528. https://doi.org/10.1002/adma.201202867.

[134] Choi, J.; Kim, K.-H.; Yu, H.; Lee, C.; Kang, H.; Song, I.; Kim, Y.; Oh, J. H.; Kim, B. J. Importance of Electron Transport Ability in Naphthalene Diimide-Based Polymer Acceptors for High-Performance, Additive-Free, All-Polymer

Solar Cells. *Chem. Mater.* **2015**, *27*, 5230–5237. https://doi.org/10.1021/acs.chemmater.5b01274.

[135] Giovannitti, A.; Thorley, K. J.; Nielsen, C. B.; Li, J.; Donahue, M. J.; Malliaras, G. G.; Rivnay, J.; McCulloch, I. Redox-Stability of Alkoxy-BDT Copolymers and Their Use for Organic Bioelectronic Devices. *Adv. Funct. Mater.* **2018**, *28*, 1706325. https://doi.org/10.1002/adfm.201706325.

[136] Shi, C.; Yao, Y.; Yang, Y.; Pei, Q. Regioregular Copolymers of 3-Alkoxythiophene and Their Photovoltaic Application. *J. Am. Chem. Soc.* **2006**, *128*, 8980–8986. https://doi.org/10.1021/ja061664x.

[137] Spano, F. C.; Silva, C. H- and J-Aggregate Behavior in Polymeric Semiconductors. *Annu. Rev. Phys. Chem.* **2014**, *65*, 477–500. https://doi.org/10.1146/annurev-physchem-040513-103639.

[138] Mas-Montoya, M.; Janssen, R. A. J. The Effect of H- and J-Aggregation on the Photophysical and Photovoltaic Properties of Small Thiophene–Pyridine–DPP Molecules for Bulk-Heterojunction Solar Cells. *Adv. Funct. Mater.* **2017**, *27*, 1605779. https://doi.org/10.1002/adfm.201605779.

[139] Hasegawa, T.; Ashizawa, M.; Hiyoshi, J.; Kawauchi, S.; Mei, J.; Bao, Z.; Matsumoto, H. An Ultra-Narrow Bandgap Derived from Thienoisoindigo Polymers: Structural Influence on Reducing the Bandgap and Self-Organization. *Polym. Chem.* **2016**, *7*, 1181–1190. https://doi.org/10.1039/c5py01870f.

[140] Nakabayashi, K.; Miyakawa, K.; Mori, H. Thienoisoindigo-Based Donor–Acceptor Random Copolymers: Synthesis, Characterization, and Thin Film Nanostructure Study. *Polym. Bull.* **2020**, *77*, 4011–4022. https://doi.org/10.1007/s00289-019-02956-z.

[141] Hu, L.; Qiao, W.; Han, J.; Zhou, X.; Wang, C.; Ma, D.; Wang, Z. Y.; Lie, Y. Naphthalene Diimide–Diketopyrrolopyrrole Copolymers as Non-Fullerene Acceptors for Use in Bulk-Heterojunction All-Polymer UV–NIR Photodetectors. *Polym. Chem.* **2017**, *8*, 528–536. https://doi.org/10.1039/c6py01828a.

[142] Park, S.; Lee, M. H.; Ahn, K. S.; Choi, H. H.; Shin, J.; Xu, J.; Mei, J.; Cho, K.; Bao, Z.; Lee, D. R.; Kang, M. S.; Kim, D. H. Combinatorial Study of Temperature-Dependent Nanostructure and Electrical Conduction of Polymer Semiconductors: Even Bimodal Orientation Can Enhance 3D Charge Transport. *Adv. Funct. Mater.* **2016**, *26*, 4627–4634. https://doi.org/10.1002/adfm.201601164.

[143] Himmelberger, S.; Vandewal, K.; Fei, Z.; Heeney, M.; Salleo, A. Role of Molecular Weight Distribution on Charge Transport in Semiconducting Polymers. *Macromolecules* **2014**, *47*, 7151–7157.

https://doi.org/10.1021/ma501508j.

[144] Gu, K.; Loo, Y.-L. The Polymer Physics of Multiscale Charge Transport in Conjugated Systems. *J. Polym. Sci. Part B: Polym. Phys.* **2019**, *57*, 1559–1571. https://doi.org/10.1002/polb.24873.

[145] Liu, Q.; Wang, Y.; Kohara, A.; Matsumoto, H.; Manzhos, S.; Feron, K.; Bottle, S. E.; Bell, J.; Michinobu, T.; Sonar, P. Tuning the Charge Carrier Polarity of Organic Transistors by Varying the Electron Affinity of The Flanked Units in Diketopyrrolopyrrole-Based Copolymers. *Adv. Funct. Mater.* **2020**, *30*, 1907452. https://doi.org/10.1002/adfm.201907452.

[146] Sawicka, M.; Storoniak, P.; Skurski, P.; Blazejowski, J.; Rak, J. TG-FTIR, DSC and Quantum Chemical Studies of the Thermal Decomposition of Quaternary Methylammonium Halides. *Chem. Phys.* **2006**, *324*, 425–437. https://doi.org/10.1016/j.chemphys.2005.11.023.

[147] Huo, J.; Deng, Q.; Fan, T.; He, G.; Hu, X.; Hong, X.; Chen, H.; Luo, S.; Wang, Z.; Chen, D. Advances in Polydiacetylene Development for the Design of Side Chain Groups in Smart Material Applications – A Mini Review. *Polym. Chem.* **2017**, *8*, 7438–7445. https://doi.org/10.1039/c7py01396e.

[148] Tahir, M. N.; Nyayachavadi, A.; Morin, J.-F.; Rondeau-Gagne, S. Recent Progress in the Stabilization of Supramolecular Assemblies with Functional Polydiacetylenes. *Polym. Chem.* **2018**, *9*, 3019–3028. https://doi.org/10.1039/c8py00536b.

[149] Fang, F.; Meng, F.; Luo, L. Recent Advances on Polydiacetylene-Based Smart Materials for Biomedical Applications. *Mater. Chem. Front.* **2020**, *4*, 1089–1104. https://doi.org/10.1039/c9qm00788a.

[150] Deschamps, J.; Balog, M.; Boury, B.; Yahia, M. B.; Filhol, J.-S.; van der Lee, A.; Choueiry, A. A.; Barisien, T.; Legrand, L.; Schott, M.; Dutremez, S. G. Tuning Topochemical Polymerization of Diacetylenes: A Joint Synthetic, Structural, Photophysical, and Theoretical Study of a Series of Analogues of a Known Reactive Monomer, 1,6-Bis(diphenylamino)-2,4-hexadiyne (THD). *Chem. Mater.* **2010**, *22*, 3961–3982. https://doi.org/10.1021/cm1008703.

[151] Jordan, R. S.; Wang, Y.; McCurdy, R. D.; Yeung, M. T.; Marsh, K. L.; Khan, S. I.; Kaner, R. B.; Rubin, Y. Synthesis of Graphene Nanoribbons via the Topochemical Polymerization and Subsequent Aromatization of a Diacetylene Precursor. *Chem* **2016**, *1*, 78–90. https://doi.org/10.1016/j.chempr.2016.06.010.

[152] Neabo, J. R.; Rondeau-Gagne, S.; Vigier-Carriere, C.; Morin, J. F. Soluble Conjugated One-Dimensional Nanowires Prepared by Topochemical Polymerization of a Butadiynes-Containing Star-Shaped Molecule in the Xerogel State. *Langmuir* **2013**, *29*, 3446–3452.

https://doi.org/10.1021/la305045n.

[153] Maeda, K.; Hong, L.; Nishihara, T.; Nakanishi, Y.; Miyauchi, Y.; Kitaura, R.; Ousaka, N.; Yashima, E.; Ito, H.; Itami, K. Construction of Covalent Organic Nanotubes by Light-Induced Cross-Linking of Diacetylene-Based Helical Polymers. *J. Am. Chem. Soc.* **2016**, *138*, 11001–11008. https://doi.org/10.1021/jacs.6b05582.

[154] Nyayachavadi, A.; Mason, G. T.; Tahir, M. N.; Ocheje, M. U.; Rondeau-Gagné, S. Covalent Cross-Linking of Diketopyrrolopyrrole-Based Organogels with Polydiacetylenes. *Langmuir* **2018**, *34*, 12126–12136. https://doi.org/10.1021/acs.langmuir.8b02807.

[155] Butera, R. J.; Simic-Glavaski, B.; Lando, J. B. Cross-Polymerization of Poly(α,ω-alkyldiyne) Macromonomers. *Macromolecules* **1990**, *23*, 199–210. https://doi.org/10.1021/ma00203a035.

[156] Hernandez-Rojas, M. E.; Peralta, E.; Beristain, M. F.; Ogawa, T. Non-Topochemical Cross-Linking of Amorphous Aliphatic Diacetylene-Containing Polymers. *Des. Monomers Polym.* **2010**, *13*, 473–486. https://doi.org/10.1163/138577210X521369.

[157] Badarau, C.; Wang, Z. Y. Synthesis and Optical Properties of Thermally and Photochemically Cross-Linkable Diacetylene-Containing Polymers. *Macromolecules* **2004**, *37*, 147–153. https://doi.org/10.1021/ma035566x.

[158] Kanbara. T.; Ohshima, S.; Hasegawa, K.; Takeuchi, S. Preparation and Characterization of Poly(9-hexylcarbazole-3,6-diylbutadiynylene). *Polym. Bull.* **1997**, *39*, 453–458. https://doi.org/10.1007/s002890050172.

[159] Rutherford, D. R.; Stille, J. K. Poly(ethynylene-2,5-thiophenediylethynylenes). Processable, Reactive Polymers That Thermally Cross-Link. *Macromolecules* **1988**, *21*, 3530–3532. https://doi.org/10.1021/ma00190a035.

[160] Rutherford, D. R.; Stille, J. K.; Elliott, C. M.; Reichert, V. R. Poly(2,5-ethynylenethiophenediylethynylenes), Related Heteroaromatic Analogues, and Poly(thieno[3,2-*b*]thiophenes): Synthesis and Thermal and Electrical Properties. *Macromolecules* **1992**, *25*, 2294–2306. https://doi.org/10.1021/ma00035a003.

[161] Jolly, A.; Miao, D.; Daigle, M.; Morin, J.-F. Emerging Bottom-Up Strategies for the Synthesis of Graphene Nanoribbons and Related Structures. *Angew. Chem. Int. Ed.* **2020**, *59*, 4624–4633. https://doi.org/10.1002/anie.201906379.

[162] Haussler, M.; Zheng, R.; Lam, J. W. Y.; Tong, H.; Dong, H.; Tang, B. Z. Hyperbranched Polyynes: Syntheses, Photoluminescence, Light Refraction, Thermal Curing, Metal Complexation, Pyrolytic Ceramization, and Soft Magnetization. *J. Phys. Chem. B* **2004**, *108*, 10645–10650. https://doi.org/10.1021/jp047857t.

[163] Sun, H.; Oner, I. H.; Wang, T.; Zhang, T.; Selyshchev, O.; Neumann, C.; Fu, Y.; Liao, Z.; Xu, S.; Hou, Y.; Turchanin, A.; Zahn, D. R. T.; Zschech, E.; Weidinger, I. M.; Zhang, J.; Feng, X. Molecular Engineering of Conjugated Acetylenic Polymers for Efficient Cocatalyst-Free Photoelectrochemical Water Reduction. *Angew. Chem. Int. Ed.* **2019**, *58*, 10368–10374. https://doi.org/10.1002/anie.201904978.

[164] Wang, L.; Wan, Y.; Ding, Y.; Wu, S.; Zhang, Y.; Zhang, X.; Zhang, G.; Xiong, Y.; Wu, X.; Yang, J.; Xu, H. Conjugated Microporous Polymer Nanosheets for Overall Water Splitting Using Visible Light. *Adv. Mater.* **2017**, *29*, 1702428. https://doi.org/10.1002/adma.201702428.

[165] Jayanthi, S.; Muthu, D. V. S.; Jayaraman, N.; Sampath, S.; Sood, A. K. Semiconducting Conjugated Microporous Polymer: An Electrode Material for Photoelectrochemical Water Splitting and Oxygen Reduction. *ChemistrySelect* **2017**, *2*, 4522–4532. https://doi.org/10.1002/slct.201700505.

[166] Otep, S.; Michinobu, T.; Zhang, Q. Pure Organic Semiconductor-Based Photoelectrodes for Water Splitting. *Sol. RRL* **2020**, *4*, 1900395. https://doi.org/10.1002/solr.201900395.

[167] Eckstein, B. J.; Melkonyan, F. S.; Zhou, N.; Manley, E. F.; Smith, J.; Timalsina, A.; Chang, R. P. H.; Chen, L. X.; Facchetti, A.; Marks, T. J. Buta-1,3-diyne-Based □-Conjugated Polymers for Organic Transistors and Solar Cells. *Macromolecules* **2017**, *50*, 1430–1441. https://doi.org/10.1021/acs.macromol.6b02702.

[168] Seidler, A.; Svoboda, J.; Dekoj, V.; Chocholousova, J. V.; Vacek, J.; Stara, I. G.; Stary, I. The Synthesis of π-Electron Molecular Rods with a Thiophene or Thieno[3,2-*b*]thiophene Core Unit and Sulfur Alligator Clips. *Tetrahedron Lett.* **2013**, *54*, 2795–2798. https://doi.org/10.1016/j.tetlet.2013.03.084.

[169] Li, W.; Guo, Y.; Shi, J.; Yu, H.; Meng, H. Solution-Processable Neutral Green Electrochromic Polymer Containing Thieno[3,2-*b*]thiophene Derivative as Unconventional Donor Units. *Macromolecules* **2016**, *49*, 7211–7219. https://doi.org/10.1021/acs.macromol.6b01624.

[170] Deng, P.; Wu, B.; Lei, Y.; Cao, H.; Ong, B. S. Regioregular and Random Difluorobenzothiadiazole Electron Donor-Acceptor Polymer Semiconductors for Thin-Film Transistors and Polymer Solar Cells. *Macromolecules* **2016**, *49*, 2541–2548. https://doi.org/10.1021/acs.macromol.5b02754.

[171] Frisch, M. J.; Trucks, G. W.; Schlegel, H. B.; Scuseria, G. E.; Robb, M. A.; Cheeseman, J. R.; Scalmani, G.; Barone, V.; Petersson, G. A.; Nakatsuji, H.; et al. *Gaussian 16, Revision C.01;* Gaussian, Inc.: Wallingford CT, 2016.

[172] Dennington, R.; Keith, T. A.; Millam, J. M. *GaussView, Version 6.1.1;*

Semichem Inc.: Shawnee Mission, KS, 2016.

[173] Krishnan, D.; Amal, R. R. B.; Gowd, E. B. Topochemical Polymerization of Hierarchically Ordered Diacetylene Monomers within the Block Copolymer Domains. *Polym. Chem.* **2019**, *10*, 3154–3162. https://doi.org/10.1039/c9py00156e.

[174] Zhou, G. J.; Zhang, S.; Ye, C. The Effect of Self-Assembly on the Optical Nonlinear Absorption of Poly(3-hexyl-2,5-thienylenediethynylene). *J. Phys. Chem. B* **2004**, *108*, 3985–3988. https://doi.org/10.1021/jp034940s.

[175] Kamimoto, N.; Nakamura, N.; Tsutsumi, A.; Mandai, H.; Mitsudo, K.; Wakamiya, A.; Murata, Y.; Hasegawa, J.-y.; Suga, S. Facile Synthesis of 1,4-Bis(diaryl)-1,3-butadiynes Bearing Two Amino Moieties by Electrochemical Reaction-Site Switching, and Their Solvatochromic Fluorescence. *Asian J. Org. Chem.* **2016**, *5*, 373–379. https://doi.org/10.1002/ajoc.201500502.

[176] Marek, P. H.; Szatylowicz, H.; Krygowski, T. M. Stacking of Nucleic Acid Bases: Optimization of the Computational Approach—the Case of Adenine Dimers. *Struct. Chem.* **2019**, *30*, 351–359. https://doi.org/10.1007/s11224-018-1253-7.

[177] Sabuzi, F.; Stefanelli, M.; Monti, D.; Conte, V.; Galloni, P. Amphiphilic Porphyrin Aggregates: A DFT Investigation. *Molecules* **2020**, *25*, 133. https://doi.org/10.3390/molecules25010133.

[178] Ali, I.; Sharma, S.; Bezbaruah, B. Quantum Mechanical Study on the π-π Stacking Interaction and Change in Conformation of Phenolic Systems with Different Intermolecular Rotations. *Computational Chemistry* **2018**, *6*, 71–86. https://doi.org/10.4236/cc.2018.64006.

[179] Kerru, N.; Gummidi, L.; Bhaskaruni, S. V. H. S.; Maddila, S. N.; Singh, P.; Jonnalagadda, S. B. A Comparison Between Observed and DFT Calculations on Structure of 5-(4-Chlorophenyl)-2-amino-1,3,4-thiadiazole. *Sci. Rep.* **2019**, *9*, 19280. https://doi.org/10.1038/s41598-019-55793-5.

[180] Yanai, T.; Tew, D. P.; Handy, N. C. A New Hybrid Exchange–Correlation Functional Using the Coulomb-Attenuating Method (CAM-B3LYP). *Chem. Phys. Lett.* **2004**, *393*, 51–57. https://doi.org/10.1016/j.cplett.2004.06.011.

[181] Chai, J.-D.; Head-Gordon, M. Long-Range Corrected Hybrid Density Functionals with Damped Atom–Atom Dispersion Corrections. *Phys. Chem. Chem. Phys.* **2008**, *10*, 6615–6620. https://doi.org/10.1039/b810189b.

[182] Wu, Z.; Petzold, A.; Henze, T.; Thurn-Albrecht, T.; Lohwasser, R. H.; Sommer, M.; Thelakkat, M. Temperature and Molecular Weight Dependent Hierarchical Equilibrium Structures in Semiconducting Poly(3-hexylthiophene). *Macromolecules* **2010**, *43*, 4646–4653. https://doi.org/10.1021/ma902566h.

[183] Metivaud, V.; Lefevre, A.; Ventola, L.; Negrier, P.; Moreno, E.; Calvet, T.; Mondieig, D.; Cuevas-Diarte, M. A. Hexadecane ($C_{16}H_{34}$) + 1-Hexadecanol ($C_{16}H_{33}OH$) Binary System: Crystal Structures of the Components and Experimental Phase Diagram. Application to Thermal Protection of Liquids. *Chem. Mater.* **2005**, *17*, 3302–3310. https://doi.org/10.1021/cm050130c.

[184] Nishide, J.; Oyamada, T.; Akiyama, S.; Sasabe, H.; Adachi, C. High Field-Effect Mobility in an Organic Thin-Film Transistor with a Solid-State Polymerized Polydiacetylene Film as an Active Layer. *Adv. Mater.* **2006**, *18*, 3120–3124. https://doi.org/10.1002/adma.200601419.